



Treball Final de Grau

Validation of the scale-up process of highly-concentrated emulsions

Validació del procés d'escalat d'emulsions altament concentrades

Jordi Ribó i Besolí

June 2013



Dos campus d'excel·lència internacional

B:KC

Barcelona
Knowledge
Campus

HUB

Health Universitat
de Barcelona
Campus

Aquesta obra està subjecta a la llicència de:
Reconeixement–NoComercial–SenseObraDerivada



<http://creativecommons.org/licenses/by-nc-nd/3.0/es/>

Tota convicció —convicció seriosa— se us convertirà en prejudici per a les conviccions ulteriors. Penseu-hi. Cada convicció que adquiriu és un prejudici més que acumuleu. I ja sabeu què vol dir un prejudici: un vici d'origen. Si sou zelosos de la vostra llibertat intel·lectual, si aspireu a conservar la «disponibilitat permanent» que n'és el pressupòsit, heu d'esforçar-vos per ser homes d'escasses conviccions. El fanàtic és un convençut: un individu que està convençut de tot, que té moltes conviccions. No crec que el fanatisme sigui una perspectiva gaire amable. La prudència, virtut cardinal, aconsella evitar aquestes exasperacions mentals i morals. I al capdavant, per a circular per la vida, no calen massa conviccions. N'hi basten tres o quatre. Només.

Joan Fuster. Diccionari per a ociosos

Acknowledgements

I would like to express my gratitude to my supervisors, Anna May Masnou and Dr. José María Gutiérrez, for their invaluable guidance and advice throughout my project.

My thanks also go to all my lab mates for their support and help to achieve this work and particularly to Bryshila, Diey, Esther, Mabel, Isabel and Toni.

Publications

Some of the work in this Final Bachelor's Project has been included in the following paper:

May-Masnou, A., Ribó-Besolí, J., Porras, M., Maestro, A., González, C. & Gutiérrez, J. M. (2014). Scale-up model obtained from the rheological analysis of highly concentrated emulsions prepared at three scales. *Chemical Engineering Science*, 111, 410–420.
doi:10.1016/j.ces.2014.03.004

REPORT

Summary

Emulsions are dispersions of two immiscible liquids, one of which is dispersed as tiny droplets -dispersed phase- in the other one -continuous phase. The decisive parameter to characterise an emulsion is the dispersed phase volume fraction ϕ . This study is focused on high-internal-phase-ratio emulsions (HIPRE), which are defined by ϕ exceeding 0.74, defined as the ratio in which the spheres of the dispersed phase are monodispersed undistorted forming the most compact packing. In this work, water-in-oil (W/O) emulsions are constituted by a 90 % wt/wt (88 % vol/vol) of water dispersed in the continuous phase (dodecane and surfactant Span 80).

The first goal of this work is the validation of empirical models obtained previously from central composite designs which apparently predict the emulsion properties given some fixed preparation and composition conditions. Actually, three of these conditions are studied: the stirring rate of the impeller and the addition flow rate, as preparation factors; and the surfactant concentration (surfactant-to-dodecane ratio), as composition variable. The characterisation of the emulsions is carried out testing their viscoelastic behaviour -rheological tests-, the stability over time -by measuring changes on the back scattering- and droplet size -determined through images obtained with an optical microscope. To do the validation of the models, additional experiments are carried out following a simple design in the experimental range of the variables.

The preparation of the emulsions is simple and in this step is where the different factors are varied in order to analyse their effects on the emulsion. The continuous phase -organic one, in which surfactant concentration is varied from one experiment to another- is introduced into the jacketed-tank at 25 °C and then, the impeller is set at a fixed stirring rate and the dispersed phase -water- is added at a constant flow rate. In this method, emulsions are formed thanks to the energy input provided by the stirrer.

Moreover, the availability of three tanks with geometric similarity (1:2:4) allows us to evaluate the scale-up process. Therefore, a second goal of this study is to obtain an empirical scale-up model, whose main objective is the prediction of the necessary preparation and composition conditions

at each scale to prepare the same emulsion at the three scales. The parameter $N \cdot D^\alpha$, as a function of the stirring rate N , the scale (D , impeller diameter) and the exponent α -calculated empirically from the regression of all the experiments in the three scales-, is defined as a factor in the scale-up study.

Finally, focusing on the first goal, only the models of some rheological parameters at small and medium scale are validated, the unfitting of the others would be caused by an erroneous calibration of the rheometer (the two series of experiments have been measured in two different rheometers with a time difference of three years), in the case of the other rheological parameters; and by the subjectivity of the measurement (measured manually, where the random choice of droplets, the background, etc might be determinant factors), regarding the droplet size. However, the general behaviour is similar, although the experimental and the predicted values differ.

Regarding to the second goal, two global models (one from experiments of the current study, and another putting together the previous and the current ones), as a function of the surfactant concentration, addition time and the scale invariant previously mentioned $N \cdot D^\alpha$, are obtained and they possess a really similar exponent α ($\alpha = 0.63$ and $\alpha = 0.65$, respectively), which indicates the similarity of behaviour of both experimental series. Obviously, in the current conditions, the experimental values fit better with the first model, yet on the second one, the experimental values are included into the confidence intervals and they follow a random distribution (the experimental values at each scale are higher or lower than the model predicts). The exponent α indicates that the equivalent scale-up invariant is the power per unit volume P/V , broadly used and recommended in mixing scale-up processes.

As far as we know, no other study has obtained a scale invariant factor $N \cdot D^\alpha$ for the preparation of highly-concentrated emulsions prepared at three different scales, that covers all three scales, different addition times, stirring rates and surfactant concentrations, so this is an exceptional result and a remarkable conclusion.

Resum

Les emulsions són dispersions estables de dos component immiscibles en què una fase –la dispersa- és dispersada en l'altra -fase continua-. La quantitat relativa de cada fase present és la que defineix si una emulsió és altament concentrada o no, de fet, la fracció en volum de la fase dispersa ha de ser més gran que 74 % (fracció en què la disposició espacial de les gotes és la més compacta possible). En aquest treball, s'estudien emulsions W/O -water in oil, en anglès; aigua en oli, en català-, en les quals la fase aquosa és la fase dispersa mentre que la fase orgànica, és la continua. L'aigua, en forma de gotes, constitueix un 90 % en pes de l'emulsió (88 % en volum de fase dispersa) mentre que la resta és la fase orgànica (dodecà i tensioactiu Span80).

Un primer objectiu del treball és la validació d'uns models empírics obtinguts prèviament a partir de dissenys centrals compostos que, aparentment (per això s'han de validar, fent experiments addicionals dins del rang experimental), prediuen com serà l'emulsió un cop fixades unes determinades condicions de preparació i composició. Aquest factors són la velocitat d'agitació i el cabal d'addició de la fase continua, quant a variables de preparació; i la concentració de tensioactiu en la fase orgànica, com a variable de composició. La caracterització de l'emulsió es duu a terme avaluant-ne el comportament viscoelàstic -tests reològics-, estabilitat al llarg del temps –mitjançant tests de dispersió de llum- i mida de les gotes –determinada a partir de fotos realitzades amb un microscopi òptic.

La preparació de l'emulsió és relativament senzilla i aquí és on intervenen els diferents factors variats per a estudiar com és l'emulsió La fase continua -orgànica, on la concentració de tensioactiu varia entre experiments- es col·loca dins d'un tanc a 25 °C i, a continuació, l'agitador es fixa a una determinada velocitat de gir i s'addiciona de la fase dispersa –aigua- durant un temps fixat. En aquest mètode, l'emulsió es forma per l'energia subministrada en forma d'agitació. A més, la disponibilitat de tres tancs geomètricament similars (1:2:4) permet avaluar-ne el procés d'escalat. Així doncs, un segon objectiu del treball és l'obtenció d'un model empíric del canvi d'escala que serveixi per a predir les condicions de preparació i de composició necessàries per tal d'obtenir la mateixa emulsió a les tres escales. A fi d'aconseguir-ho, es defineix un nou factor,

el paràmetre $N \cdot D^\alpha$, que depèn de la velocitat d'agitació N , l'escala utilitzada (D , diàmetre de l'agitador) i l'exponent α , que s'obté empíricament a partir de l'ajust de tots els valors a les diferents escales.

Finalment, respecte al primer objectiu, només els models d'alguns paràmetres reològics en l'escala petita i mitjana es validen, el no encaix de la resta pot ser atribuïble a un calibrat diferent del reòmetre (se n'han fet servir dos de diferents i amb una diferència de temps de tres anys) en el cas de les propietats reològiques; i a la subjectivitat de la mesura (mesurada manualment on la tria aleatòria de gotes, l'experiència, etc poden ser factors determinants) pel que fa a la mida de gota. Tot i això, la tendència que segueixen és similar, el que dista són els valors experimentals i els predits pel model.

Quant al segon objectiu, s'han obtingut dos models globals (un amb tots els experiments d'aquest estudi, i un altre, amb els d'aquest i els previs), funció de la concentració de tensioactiu, el temps d'addició i l'invariant anteriorment mencionat $N \cdot D^\alpha$, que pel que fa a l'exponent α són molt similars ($\alpha = 0.63$ i $\alpha = 0.65$, respectivament), fet que indica que la tendència de les dues sèries de punts és similar. Com és obvi, en les condicions actuals, els punts s'ajusten millor al primer model; però en el segon, el valors experimentals estan dins dels intervals de confiança, a més de seguir una distribució aleatòria (els valors a cada escala presenten valors superiors i inferiors als predits pel model). L'exponent α indica que l'invariant de canvi d'escala equivalent és la potència per unitat de volum P/V , àmpliament utilitzat i recomanat en processos d'escalat de mescles.

Segons tenim constància, cap altre estudi ha obtingut un invariant d'escala $N \cdot D^\alpha$ en la preparació d'emulsions altament concentrades en tres escales que abasti les tres escales, diferents temps d'addició, velocitats d'agitació i concentracions de tensioactiu. Per tant, és un excel·lent resultat i una conclusió molt destacable.

Contents

1. INTRODUCTION	1
1.1. High-internal phase ratio emulsions (HIPRE)	1
1.1.1. Concept	1
1.1.2. Preparation of HIPRE	1
1.1.3. Characterisation	3
1.1.3.1. Rheology	3
1.1.3.2. Stability analysis	8
1.1.3.3. Droplet size and polydispersity	11
1.2. Scale-up	12
1.3. Experimental design	15
2. OBJECTIVES	17
3. MATERIALS AND METHODS	19
3.1. Materials	19
3.2. Methods	19
3.2.1. Preparation of HIPREs	19
3.2.2. Characterisation of HIPRE	21
3.2.2.1. Rheological parameters	21
3.2.2.2. Stability analysis	22
3.2.2.3. Droplet size and polydispersity	23
3.2.3. Experimental design	24
4. RESULTS AND DISCUSSION	25
4.1. Validation of the models at each scale	25
4.1.1. Validation of the models at small scale	25
4.1.1.1. Models at small scale	25
4.1.1.2. Influence of stirring rate at small scale	26
4.1.1.3. Influence of addition time at small scale	28
4.1.1.4. Influence of S/O rate at small scale	31
4.1.2. Validation of the models at medium scale	37
4.1.2.1. Models at medium scale	37
4.1.2.2. Influence of stirring rate at medium scale	38
4.1.2.3. Influence of addition time at medium scale	41

4.1.2.4. Influence of S/O rate at medium scale	43
4.2. Validation of the scale-up models	47
4.2.1. Experiments at large scale	47
4.2.2. Validation of the scale-up models	48
4.3. Preparation of meso- and macroporous materials	59
5. CONCLUSIONS	61
6. REFERENCES	65
7. ABBREVIATIONS AND NOMENCLATURE	69
APPENDICES	71
A 1. Validation of the models at each scale	73
A 1.1. Models at small scale	73
A 1.2. Models at medium scale	74
A 1.3. Experiments performed	76
A 1.4. Graphical representation of the models and the experiments to validate them	78
A 2. Validation of the scale-up models	94
A 2.1. Scale-up models at fixed conditions	94
A 2.2. Scale-up models from general models at medium and small scale	99
A 2.3. Scale-up models from all the current experiments	100
A 2.4. Scale-up general models from all the current and previous experiments.	104
A 2.5. Images of the droplets of the emulsions obtained with the optical microscope	108

1. Introduction

1.1. High-internal phase ratio emulsions (HIPRE)

1.1.1. Concept

Emulsions are dispersions of two immiscible liquids, one of which is dispersed as tiny droplets -dispersed phase- in the other one -continuous phase. In this study of water in oil (W/O) emulsions, oil is the continuous phase, so the dispersed one is water. Emulsions also contain a third component, called the emulsifying agent, emulsifier or surfactant, which has two principal functions¹:

- To decrease the interfacial tension between oil and water
- To stabilise the droplets against coalescence once they are formed.

The decisive parameter to characterise an emulsion is the dispersed phase volume fraction ϕ . This study is focused on high-internal-phase-ratio emulsions (HIPRE) which are defined by ϕ exceeding 0.74, defined as the ratio in which the spheres of the dispersed phase are monodispersed undistorted forming the most compact packing. When ϕ is greater than 0.74, the emulsions structure consists of polyhedral droplets separated by thin films of continuous phase, a structure resembling gas-liquid foams and when ϕ is lower, droplets maintain their spherical shape.

Highly concentrated emulsions are broadly used in different applications such as food (sauces, spreads, dressings), cosmetics, protective films, topical drug delivery, aviation fuel, extraction of antibiotics and pollutants, preparation of meso- and macroporous materials, etc.²

1.1.2. Preparation of HIPRE

The droplet size is the determining factor when choosing the proper method to prepare HIPRE. In the high-energy methods, high mechanical energy is applied during emulsification, in which the deforming forces are able to break the droplets into smaller ones³. Therefore, the smaller the droplet size is, the more energy is required. Some examples of equipments used are *colloid mill*, in which the stirring rate is around 3,000 rpm⁴ and *Ultra-Turrax*, in which the mechanical energy

input depends on the experiment -France et al.⁵ fixed the stirring rate at 8,000 rpm, or Aranberri et al.⁶ at 11,000 rpm. When the agitation rate is not so high, these mechanical methods are known as medium-energy methods. Capdevila et al.⁷, in their evaluation of the influence of composition and preparation variables on the W/O emulsion properties, applied a medium mechanical energy method; actually, the higher stirring rate was 800 rpm. This is also the method followed in this study: a suitable amount of emulsifier is dissolved in the oil that will constitute the continuous phase, followed by continuous addition of the water, which will constitute the dispersed phase, with continuous stirring over a determined period of time.⁸

On the contrary, the lower energy methods, or condensation methods, are based on the phase transitions taking place during the emulsification process. These methods allow achieving finer droplets reducing the time required for preparation and the energy input. These phase transitions result from changes in the spontaneous curvature of the surfactant and can be achieved (i) at constant composition by changing the spontaneous curvature of non-ionic surfactants with temperature, the Phase Inversion Temperature, PIT or (ii) at constant temperature by varying the composition of the system by the Emulsion Inversion Point (EIP) method⁹.

The PIT method is based on the physicochemical property defined by the hydrophile-lipophile balance (HLB) temperature (T_{HLB}) that is the temperature at which the hydrophilic and lipophilic properties of the surfactant are balanced in the system. For non-ionic surfactants, W/O highly concentrated emulsions can be formed by rapidly heating an O/W microemulsion, from a temperature lower than the T_{HLB} to a temperature up to 25-30 °C above it, forcing the transitional phase inversion.⁸ It is valid to prepare both W/O and O/W emulsions, raising or decreasing its temperature, respectively. Several authors carried out their research projects using this method, Esquena et al.¹⁰ prepared W/O emulsions solid polystyrene as templates for foams with a narrow pore size distribution. Fernandez et al.³ studied this method in O/W emulsions (water / paraffin oil / a mixture of non ionic surfactants and fatty acids). Figure 1 schematises the process.

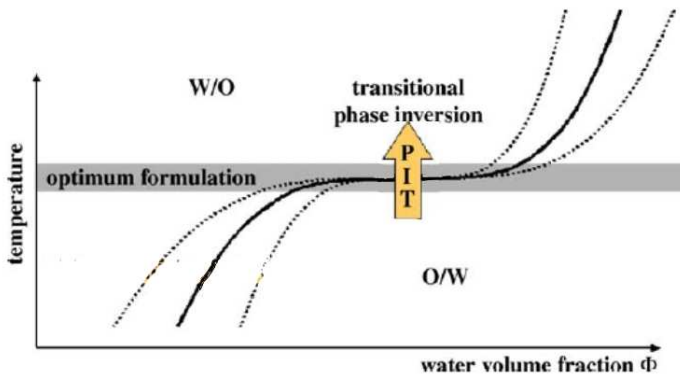


Figure 1 .Adapted from Fernandez et al.³. Schematic illustration of transitional (PIT) phase inversion for the preparation of finely dispersed W/O emulsions. The solid black line marks the inversion locus, the dotted lines the hysteresis zone. Within the optimum formulation zone and at the inversion locus, the interfacial tension is minimal. During low-energy emulsification, this ultralow interfacial tension is employed for the formation of finely dispersed droplets, while the final emulsion should be far away from these regions to enhance emulsion stability.

1.1.3. Characterisation

Once the HIPRE is prepared, an analysis of the influence of the composition –surfactant concentration- and preparation variables –stirring rate and addition time- on the rheological behaviour –i.e. yield stress, storage modulus, loss modulus and viscosity– and of the structural parameters such as droplet size, polydispersity, surface area of dispersion and stability, is developed.

1.1.3.1. Rheology

Steady shear test

The steady shear test -the shear stress versus shear rate plot- allows us to see directly if there is a Newtonian behaviour because the plot will take the form of a straight line through the origin. Alternatively, a non-Newtonian response is, by definition, nonlinear and may or may not pass through the origin. If the sample has an apparent yield stress, then the line or curve will have some positive y-axis intercept¹¹.

In Figure 2 (A), the Newtonian fluid yields a straight line that emanates from the origin. The other four examples are non-Newtonian fluids. τ_0 represents a yield stress point, which is common for plastic fluids.

Emulsions, particularly, are non-Newtonian fluids owing to the interactions between phases and the complexity of their structure. When HIPREs are subjected to a shear stress below a certain critical value, yield stress τ_0 , they exhibit very small deformation rates indicating creeping behaviour. Upon increasing the shear stress above τ_0 , a sharp increase in shear rate is observed indicating fracturing of the material.

The yield stress τ_0 is obtained by the intersection of two linear regressions on the log-log plot shear rate versus shear stress, as it is shown in Figure 2 (B). The first one, taking into account a few points before the sudden increase of the shear rate, and the other one, when the function grows sharply.

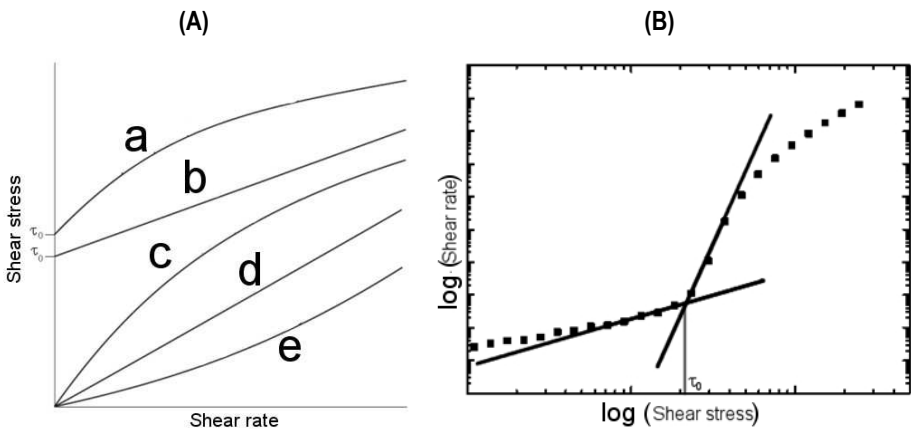


Figure 2. (A) Rheogram for five time-independent fluids. Adapted from Whittingstall¹¹ where: a, pseudoplastic plastic (shear thinning); b, Bingham plastic; c, pseudoplastic (shear thinning); d, Newtonian; e, dilatants (shear thickening). (B) Procedure to obtain the yield stress in steady shear test

Several authors have implemented this test in products characterisation such as Bhattacharya et al.^{12,13} in the characterisation of Tamarid Kernel Powder (TKP) suspensions and Rice-Blackgrams suspensions, respectively.

Oscillatory shear test

The graphical representation of storage modulus G' versus shear stress τ shows at low stresses, a zone of constant response (*plateau region*) indicating an unaltered structure, not disturbed by shear. In this linear region, the applied strains are very low; the droplets are crowded and cannot move freely past one another: this defines the elastic domain. With further increase in shear stress, the storage modulus drops sharply while the phase lag angle δ rises, the applied strain being sufficient to allow the fluid to move past one another and inducing a transition to the viscous domain: the emulsions then become more viscous than elastic. This change from the elastic to the viscous domain can be defined precisely by noting the stress (or the strain) when G'' reaches a maximum, this critical stress $(\tau_0)_c$ being considered as a yield stress. The G'' peak confirms and elucidates the transition from the elastic to viscous region¹⁴. See Figure 3.

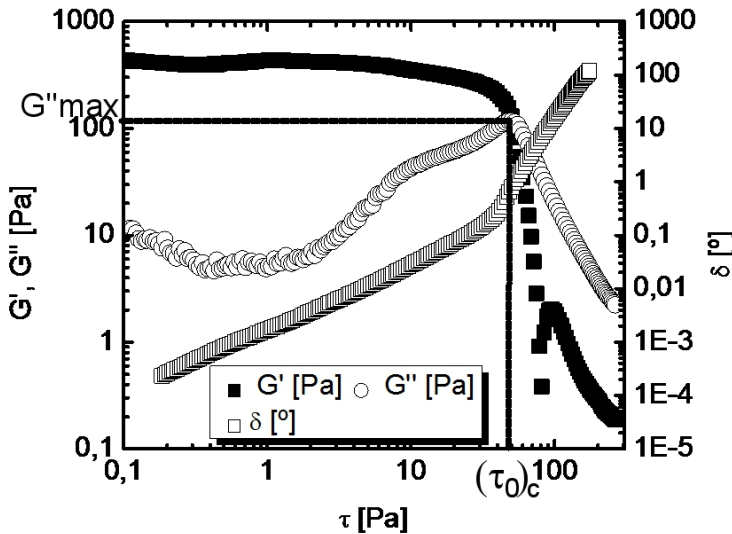


Figure 3. Procedure to obtain the critical yield stress in oscillatory shear test

Jager-Lézer et al¹⁴ analysed a series of highly concentrated lipophilic cosmetic emulsions for different volume fractions evaluating storage modulus G' , loss modulus G'' and phase angle δ versus shear stress.

Frequency sweep test

A frequency sweep test is a particularly useful test as it enables to study the viscoelastic properties of emulsions which possess microscopic mechanisms for both elastic energy storage and viscous dissipation. They are viscoelastic fluids, exhibiting a stress response to a dynamically applied shear strain that is partially liquid-like (viscous) and partially solid-like (elastic). The energy storage and dissipation per unit volume can be represented by the frequency-dependent complex viscoelastic shear modulus $G^*(\omega, \phi)$ perturbative shears in which the stress and strain are linearly proportional. The real part $G'(\omega) = \text{Re}[G^*(\omega)]$, or storage modulus, is the in-phase ratio of the stress with respect to an oscillatory strain, and reflects elastic mechanisms, whereas the imaginary part $G''(\omega) = \text{Im}[G^*(\omega)]$, or loss modulus, is the out-of-phase ratio of the stress with respect to the strain and reflects dissipative mechanisms.¹⁵ In conclusion, the storage modulus G' can be used as a measure of the elastic component of the sample and similarly, the loss modulus G'' – the viscous component of the sample.

At high frequencies, the values of each parameters are not accurate because the time to carry out the measurement -being the inverse of the frequency- its excessively low (at 100 Hz, the duration of each oscillation is 0.01 s) to get a reliable result. For this reason, we will only take into account the data measured up to 10 Hz. See Figure 4.

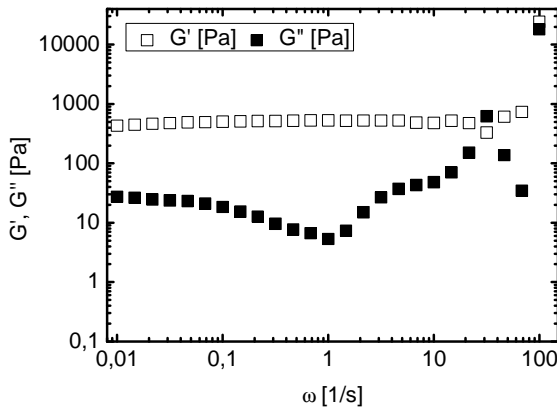


Figure 4. Frequency sweep test

Mason et al.¹⁵ evaluated the frequency ω dependence and volume fraction ϕ dependence of the complex shear modulus G^* in monodisperse emulsions¹⁵.

Viscosity versus shear rate test

Another valid parameter used to characterise emulsions is the graph of viscosity versus shear rate on a log-log plot. These curves have a typical shape represented by an initial plateau at low shear rate called the zero-shear viscosity η_0 , a final plateau at high shear rate called the infinite-shear viscosity η_∞ , and a linear portion linking them called the power law region. If all these characteristics are present, then the data can be considered to be a complete flow curve. Often, however, some of the high-shear or low-shear data will be absent. Typically, the controlled-rate rheometer will have problems probing the zero-shear viscosity, while the controlled-stress instrument may not reach the infinite shear viscosity.¹¹

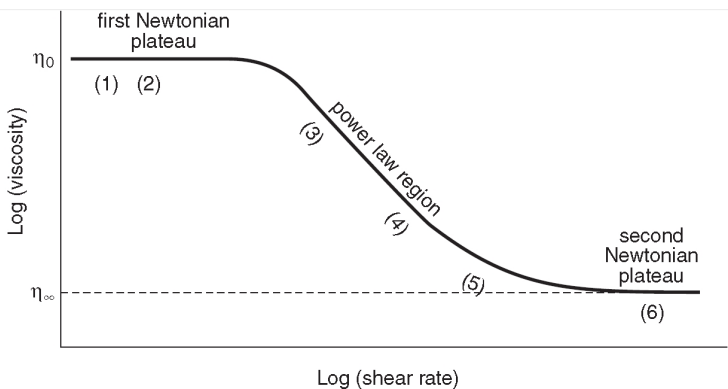


Figure 5. A complete flow curve for a time-independent non-Newtonian fluid.¹¹

In Figure 5, η_0 and η_∞ are the viscosities associated with the first and second Newtonian plateaus, respectively. Regions (1) and (2) correspond to viscosities relative to low shear rates induced by sedimentation and levelling, respectively. Regions (3) and (4) correspond to viscosities relative to the medium shear rates induced by pouring and pumping, respectively. Regions (5) and (6) correspond to viscosities relative to high shear rates by rubbing and spraying, respectively.¹¹

The relation between viscosity and shear rate was defined and depicted as a part of the characterisation of hydropropylmethyl-cellulose-stabilized emulsions (Kuclike et al.)¹⁶ The same test was developed with sodium carbomethylcellulose solution (Yang and Zhu)¹⁷ and by Manson and Bibette¹⁸ with O/W emulsions (silicone oil, water, non ionic surfactant NP7).

1.1.3.2. Stability analysis

Particle Science Inc in their *Technical Brief*⁹ expose the process by which an emulsion completely breaks. Coalescence -two or more droplets merge to form a single droplet- is generally considered to be governed by three different droplet loss mechanisms, i.e., flocculation, creaming / sedimentation and disproportionation / Ostwald ripening. The first two are the primary methods by which emulsions are destabilised but all three processes may occur simultaneously and in any order. Figure 6 presents a graphical representation of each phenomena.

Creaming - Sedimentation is not an actual breaking but a concentration change between the top and the bottom of the emulsions, one part of which (the cream) is richer in the disperse phase than the other. Creaming is the principal process by which the disperse phase separates from an emulsion and is typically the precursor to coalescence. Creaming is inhibited by a small droplet radius, a highly viscous continuous phase and a low density difference between the oil and water phases.

Flocculation can be generally defined as the aggregation of droplets to give 3-D clusters without coalescence occurring. Importantly, all droplets maintain their own integrity and remain as totally separate entities. It results when there is a weak, net attraction between droplets and arises through various mechanisms.

Flocculation may be subdivided for convenience into two general categories: that resulting from sedimentation aggregation and that from Brownian motion aggregation of the droplets. Both processes occur simultaneously in a typical emulsion and so cannot be rigorously separated. Because the magnitude of the forces involved is different for the two flocculation processes, the structure of the 3D droplet clusters is different.

Ostwald ripening is a process – often referred to as disproportionation – that is dependent on the diffusion of disperse phase molecules from smaller to larger droplets through the continuous phase. The pressure of dispersed material is greater for smaller droplets than larger. The pressure differential between small and large droplets constitutes the driving force for diffusion, but the rate of diffusion depends on the solubility of the dispersed phase in the continuous phase. The higher

the disperse phase volume, the greater its relative vapour pressure (and thus the solubility) will be. The diffusion rate is also impacted directly by the viscosity of the continuous phase.

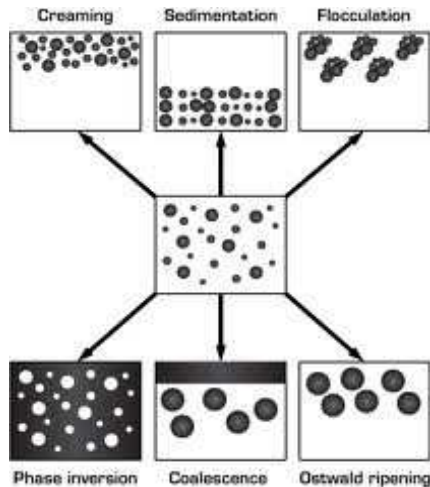


Figure 6. Schematic of mechanism of emulsion destabilisation

The stability of emulsions is determined by light scattering measurements (%BS profiles) to discern the way W/O emulsions would be destabilised over time. Bru et al.²⁰ propose a method to evaluate which destabilisation phenomena occur and to quantify its effect using the graphs of back scattering *BS* versus axial position provided by *Turbiscan MA 2000*.

- **Sedimentation – Creaming:** It is clearly observed a decrease of the backscattered light flux at the bottom of the sample due to lower particle volume fraction in this region (clarification) and, on the other hand, an increase of the back scattering level at the top of the sample due to particle density increase during creaming. See Figure 7.

The same kind of behaviour is observed for sedimentation processes with an increase of the back scattering level at the bottom and decrease at the top of the sample. It is then possible to analyze creaming kinetics through the time evolution of the cream thickness and then compare the stability between samples.

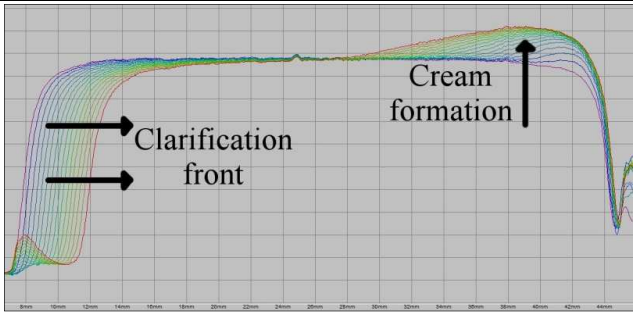


Figure 7. Creaming emulsion

- Particle size variation** Coalescence and flocculation phenomena are physico-chemically very different but lead to an increase of the scatterers size. Both phenomena can be differentiated in the way that coalescence results from the fusion of closed drops whereas particles stick during a flocculation or aggregation process. In some case flocculation of droplets can lead to coalescence. Particle size variation induced by these phenomena is detected as it leads to a decrease of the back scattering level over the whole sample height. Figure 8 indeed shows a decrease of the back scattering level everywhere in the cell during a coalescence process

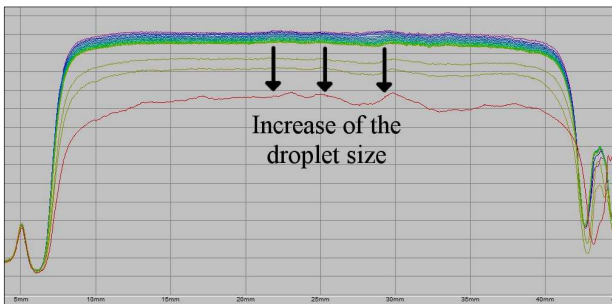


Figure 8. Coalescing emulsion

Emulsions do not generally undergo only one phenomenon but several at the same time. The *Turbiscan*® allowing an instability macroscopic visualization of the stability of concentrated dispersions, it is possible to discriminate various destabilizations. The profiles obtained are a combination of the ones previously described.

1.1.3.3. Droplet size and polydispersity

The droplet size is described as the surface-volume (Sauter) mean diameter d_{32} and the polydispersity is quantified by the standard deviation s and by the coefficient of variation cv –as a function of the mean diameter d_{10} and the standard deviation–, considering in both the maximum number of measured droplets.

$$d_{32} = \frac{\sum n_i d_i^3}{\sum n_i d_i^2}; cv = \frac{s}{d_{10}}$$

When $cv < 0.2$, the emulsion obtained is considered to be monodisperse.

Another parameter that characterises the emulsion is the surface area of dispersion a_v , which is defined as the interfacial area of dispersed phase a_d per unit volume of the whole dispersion $V_t = \frac{V_d}{\phi}$, where ϕ is the dispersed phase volume fraction and V_d the volume it occupies.

Taking $a_d = n \pi d_{32}^2$ and $V_d = \frac{n \pi d_{32}^3}{6}$, where n is the number of droplets, d_{32} the Sauter mean diameter. a_v is defined as surface divided by volume, so the units are m^2/m^3 of m^{-1} . Then,

$$a_v = \frac{a_d}{V_t} = \frac{6 \phi}{d_{32}}$$

It is obvious that a correlation between the rheological properties of an emulsion and its internal structure exists. Malkin et al.²¹ concluded that the smaller the droplets are, the higher viscosity and elastic component the emulsion possesses, Teipel²² evaluated the influence of the droplet size on the shear stress at a given shear rate and concluded that the smaller droplet emulsion exhibited a higher shear stress. Some theoretical models exposed by Paruta-Tuarez et al.²³ defined the storage modulus G' and the yield stress τ_0 as a function of internal structure parameters and composition of the emulsion. The most known model is the Princen & Kiss which relates the static shear modulus G to the dispersed-phase volume fraction ϕ , the Sauter mean radius R_{32} and the interfacial tension σ .

$$G = 1.769 \frac{\sigma}{R_{32}} \phi^{1/3} (\phi - 0.712)$$

1.2. Scale-up

Scale-up is a difficult task in many cases as a variety of poorly defined and interacting factors can influence the final product of an industrial process. In the simplest case, geometric, dynamic, kinematic, thermal, and/or chemical similarities are targets for scale-up.²⁴ There are several methods to achieve appropriate scale-up of mixing as described by Gorsky²⁵.

The first involves geometric similarity. This technique employs proportional scale-up of geometric parameters of the vessel. The scaled-up parameters may include such geometric ratios as D/T , where D is the diameter of the impeller and T is the diameter of the tank, and H/T , where H is the height of the liquid in the vessel. Similar ratios are compared for both small-scale vessel (D_1, T_1) and the larger-scale on (D_2, T_2). In most design, the value of the ratio D/T -will be between $0.15 < D/T < 0.6$ and the ratio H/T , $0.3 < H/T < 1.5$. In stirred tanks with viscous fluids (such as emulsions) the ratio D/T is close to the unity so as to avoid the formation of a layer of immobilised –not mixed– emulsion between the walls and the impeller due to their viscous properties. Therefore, the impeller sweeps the layer of emulsion that if the ratio was lesser, it would not be homogenised.

Assuming the geometric similarity, the second method^{25,26} for achieving appropriate scale-up of mixing uses dimensionless numbers to predict scale-up parameters. The use of dimensionless numbers proposed by Wilkens, R. J. & Gates²⁶ simplifies design calculations by reducing the number of variables to consider.

- **Impeller Reynolds number**, Re is usually the primary independent variable in a dimensionless-number correlation:

$$Re = \frac{D^2 \rho N}{\mu}$$

Where N is the rotational speed [s^{-1}], D is the impeller blade diameter [m], ρ is the density of solution dispersion [kg/m^3] and μ is the viscosity of solution dispersion [$kg/(m \cdot s)$].

- **Froude number**, Fr , is the ratio of inertial to gravitational force:

$$Fr = \frac{DN^2}{g}$$

Rotational speed tends to decrease with most scale-up criteria. N will have a powerful, non-linear effect on Fr , causing Fr to decrease with increasing volume, even though D is increasing. Thus, scale-up based on equal Fr is rarely used as a scale-up criterion because it results in a relatively large and expensive industrial mixer.

- **The power number**, N_p , which is a function of the Reynolds number and the Froude number:

$$N_p = \frac{P g_c}{\rho N^3 D^5}$$

The power number correlation has been used successfully for impeller geometric scale-up²⁶.

- **Impeller tip speed**, S_t [rad/s], is a common scale-up criterion for industrial mixers, often associated with shear-sensitive mixing phenomena, such as particle or droplet-size control:

$$S_t = \pi N D$$

- **Torque per volume**, T/V [(N·m)/m³], is a measure of torque invested by a fluid mixer per unit of mixed volume. T/V is a practical and common scale-up criterion for fluid mixers because it relates directly to the size and torque capability of the mixer.
- **Power per volume**, P/V [W/m³], is probably the most commonly used criterion in mixing because it is easily understandable and practical. To calculate P/V , rearrange the power number equation to solve for P :

$$N_p = \frac{P g_c}{\rho N^3 D^5} \rightarrow P = \frac{N_p \rho N^3 D^5}{g_c}$$

where P is power and g_c is a gravitational conversion factor.

Other advantages of using P/V as a scale-up criterion are that it correlates well with mass-transfer characteristics in the mixer, and it is conservative enough to provide adequate

performance in production-scale equipment — particularly when no other strong correlating parameter has been determined from small-scale testing²⁶.

Approximately other half a dozen dimensionless numbers are involved in the various aspects of mixing, heat and mass transfer, etc.²⁵ In most scale-up situations, however, total similarity on different scales cannot be reached, as it is difficult or even impossible to maintain all the dimensionless groups that characterise the process. In these cases, a trade-off between different dimensionless groups has to be found, with groups being “weighted” differently according to their expected influence on the process. Alternatively, a mathematical model can be developed that accounts for the physical and chemical processes considered important for scale-up. For this purpose, the process mechanisms have to be clearly understood and the model must not contain any phenomenological or unknown scale-dependent parameters, as it is not then suitable for quantitative scale-up predictions.²⁴

Taking into account the large amount of scale-up rules of thumb and the emulsification system available, it was considered to follow Gorsky scale-up approach²⁵, which summarises the previous dimensionless numbers in the scale-up model of the power law relationship $N D^\alpha$, where the power law exponent α has a definite physical significance as shown in Table 1, N is the stirring rate, D the impeller blade diameter. Therefore,

$$N_2 = N_1 \left(\frac{D_1}{D_2} \right)^\alpha$$

Where ₁ and ₂ means two different scales.

The correlation between Gorsky model and the dimensionless numbers can be proved, such as the Froude number ($D_1 N_1^2 = D_2 N_2^2$) can be reorganised as $N_2 = N_1 \left(\frac{D_1}{D_2} \right)^{1/2}$ where $\alpha = 1/2$ or the impeller tip speed ($D_1 N_1 = D_2 N_2$) can be written as $N_2 = N_1 \left(\frac{D_1}{D_2} \right)$ where $\alpha = 1$.

The value of α and its corresponding significance are determined either empirically or through theoretical means.

Table 1. Common values assigned to the power law exponent α when comparing large- to small-scale equipment²⁵

α	Physical interpretation
0	Equal blend time
1/2	Equal surface motion
2/3	Equal mass transfer rates or equal power per unit volume P/V
3/4	Equal solids suspension
1	Equal liquid motion (equal average fluid velocity)

1.3. Experimental design

The design of experiments DOE²⁷ is an efficient procedure for planning experiments so that the data obtained can be analysed to yield valid and objective conclusions. The great advantage of using DOE is that it provides an organised approach, with which it is possible to address both simple and tricky experimental problems. The experimenter is encouraged to select an appropriated experimental objective, and is then guided to devise and perform a set of experiments, which is adequate for the selected objective. Experience shows that DOE requires fewer experiments than other approaches. Since these few experiments belong to an experimental plan, they are mutually connected and thereby linked in a logical and favourable manner. Thus, one obtains more useful and more precise information about the studied system, because the joint influence of all factors is assessed. After checking the model adequacy, the importance of the factors is evaluated in terms of a plot of regression coefficients, and interpreted in a response contour plot or response surface²⁸.

The design of the experiment begins with determining the objectives of an experiment and selecting the process factors for the study. An experimental design is the laying out of a detailed experimental plan in advance of doing the experiment. The choice of an experimental design depends on the objectives of the experiment and the number of factors to be investigated.

The method chosen in this experimental study is the response surface method (RSM). Good RSM designs have to allow the estimation of the parameters of the model with low uncertainty, which means that we want the confidence intervals of the regression coefficients to be as narrow as possible. Good RSM designs should also give rise to a model with small prediction error, and

permit a judgement of adequacy of this model. This latter aspect means that the design must contain replicated experiments enabling the performance of a lack of fit test. In addition, good RSM designs should encode as few experiments as possible.

The suitable type of design in this work is the central composite design (CCD) of three levels and three factors plus the star design (actually five levels taking into account the star design), which consists of three building blocks, (i) eight factorial experiments, (ii) six axial experiments –star points–, (iii) and the centre-point, at least replicated once. It is depicted in Figure 9.

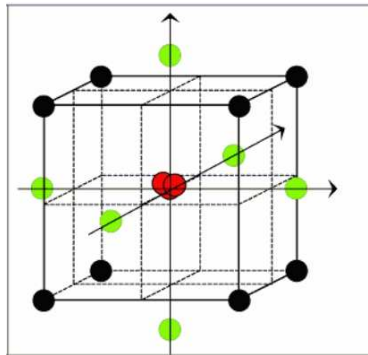


Figure 9. CCD design + star points²⁸

Once the models are obtained, a validation process is carried out performing new experiments within the experimental range in order to corroborate the validity of the model. In fact, that is the aim of this work. A simple experimental design (varying only one factor and remaining constant the others) is developed so as to extend the number of experiments and to ensure that the model's prediction agrees with the experimental results. In addition to that, the experimental range of the stirring rate N has been broadened from the previous work interval to lower values, so as to develop a more accurate study of the scale-up.

2. Objectives

The main goals of this project are:

- (1) to validate the empirical models at small and medium scale that describe the emulsion features, obtained in the preparation of W/O HIPRE and
- (2) to determine a scale-up model for this kind of system, from the experiments at three scales, and determine the scale invariants.

To achieve these goals, the following specific objectives are proposed:

- Determine the validity of the models in the range of the process variables within the levels chosen in previous studies, in both small and medium scale. To do this, additional and different experiments from the ones used to determine the models will be carried out. The response variables chosen are droplet size, stability and rheological parameters (yield stress, storage modulus, viscosity...)
- Determine the destabilization mechanisms from light scattering measurements (variation of back scattering) and correlate them with preparation and composition variables.
- Determine the validity of the scale-up model obtained using the small and medium scale by doing experiments in the large scale.
- Calculate the empirical scale invariant from the models at small and medium scale.
- Calculate the scale invariant from the experimental values at the three scales for a given set of conditions. The influence of the variation of the addition time t (or addition flow rate Q) and the surfactant concentration S/O (remaining the other factor constant) is analysed.
- Calculate the global empirical scale invariant, and then, obtain a model for each rheological parameter which include all the experiments performed
- Explain the physical significance of the power law exponent α of the scale invariant.

3. Materials and methods

3.1. Materials

The continuous phase of the emulsion is dodecane (99.5 %) and the surfactant is Span80® (in Table 2, the physical properties are shown), both were purchased from *Sigma-Aldrich*. The deionised *Milli-Q* water constitutes the dispersed phase (88 % vol/vol, 90 % wt/wt).

Table 2. Physical properties of Span80® from Sigma-Aldrich catalogue²⁹

Commercial Name	Span80®
Name	Sorbitane monooleate
Type	Non ionic
Empirical Formula	C ₂₄ H ₄₄ O ₆
Molecular Weight	428.60
HLB value	4.6 ± 0.1
Density	0.99 g/mL at 20 °C

3.2. Methods

3.2.1. Preparation of HIPREs

The W/O HIPREs of this work are constituted by a 90% wt/wt ($\phi = 0.88$) of water (dispersed phase) and the concentration of surfactant in the continuous phase (dodecane, Span 80) is left as a composition variable to study.

The experimentation system, in each of the three geometrically-similar scales, consists of a glass jacketed vessel and a three-level P-4 pitched blade impeller. The dispersed phase is added by a peristaltic pump (*ISMATEC Reglo* used in small scale and *ISMATEC MCP* used in both medium and large scales) to control properly the flow rate. A thermostatic bath (*HAAKE F6-C35* used in both small and large scale; *HUBER Ministat 230*, in medium scale) regulates the temperature of the refrigeration fluid (*Milli-Q* water, ethylene glycol) at 25 °C. The digital laboratory stirrer *IKA Eurostar power control-visc (IKA)* sets the stirring rate.

In Figure 10 (A), a sketch of the vessel is depicted; in Figure 10 (B), the three jacketed stirring tanks are presented; and in Table 3, the geometric dimensions of the three vessels and respective impellers used are shown.

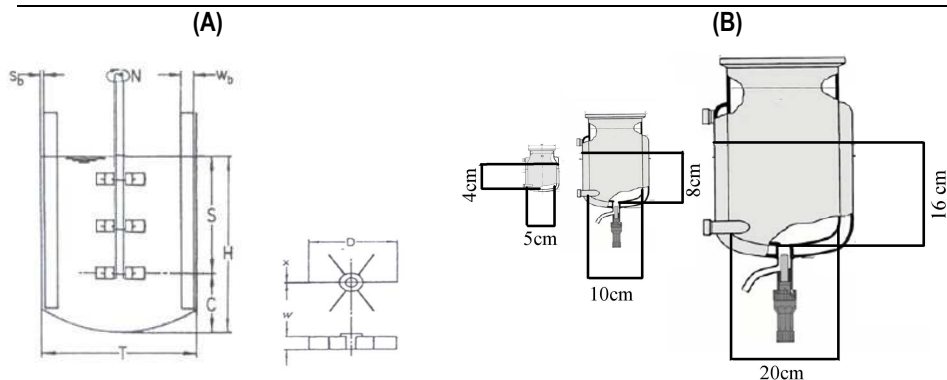


Figure 10. (A) Sketch with the characteristic dimensions of a stirred tank and three level P-4 pitched blade impeller. (B) Liquid height and tank diameter of each scale.

Table 3. Characteristic dimensions of the three scales. Notation as in Figure 10 (A).

Scale	V (mL)	D (cm)	T (cm)	H (cm)	D/T	H/T	T/T_{small} H/H_{small}
Small	78	4.5	5	4	0.9	0.8	1
Medium	628	9	10	8	0.9	0.8	2
Large	5026	16	20	16	0.8	0.8	4

Firstly, to prepare the continuous phase, the amount of surfactant and oil are weighed and mixed and when the dissolution is completely homogeneous, the mixture is introduced into the vessel, which is already at the desired temperature. Figure 11 (A) shows the equipment available to prepare the emulsions and Figure 11 (B), the different impellers used at each scale. The impeller is placed slightly above the continuous phase in order to prevent the friction between the metallic blades and the glass wall and to start the emulsification as early as the dispersed phase is transferred into the vessel. The stirring rate N (rpm) and the addition flow rate Q (mL/min) are fixed according to the experimentation plan. Before starting the addition of the dispersed phase, the agitation speed N is set and the temperature of the refrigeration fluid is checked. The peristaltic pump provided a controlled and constant flow rate. During the addition of the dispersed phase, this should not flow through the tank walls but should be introduced directly into the continuous phase in order to ensure the correct emulsification.

Once all the dispersed phase is added, the emulsion is stirred at the same agitation speed for 5 more minutes in order to homogenise the emulsion (ensure the incorporation of all the dispersed phase).

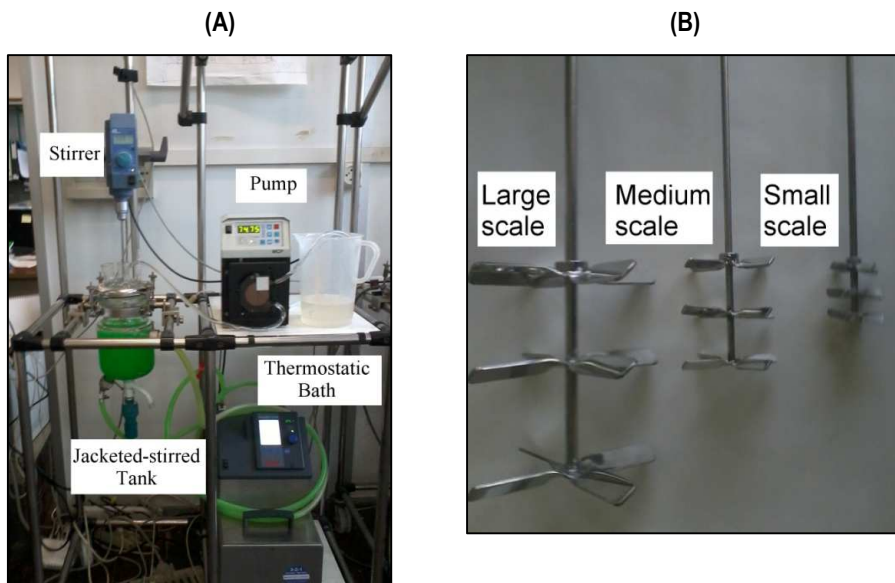


Figure 11. Equipment used to carry out the study at medium scale (A); impellers used at each scale (B)

The torque T supplied by the agitator is measured along all the process duration. The data is collected in *LabWorldSoft® (IKA)* software to be analysed and then depicted as a function of time.

3.2.2 Characterisation of HIPRE

3.2.2.1. Rheological parameters

The rheological tests were performed in *HAAKE Mars III Rheometer (Thermo Fisher Scientific)* and data were collected in *HAAKE RheoWin Job Manager* and were visualised and saved in *HAAKE RheoWin Data Manager*. A 35 mm serrated plate-plate geometry to avoid slippage of the emulsion and with a gap of 0.5 mm was used. All the tests were performed at 25 °C (regulated by *HAAKE C25-F6* thermostatic bath).

Modern rheometers can work in two test modes, CS in which a controlled stress input τ is provided and the resulting shear rate $\dot{\gamma}$ is determined, or on the other hand, CR where the rheometer provides a controlled shear rate input and the consequent shear stress is determined. The suitability of each mode depends on the test performed, as it is showed in Table 4 with further parameters fixed in each test.

Table 4. Characteristic parameters of each rheological test

Test	Mode	Measured variable	Independent variable		Fixed variable	Steps	Step Duration
			From	to			
Steady Shear	CS	$\dot{\gamma}$	$\tau = 0.01 \text{ Pa}$	$\tau = 100 \text{ Pa}$		50	10 s
Oscillatory Shear	CS	G', G''	$\tau = 0.1 \text{ Pa}$	$\tau = 1000 \text{ Pa}$	$\omega = 1 \text{ Hz}$	200	
Frequency Sweep	CS	G', G''	$\omega = 100 \text{ Hz}$	$\omega = 0.01 \text{ Hz}$	$\tau = 1 \text{ Pa}$	30	
Viscosity vs Shear rate	CR	η	$\dot{\gamma} = 0.001 \text{ s}^{-1}$	$\dot{\gamma} = 100 \text{ s}^{-1}$		30	60 s

3.2.2.2. Stability analysis

The *TurbiScan MA 2000* measures the back scattering *BS* of concentrated dispersions over time, which is used as an approach to stability, and is used to determine the mechanisms driving to destabilization.

The sample to be analysed is contained in a cylindrical glass measurement cell. The analyzer (Figure 12) consists of a reading head that moves along a cylindrical cell to scan the entire sample length. The reading head consists of a pulsed near infrared light source ($\lambda = 850 \text{ nm}$) and two synchronous detectors ³⁰:

- The transmission detector receives the light which goes through the sample (0°)
- The back scattering detector receives light backscattered by the sample (135°)

Thus the device provides transmission and back scattering profiles giving the transmitted and backscattered light flux (% , relative to external standards) as a function of the sample height (mm).

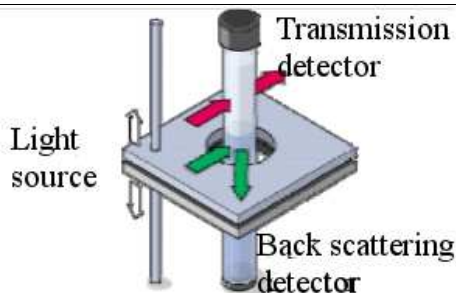


Figure 12. Principle of *Turbiscan MA 2000* measurement²⁰

The portion of emulsion which is analysed is extracted from the whole emulsion into a 5 mL syringe with no needle. A plastic tube, as long as the cylindrical glass measurement cell, is fixed in the orifice of the syringe and the other extreme of the tube is placed on the base of the cylindrical cell. Then, the emulsion is carefully expelled avoiding the formation of air bubbles, which would distort the measurement. Finally, the measurement cell is plugged, introduced inside the device *Turbiscan MA 2000* and a light scanning is carried out every two minutes for 30 minutes. Moreover, the evolution of the stability is measured every 24 hours taking a light scanning test.

3.2.2.3. Droplet size and polydispersity

The droplet size was obtained by statistical methods after counting more than 600 droplets of each emulsion.

Using a spatula, a slight portion of emulsion is extracted –it is preferable to take the sample on the bulk of the emulsion rather than on the surface to ensure a complete homogenization of the emulsion– and is laid on a microscope slide 26x76 mm (*Deltalab*). Then, a cover glass 20x20 mm (*Deltalab*) is placed above the sample and it is pressed against the slide in order to achieve the thinnest layer of emulsion between them and to take pictures in which droplet borders are clearly defined.

The optical microscope *Optika Microscope*, which is equipped with the camera *Moticam 2300 3.0 MP Live Resolution (Motic)*, allows to take photographs at 400x to then measure the diameter of a significant number of droplets of each emulsion using *Motic Images Plus 2.0* software (*Motic*).

3.2.3. Experimental design

The models which will be validated were obtained at each scale (small and medium) carrying out a rotatable central composite design (CCD): 2^3 +star design, with two centre points. The experimental factors which remain constant at small and medium scale are three, the addition time t , the surfactant concentration as a ratio between surfactant and oil S/O and the stirring rate N . Due to the different effective volume V of each scale, while the addition time t will be equal at both scales, the addition flow rate Q will differ (defined as $Q = V/t$). 16 runs were required at each scale and at medium scale each one was replicated once.

Two models are obtained, the general model (all the factors with quadratic interactions) and the significant model (only the significant factors -the variables whose p-value is smaller than 0.05 in the general model).

The validation of the models consists on a simple experimental design, in which only one factor is varied within the experimental range and the others two remain constant.

4. Results and discussion

4.1. Validation of the models at each scale

4.1.1. Validation of the models at small scale

4.1.1.1. Models at small scale

As a previous work, these polynomial models –general and significant ones- (see Appendices A 1.1.) were obtained as a result of a central composite design. The factors and levels chosen are shown in Table 5. The validation of models consists of performing experiments in which two factors remain constant and the value of the third one whose influence will be discussed, is varied. Figure 13 shows graphically the levels used for the validation. The experiments carried out are shown in Appendices A 1.3.1.

Table 5. Factors and levels at small scale.

Factors	Low	High	Centre
Water volume fraction ϕ	0.88	0.88	0.88
S/O (wt/wt)	0.177	0.357	0.267
N (rpm)	700	1400	1050
t (min)	8.75	3.5	5
Q (mL/min)	8	20	14

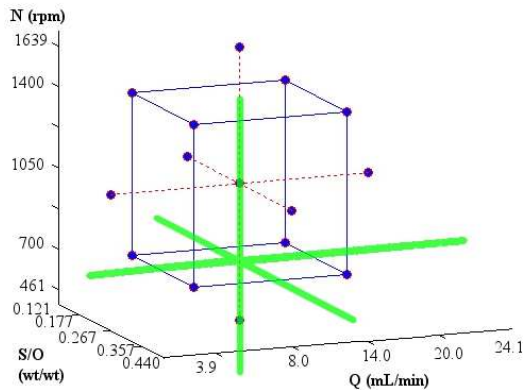


Figure 13. Graphical representation of the experimental design and validation experiments (green straight lines) at small scale

4.1.1.2. Influence of stirring rate at small scale

The surfactant oil ratio was fixed at $S/O = 0.267 \pm 0.020$ and the addition flow rate at $Q = 14 \text{ mL/min}$. The six experiments were performed fixing the agitation rate N from 350 rpm to 1485 rpm.

Rheological parameters

The effect of the stirring rate N on the emulsion rheological behaviour is undeniable: with an increase in the stirring rate, the elastic portion of the emulsion increases, the emulsion is more consistent. It is reflected in the yield stress τ_0 and critical yield stress $(\tau_0)_c$, the stress that the emulsion requires to flow is proportional to stirring rate. However, the models of τ_0 (Figure A 1, Appendices A 1.4.) do not fit with the results (their values are smaller than the models predict). As discussed in the introduction, the τ_0 value is obtained from the intersection of two linear regressions as to obtain the model. Although the method is subjective -depending on the values chosen, the values can slightly differ from one experimenter to others-, the difference between models and experimental result is considerably higher. There is no clear reason to justify this fact, the only plausible one is that we have used different rheometers, and the settings might not have been the same. Figure 14 shows the steady shear test from which τ_0 is obtained, at different stirring rates.

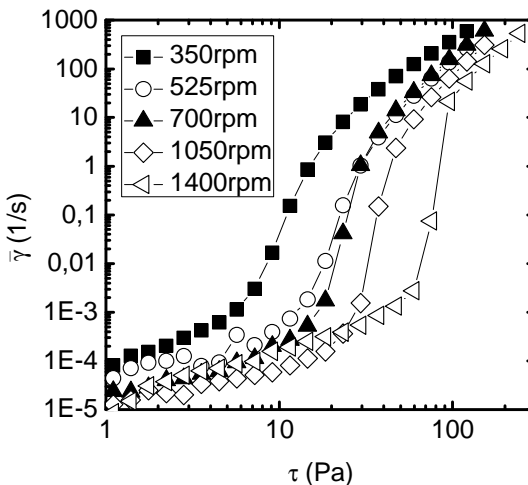


Figure 14. Steady shear test at equal S/O and Q . The stirring rate N varies from 350 rpm to 1400 rpm.

However, $(\tau_0)_c$ (Figure A 2) results fit with the general model at intermediate stirring rates N , yet at lower values (out of the range of application of the model), while the general model predicts a constant value, the experimental values are lower. The significant model even shows a decrease in the value at lower N but the experimental result is lower. At higher stirring rates N , even though a replication fits utterly with both models, the other two are below it. To sum up, the experimental value seems to follow a behaviour that could resemble a logarithmic curve rather than the exponential curve depicted by both models.

Another evidence of the increase of the solid-like behaviour of the sample is the value of the storage modulus G' at $\tau = 1$ Pa at a wide range of frequencies ω (Figure A 3) which rises considerably (at 350 rpm, $G' = 100$ Pa; at 1400 rpm, $G' = 500$ Pa). Results show the general model does not have to be extended out of the experimental range (< 461 rpm), while the model predicts the value of G' to not vary significantly below 461 rpm, experimental results show the contrary. Nevertheless, the significant model predicts better the value out of the experimental range but at higher N , the same as in the general model happens. Even the experimental values can be fitted with a logarithm curvature regression rather than with the regressions obtained with both the general model (slightly exponential curve) and the significant model (straight line), it seems that at high N , the values do not rise as sharply as at lower N .

The same occurs with the loss modulus at the critical yield stress G''_{max} (Figure A 4), the slope of the graphical depiction decreases with the stirring rate N . The models indicate a continuous growth, but as it happens with the previous rheological parameters, the experimental values can be fitted to a logarithm curve. Nevertheless, the general model predicts properly the value at stirring rates N out of the experimental range, in fact, at $N = 350$ rpm the value provided by the model and the experimental one are the same. The significant model shows higher values than the general one, so it is worse than the general model.

Viscosity (Figure A 5) increases up to 1050 rpm, and at higher stirring rates N , the values seem to not be affected by N , even though in the model viscosity increases. At energy input below the experimental range, viscosity decreases more sharply than the model predicts.

Stability analysis

The stability with time increases (relative back scattering drops slower) with the agitation rate N (Figure A 6). The graphical representation of the BS versus cell position (Figure A 7) shows at

high N ($N = 1485$ rpm) the main destabilization mechanism is coalescence because BS decreases as a front along the sample, even though creaming also occurs (a zone of clarification appears at the bottom of the cell after 10 days). At low N ($N = 350$ rpm) (Figure A 8), coalescence has an important role in the destabilization but creaming and sedimentation as well, due to the separation into two phases (the trench in BS profile).

Droplet size and polydispersity

Droplet size is measured from mean diameter d_{10} and Sauter mean diameter d_{32} (Figure A 9), both parameters decrease with stirring rate N as in the models. Although the behaviour is coincident (a decrease of droplet size with stirring rate N), the Sauter mean diameter of the model at low N is three times the experimental one. There is no further difference between the significant and the general models. The same happens with d_{10} , in comparison with the values of the experiments in the previous work.

The surface area of dispersion a_v (Figure A 10 (A)) due to its dependence of d_{32} and the dispersed phase volume fraction ϕ –which remains constant– possess the inverse behaviour than d_{32} , a rise with the stirring rate N . All the emulsion are polydispersed ($cv > 0.2$), the coefficient of variation cv (Figure A 10 (B)) is found between $cv = 0.5$ and $cv = 0.9$.

Summary

An increase of the energy input gives to the emulsion stronger elastic properties. The more solid-like behaviour of the emulsion is clearly related with the stirring rate N . A higher stirring rate N favours the breakup of the dispersed phase into finer droplets. The interaction among the fine droplets forming a compact packing provides to the emulsion more elastic properties.

4.1.1.3. Influence of addition time at small scale

The stirring rate was set at $N = 700$ rpm and the surfactant concentration at $S/O = 0.267 \pm 0.020$. The addition flow rate values in the five experiments carried out are varied in the interval 3.9 mL/min – 24.1 mL/min, giving a total addition time between 18.24 min and 2.93 min, respectively.

Rheological parameters

The properties of the emulsion are hardly influenced by the addition time t (or addition flow rate Q). Although a drop in the addition time implies the viscous behaviour of the emulsion to increase, the difference between the extreme values of each rheological parameter is small.

Focusing on yield stress τ_0 (Figure A 11) and critical yield stress $(\tau_0)_c$, their values are lower at high addition flow rate Q (low addition time t). As in the influence of stirring rate N , τ_0 models predicts a value higher than the experimental one. Even though, the behaviour of the results is the same than the models one.

The $(\tau_0)_c$ (Figure 14) values do not fit with any models but the general model follows a completely different behaviour than the significant one, since the significant model is not a function of the addition flow rate Q , so the value is mainly constant along the experimental range, even though the representation of the general model decreases sharply up to 20 mL/min and then, increases its value. Therefore, the significant model defines better the behaviour of the experimental values, yet the experimental values are below the model curve.

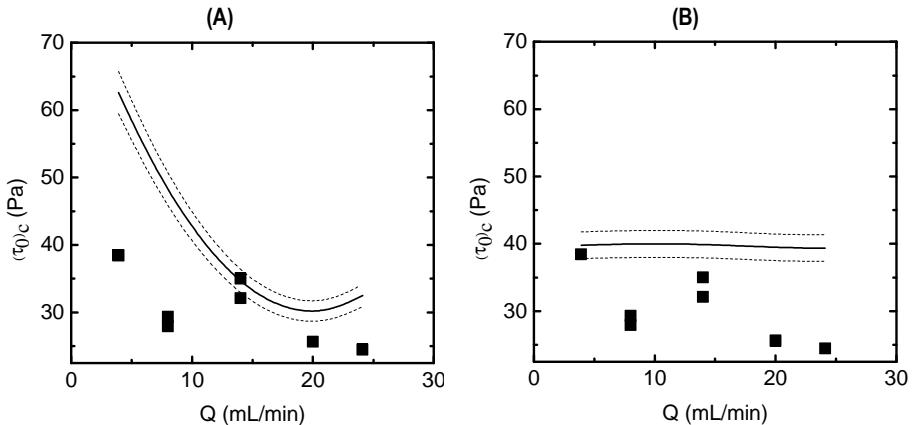


Figure 15. Critical yield stress $(\tau_0)_c$ at equal S/O and N at small scale. **(A)**, general model; **(B)**, significant model.

The storage modulus G' at a fixed stress $\tau = 1$ Pa follows the same behaviour as the parameters discussed previously. In this case, experiments confirm the validity of the general model prediction from $Q = 15$ mL/min, yet below this flow rate, although the values of the model rise, the experimental ones show a not so sharp growth. However, the significant model predicts utterly the values up to $Q = 15$ mL/min. Therefore, we can confirm that up to $Q = 15$ mL/min, no

dependence between Q and G' exists but at higher Q , the dependence is considerable. Figure 18 shows both models.

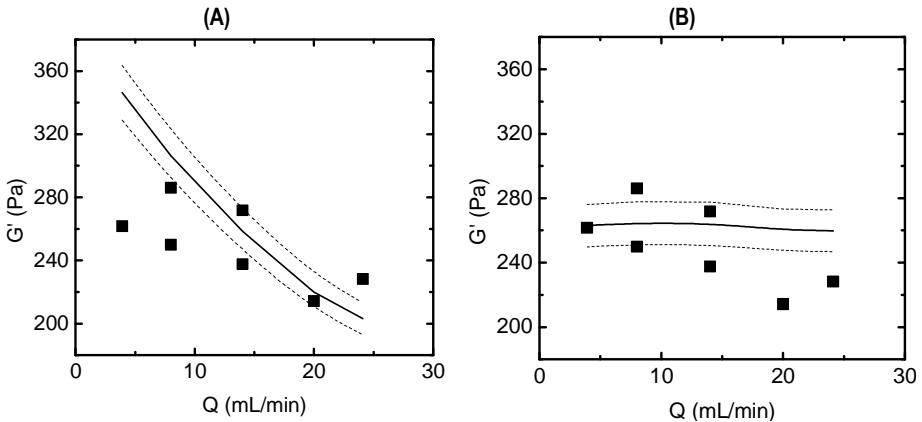


Figure 16. Storage modulus G' at equal S/O and N at small scale. (A), general model; (B), significant model.

The loss modulus at the critical yield stress G''_{max} (Figure A 12) decreases with the addition flow rate Q . While the significant model shows a linear decrease with addition flow rate Q , the general one predicts a sharply decrease at lower Q and then at higher Q , G''_{max} remain constant. Although the experimental results up to $Q = 10$ mL/min fits perfectly with the general model, at higher Q , the experimental values are higher than both models predictions but the behaviour of the experimental values is similar to the general model (a stabilization of the value at higher Q). However, the significant model does not predict accurately neither the behaviour nor the proper values.

Finally, viscosity (Figure A 13) corroborates as well what has been discussed, the model and the experimental values decrease slightly with the addition flow rate Q .

Stability analysis

The variation of BS with time in all the range of addition flow rate Q is thoroughly similar (Figure A 14). In Figures A 15 and A 16, the variation with time of BS versus cell position in the experiment at $Q = 3.9$ mL/min and $Q = 24.0$ mL/min, respectively, are depicted. From these graphs, the mechanism of destabilization can be clearly analysed. After the emulsion being prepared (from purple to green lines), the main mechanism is coalescence so that the BS decreases homogeneously along the cell length as a front. However, after a long time (38 days, to be more

precise), while coalescence has continued affecting the sample, creaming and sedimentation have been developed, the trench in the graph shows the separation of the sample into two phases -one richer in water (denser) and the other richer in oil (less dense).

Droplet size and polydispersity

The experimental Sauter mean diameter d_{32} (Figure A 17 (A)) does not fit with the model as happens in all experiments (the experimental value is three times higher than what the model predicts), but the behaviour is comparable. The droplet size d_{10} (Figure A 17 (B)) does not change its value significantly with the addition rate but the Sauter mean diameter d_{32} does not vary with the addition flow rate Q up to $Q = 10\text{mL/min}$, but at higher Q , d_{32} slightly increases. In previous models, Q did not have a significant effect on droplet size.

Due to the little variation between the extreme values, the polydispersity as coefficient of variation cv (Figure A 18 (A)) –around 0.85- is similar in all the experiments, so emulsions are clearly polydisperse ($cv > 0.2$). However, the surface area of dispersion a_v (Figure A 18 (B)) presents further variability owing to its dependence of d_{32} , in fact, a_v decreases increasing the addition flow rate Q .

Summary

Remaining the energy input (stirring rate N) constant, if the addition flow rate is less (addition time t high), the ratio between energy used to disperse the water and the amount of water is higher, so the droplets of the dispersed phase are finer because more energy can be used to break-up the large droplets added. Therefore, increasing the addition flow rate Q or reducing the addition time t implies a slightly decrease of the solid-like behaviour of the emulsion. The results show below $Q = 10\text{ mL/min}$, the properties of the emulsion do not differ significantly with the addition flow rate Q . At higher Q , the properties change but not so remarkably than with the stirring rate or concentration of surfactant.

4.1.1.4. Influence of S/O rate at small scale

The stirring rate was fixed at $N = 700\text{ rpm}$ and the addition flow rate at $Q = 14\text{ mL/min}$. The five experiments were performed varying the surfactant concentration, expressed as a ratio between surfactant and oil S/O between 0.121 and 0.440.

Rheological parameters

An increase of the surfactant concentration S/O as the ratio between surfactant and oil in the emulsion produces a stronger solid-like behaviour of the emulsion.

Firstly, the graph of the yield stress τ_0 (Figure A 19) shows that the results follow the same behaviour as the general model –the slope of the regression decreases with the surfactant oil ratio S/O - but not the significant one (raising straight line). On the other hand, $(\tau_0)_c$ values (Figure A 20) are not properly predicted in any model. The behaviour is like the τ_0 general model, so both the general model (a decrease up to a minimum and then a sharply increase with S/O) and the significant one (rising straight line) do not define properly the values. In all cases, the experimental values are lower than the prediction of the models.

Both models of the storage modulus G' (Figure 17) predict a linear proportion between G' and the concentration of surfactant S/O . Nevertheless, the significant model predicts perfectly the values up to $S/O = 0.3$ and on the other hand, the general model predicts completely the values from $S/O = 0.3$. Both models are function of surfactant concentration, so at lower S/O , the storage modulus varies linearly with surfactant concentration, yet at higher S/O , the quadratic interactions are slightly more important.

Figure 18 shows that the storage modulus G' does not vary significantly along the frequency range, as discussed in the introduction, so G' can be obtained as the average of all the values in this frequency range.

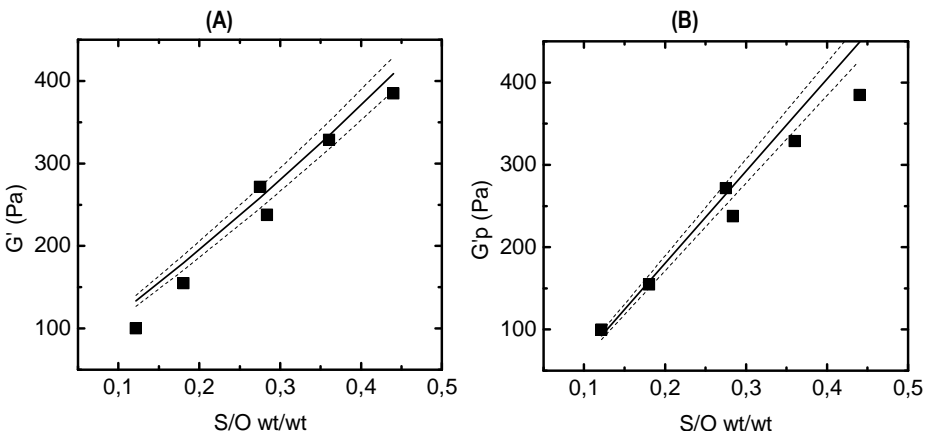


Figure 17. Storage modulus G' at equal Q and N at small scale. (A), general model; (B), significant model.

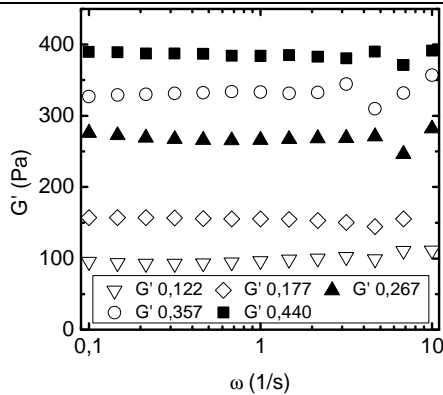


Figure 18. Frequency sweep test to obtain storage modulus G' at different S/O (from 0.122 to 0.440)

The loss modulus at the critical yield stress G''_{max} (Figure A 21) follows an almost proportional relation (with a slight degree of convex curve) behaviour with the surfactant concentration. The general model predicts a slightly-exponential-like behaviour (the extreme values fit perfectly with the general model but the intermediate values do not). On the contrary, the significant model predicts correctly the behaviour and even the values (they are slightly higher than the experimental ones at higher S/O).

The model of viscosity (Figure A 22) predicts the behaviour of the experimental values but not the proper values. As the surfactant concentration S/O increases, the growth of the value of viscosity is tempering.

Stability analysis

The main function of the surfactant is to stabilise the droplets against coalescence once they are formed. As Figure 19 (A) shows, the *relative BS* (stability) a few minutes after the preparation decreases slower in emulsions with higher surfactant concentration, confirming that the more surfactant there is, the more stable the emulsions are. Figure A 23 shows the *relative BS* 30 min and 24 h after preparation.

However, many days after Figure 19 (B), we see that the emulsion with $S/O = 0.177$ seems to be the most stable one, since the change in *relative BS* is the lowest. This could indicate the existence of an optimum surfactant concentration which stabilises better the emulsion with time. Therefore, although after the emulsion preparation, the surfactant plays an important role in

stabilization, by observing the emulsion after a long period of time, there could be an optimum concentration that maximise stabilisation.

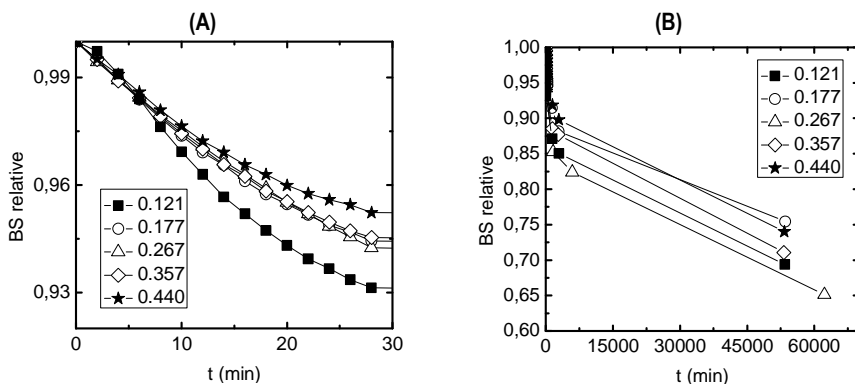
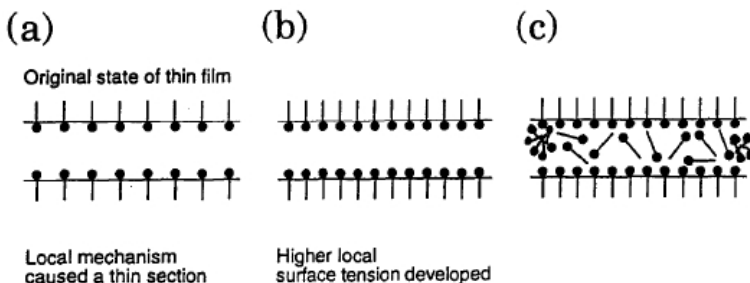


Figure 19. Evolution of relative back scattering with time. **(A)**, the whole interval; **(B)**, only the first 30 min.

If a surfactant stabilised film undergoes a sudden expansion, the immediately expanded portion of the film must have a lower degree of surfactant adsorption than unexpanded portions because the surface area has increased. This causes an increased local surface tension which produces immediate contraction of the surface. Thus, the contraction of the surface induces liquid flow from the low tension region to the high tension region to restore equilibrium, this is termed Gibbs - Marangoni effect³¹. If the surfactant concentration is too low (Figure 20a) to form a resistant protective layer around the droplets, droplets tend to coalesce as they collide. In the case of the continuous phase being too concentrated (Figure 20c), the differential tension relaxes too rapidly because of the supply of surfactant which diffuses to the surface. This causes the restoring force to have time to counteract the disturbing forces and producing a dangerously thinner film which could lead to drop merge (coalescence)³². Therefore, an optimum of surfactant (Figure 20b) concentration to maximise stabilization over time would exist³³.



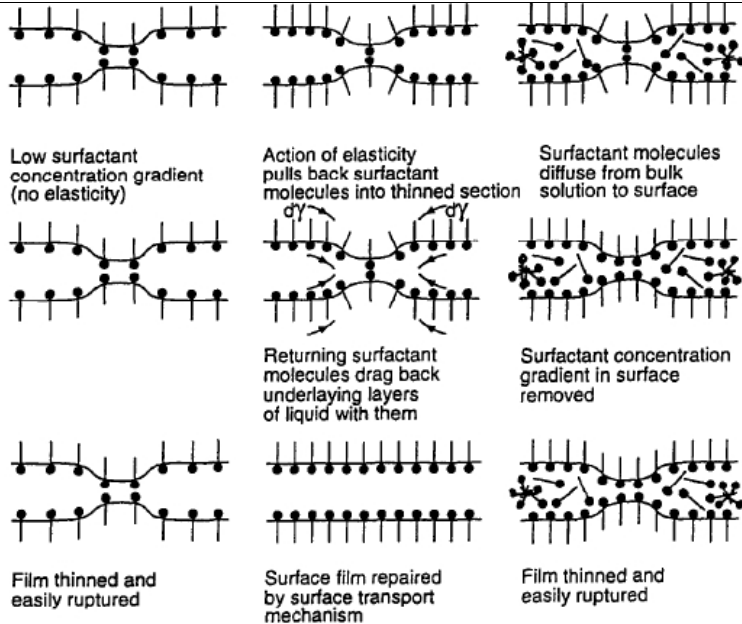


Figure 20. Gibbs-Marangoni mechanism of dynamic stability. Adapted from Pugh³²

The variation with time of BS versus cell position at the highest and lowest surfactant concentration emulsion is depicted in Figure A 24 and A 25. The behaviour of both samples is identical. The BS decreases with time, which means that coalescence is occurring-, moreover, a clarification zone appears, indicating slight separation of phases. Despite this fact, it is remarkable that after 37 days, the majority of the emulsions remain stable with no phase separation.

Droplet size and polydispersity

The Sauter mean diameter d_{32} (Figure A 26 (A)) decreases slightly from 3.5 μm to 2.5 μm and the mean diameter d_{10} (Figure A 26 (B)) remain constant in all the range of surfactant concentration S/O around $1.4 \pm 0.3 \mu\text{m}$. Figure 21 and 22 show the images from the optical microscope at $S/O = 0.420$ (where the droplets seem finer) and $S/O = 0.121$, respectively. However, the model predicts wider droplets and a linear decrease with the surfactant concentration S/O . Assuming that the rheological parameters are influenced by the surfactant concentration S/O , a difference in the droplet size as the model predicts would be observed. The surface area of dispersion a_v (Figure A 27 (A)) rises with an increase of the surfactant concentration S/O (from 1.6 to 2.1 μm^{-1}). Moreover, polydispersity is the same in all emulsions because all experimental diameters are

alike. The coefficient of variation cv (Figure A 27 (B)) is around 0.8, so the emulsions are polydisperse.

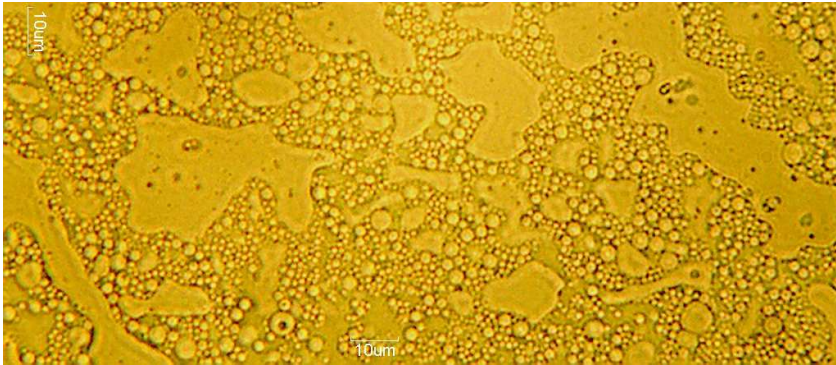


Figure 21. Image obtained with the optical microscope . $S/O = 0.420$, $Q = 14$ mL/min , $N = 700$ rpm.

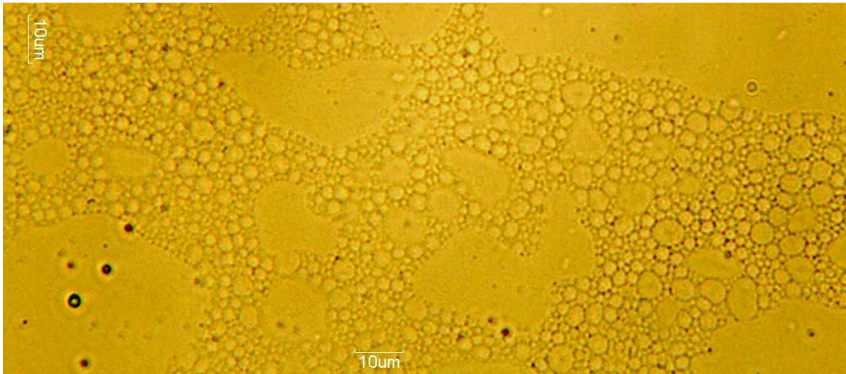


Figure 22. Image obtained with the optical microscope $S/O = 0.121$, $Q = 14$ mL/min , $N = 700$ rpm.

Summary

The more surfactant there is, in the range studied, the more stable emulsions are a few minutes after preparation. If the interfacial tension is reduced, finer droplets can be formed because less droplet area is required to have a stable emulsion. In fact, the surface area of dispersion a_v (interfacial area of dispersed phase per unit volume of the whole dispersion) proves that at higher surfactant concentration S/O , the surface area of dispersion is higher than at lesser S/O because the concentration of surfactant allows the existence of smaller droplets (with the same amount of dispersed phase, there are more droplets). Therefore, the interfacial area per unit of volume is higher as the results show.

4.1.2. Validation of the models at medium scale

4.1.2.1. Models at medium scale

The polynomial models (general and significant ones) that are going to be validated are shown in Appendices A 1.2. In Table 6 the factors and levels at this scale are shown. Figure 23 depicts the validation experiments following the same procedure as at small scale. The experiments performed are presented in Appendices A 1.3.2.

Table 6. Factors and levels at medium scale

Factors	Low	High	Centre
Water volume fraction ϕ	0.88	0.88	0.88
S/O (wt/wt)	0.177	0.357	0.267
N (rpm)	700	1400	1050
t (min)	8.75	3.5	5
Q (mL/min)	64	160	112

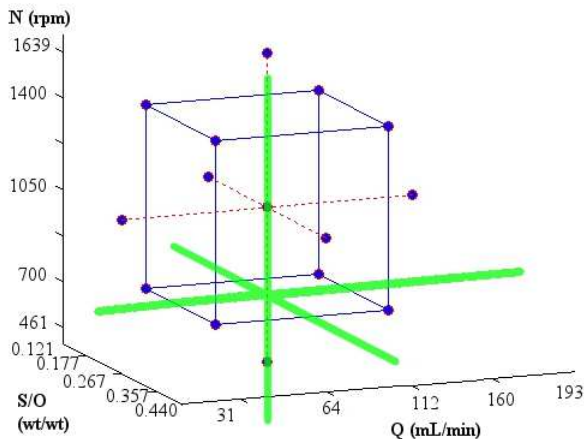


Figure 23. Graphical representation of the experimental design and validation experiments (green straight lines) at medium scale

4.1.2.2. Influence of stirring rate at medium scale

The surfactant-to-oil ratio was fixed at $S/O = 0.267 \pm 0.020$ and the addition flow rate at $Q = 112 \text{ mL/min}$. The agitation rate N was varied in the range from 350 rpm to 1400 rpm (five experiments).

Rheological parameters

The stirring rate N is the variable that has a greater influence on the rheological parameters. In fact at higher energy inputs, the elastic properties of the emulsion are more prominent. The models of the yield stress τ_0 (Figure A 28) and of the critical yield stress $(\tau_0)_c$ (Figure A 29) do not fit with the experimental values (are lower in all the surfactant concentrations).

At higher stirring rate N , while τ_0 and $(\tau_0)_c$ models and τ_0 experimental results seem to slow its growth, the experimental values of $(\tau_0)_c$ maintain the same lineal behaviour in all the range. Moreover, there is no difference between the general and the significant models, so the yield stress is defined by a non-quadratic function.

Focusing on the storage modulus G' (Figure A 30), the models propose that G' grows linearly. The behaviour is similar and a concordance between the general model and the experimental results exists. In this case, the general model can be extended below the experimental range because of the linearity, which is maintained. Moreover, the general model and the significant one are identical, so the other factors (non-significant) do not interfere in the variable.

The behaviour of the loss modulus G'' at the critical yield stress G''_{max} (Figure A 31) is the same as the storage modulus G' —a linear increase with N —. However, both models show a high-slope logarithm-like behaviour (as τ_0 and $(\tau_0)_c$), so at low stirring rate N , both models define utterly the values but from 1050 rpm, the experimental values are higher. As happens with the storage modulus G' , the general model and the significant model have remarkable difference in terms of values and shape.

On the other hand, viscosity (Figure 24 shows the model, while in Figure 25 viscosity in all the range of shear rate is depicted) follows the same behaviour than the yield stress τ_0 experimental results. The value of viscosity slows its growth when the stirring rate N rises. The depiction of the model and the experimental values shows a logarithm curve and from $N = 1050 \text{ rpm}$ a plateau is formed. Along the experimental range, the model fits properly with the model.

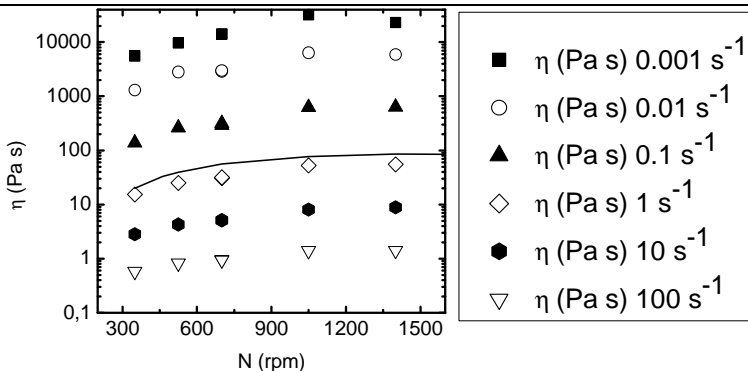


Figure 24. Viscosity at each gradient at equal S/O and Q at medium scale. Models: line.

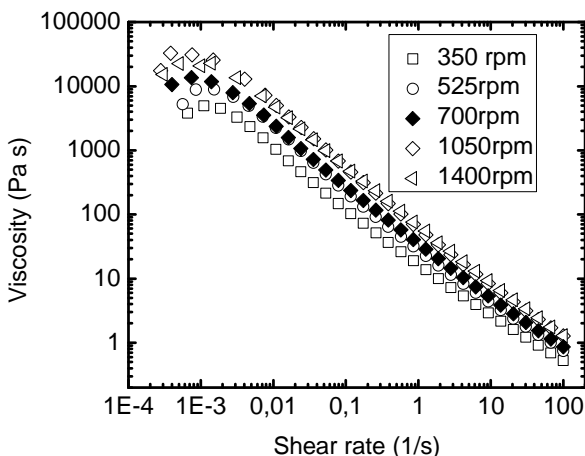


Figure 25. Viscosity versus shear rate test at equal S/O and Q at medium scale at different N . Emulsions prepared at low N have lower viscosity.

Stability analysis

The stability with time decreases sharply below $N = 525$ rpm and above $N = 1050$ rpm (Figure A 32). In the first case, the droplets would be so large that the coalescence is highly favoured. Actually, Figure 26 shows that during the first hours, coalescence is the predominant mechanism (a decrease in BS as a front) but over time, creaming and sedimentation are involved in destabilization. Above $N = 1050$ rpm, the mechanism would be Ostwald ripening due to the presence of tiny droplets (extremely elastic emulsion) which would diffuse to larger drops and accelerate coalescence. Moreover, creaming would have taken part into the destabilization because of the heterogeneous shape of the BS profile 15 days after the preparation of the emulsion (Figure 27).

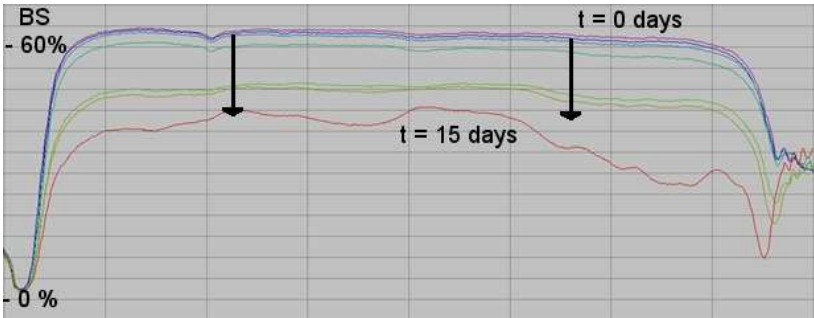


Figure 26. Back Scattering with cell position at each time. $N = 350$ rpm.

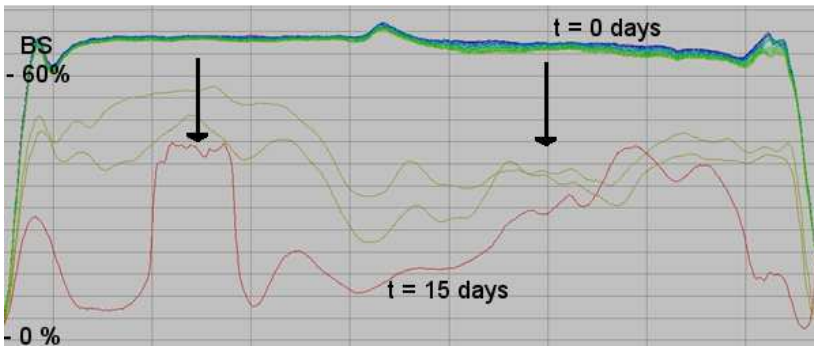


Figure 27. Back Scattering with cell position at each time. $N = 1400$ rpm.

Droplet size and polydispersity

Both mean diameter d_{10} and Sauter mean diameter d_{32} (Figure A 33) decrease with stirring rate N as in the model. Although the behaviour is similar, the Sauter mean diameter predicted by the model is higher than the experimental results. What the model proposes is that at very high N , the Sauter mean diameter d_{32} rises while the models of the rheological parameters predict a more elastic behaviour to the emulsion, so this paradox occurs because the model does not predict properly the value at high N .

The surface area of dispersion a_v (Figure A 34 (A)), which increases with an increase in the stirring rate N (from 1.5 to 3.5 μm^{-1}) because droplets are smaller, indicates that at higher stirring rate N the total surface per unit volume is higher. The coefficient of variation cv (Figure A 34 (B)) is found, as at small scale, around $cv = 0.7$, so all emulsion are polydispersed ($cv > 0.2$).

Summary

An increase of the energy input gives to the emulsion stronger elastic properties. The break of the dispersed phase into tiny droplets is promoted by a higher impeller speed. As several authors said (Malkin et al.²¹, Teipel²², etc), tiny droplets imply a more solid-like behaviour of the emulsion.

4.1.2.3. Influence of addition time at medium scale

The stirring speed N was fixed at $N = 700$ rpm and the surfactant concentration at $S/O = 0.267 \pm 0.020$. Five new experiments were performed varying the addition flow rate values between 31 and 193 mL/min.

Rheological parameters

Although the yield stress τ_0 experimental results follow the general model behaviour (a decrease in the addition flow rate implies an increase in both τ_0 and $(\tau_0)_c$, (Figure A 35), the values are considerably lower than those that the general model predicts. The significant model predicts that τ_0 drops linearly with addition flow rate Q , but apparently, the results follow a negative exponential curve. On the other hand, the behaviour of the critical yield stress $(\tau_0)_c$ (Figure A 36) is described correctly by the significant model (a straight line) rather than a drop which tend to a horizontal asymptote (general model). As happens with τ_0 , the values predicted are much higher than the experimental ones.

The storage modulus G' (Figure A 37) general model does not predict properly neither the behaviour nor the values of the experimental results. While the experimental values decrease slightly when increasing the addition flow rate Q , the model presents a parabolic shape with a minimum. Moreover, the values predicted by the models are fairly higher than the experimental ones. Actually, which predicts properly the behaviour is the significant model (the storage modulus G' drops linearly with the addition flow rate N) but the experimental values are a little lower than the model's ones.

The loss modulus at the critical yield stress G''_{max} (Figure 28), as the storage modulus G' , decreases with the addition flow rate Q . Both models predict the values fairly well but while the significant model describes a decreasing straight line, the general one describes a dropping-curve shape, which also the experimental values follow.

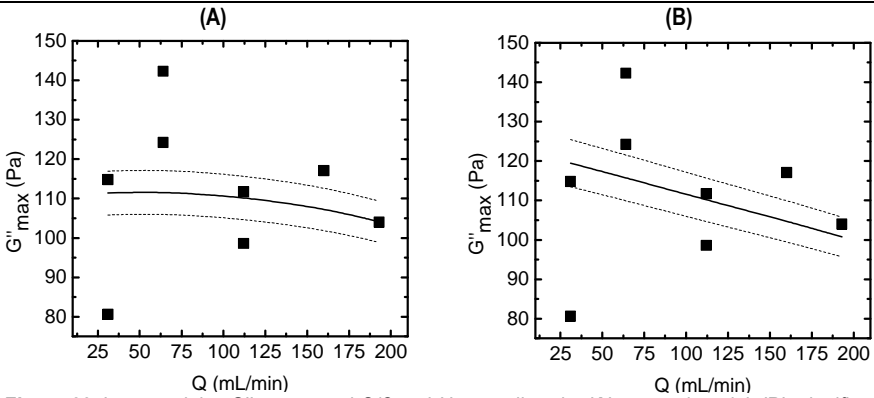


Figure 28. Loss modulus G''_{\max} at equal S/O and N at small scale. (A), general model; (B), significant model.

What the viscosity models (Figure A 38) predict and the experimental values show is the same, the viscosity along the experimental range does not vary significantly. However, at high Q , the viscosity value decreases slightly with the addition flow rate. Therefore, viscosity follows the same behaviour as the other rheological parameters.

Stability analysis

The evolution of the stability with time differs among samples (Figure A 37). Actually, the emulsions prepared at low addition flow rate Q are destabilised quicker than those at high Q as it is presented in Figure 29. The reason might be that at low addition flow rates Q , the droplets are slightly finer than those at high Q , so coalescence might be favoured leading to a quicker destabilisation.

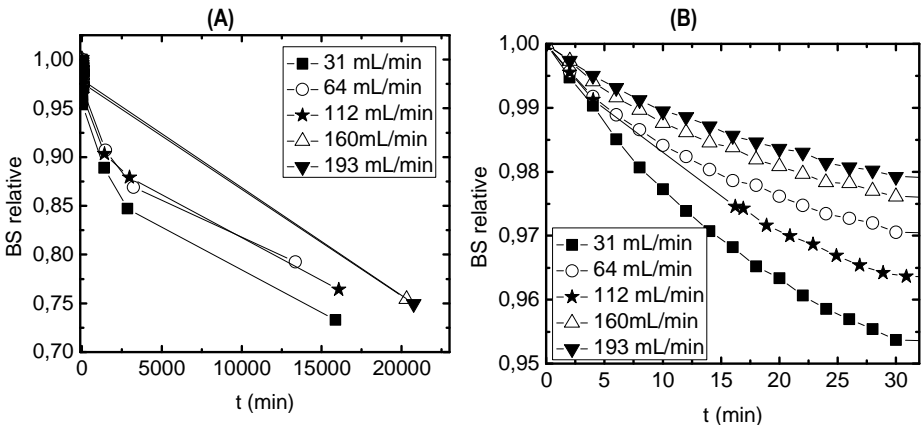


Figure 29. Evolution of relative back scattering with time. (A), the whole interval; (B), only the first 30 min.

Figure A 40 and A 41 show the evolution of BS with time at the cell. The shape in both cases is similar, so it is undeniable that the main mechanism of destabilization is coalescence due to the homogeneous decrease of BS over time.

Droplet size and polydispersity

The Sauter mean diameter d_{32} (Figure A 42 (A)) model predicts a constant value up to $Q = 112$ mL/min and an increase at higher Q . This is the exact behaviour of the experimental values, and as it happens in the previous experiments, the values are considerably lower than the ones that the model predicts. The droplet size d_{10} (Figure A 42 (B)) does not change its value significantly.

The surface area of dispersion a_v (Figure A 43 (A)), as a polydispersity indicator, decreases from $2.2 \mu\text{m}^{-1}$ at $Q = 31$ mL/min to $1.2 \mu\text{m}^{-1}$ at $Q = 193$ mL/min. On the contrary, the coefficient of variation cv (Figure A 43 (B)) is found around 0.9 in all the experimental range, which indicates the polydispersity of the emulsion ($cv > 0.2$)

Summary

The effect of the addition time t (or addition flow rate Q) is not relevant compared with the other factors (surfactant concentration S/O and stirring rate N). What is true is whether the addition time t increases (or the addition flow rate Q decreases), the emulsion possesses more solid-like behaviour, yet the difference between the emulsions prepared in the extreme values of the factor ($Q = 31$ mL/min and $Q = 191$ mL/min) is not so pronounced than the difference between extreme values when the other factors (stirring rate N and addition flow rate Q) are varied to discuss their influence.

4.1.2.4. Influence of S/O rate at medium scale

The stirring rate was set at $N = 700$ rpm and the addition flow rate at $Q = 112$ mL/min. The five experiments were performed varying the surfactant concentration, expressed as a ratio between surfactant and oil S/O , between 0.121 and 0.440.

Rheological parameters

A decrease in the surfactant concentration S/O favours a liquid-like behaviour of the emulsion. It is reflected in the yield stress τ_0 and critical yield stress $(\tau_0)_c$ value: both follow the same behaviour as their respective models but the values do not fit, as happens in most of the experiments. The experimental values of yield stress τ_0 (Figure A 44) follow a behaviour like a growing curve (general model) while the significant model is a increasing straight line since then actor has no effect and there are no quadratic terms. With the critical yield stress $(\tau_0)_c$ (Figure A 45), the contrary occurs, the slope of the significant model is slightly higher than the general one and can describe the behaviour but not the proper value.

The storage modulus G' at $\tau = 1$ Pa models (Figure A 46) predict a sharply growth along the experimental range. The general model follows a slightly exponential curve and the significant one, a straight line. The prediction of the values is not fairly correct in both models.

The loss modulus at the critical yield stress G''_{max} (Figure A 47) follows an almost proportional relation (slightly curved) behaviour with the S/O ratio. Both models (general and significant) are straight lines which predict quite properly the values at low surfactant concentration S/O but at high S/O , the experimental values are so dispersed that they are below and above the models, so conclusions cannot be drawn.

From Figure 30, G''_{max} and $(\tau_0)_c$ are obtained as discussed in the introduction.

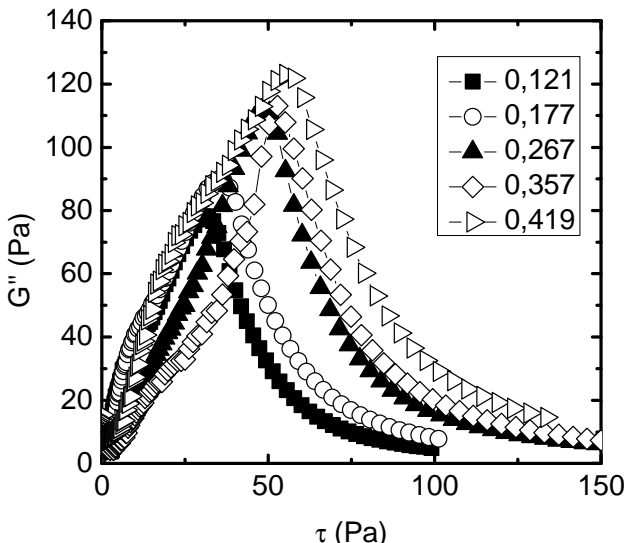


Figure 30. Oscillatory shear test showing the variation of G'' with stress, for different S/O .

Finally, as the other parameters discussed previously, viscosity (Figure A 48) slowed its growth as the surfactant concentration S/O increases. The viscosity model predicts the behaviour of the experimental values but the model values are slightly higher. In fact, when all the experimentation was finished, we noticed that the settings of the viscosity test programme differ from the other ones (steady shear test, oscillatory shear test and frequency sweep test). Moreover, the measurements to obtain the models were developed in a different rheometer, so neither we can check if the settings of viscosity and yield stress test programme of both rheometers are the same nor the calibration at low shear rates is correct.

Stability analysis

The more surfactant there is, the more stable the emulsions are, when observed at a short time after preparation (Figure 31 (A)). In fact, one of the function of the surfactant is to stabilise the droplets against coalescence once they are formed. As Figures A 49 and A 50 show, in the extreme experiments the main destabilization mechanism is coalescence due to the decrease as a front in the BS along time. So, extending the argument to the other experiments, at the fixed stirring rate N and addition flow rate Q , the main mechanism of destabilization is coalescence.

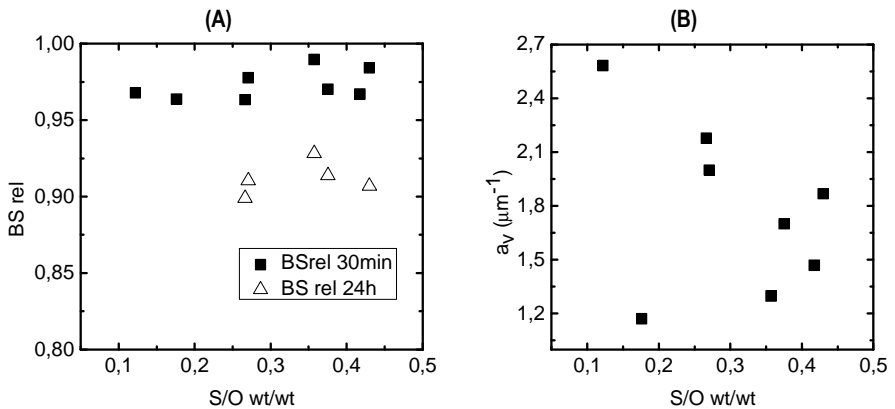
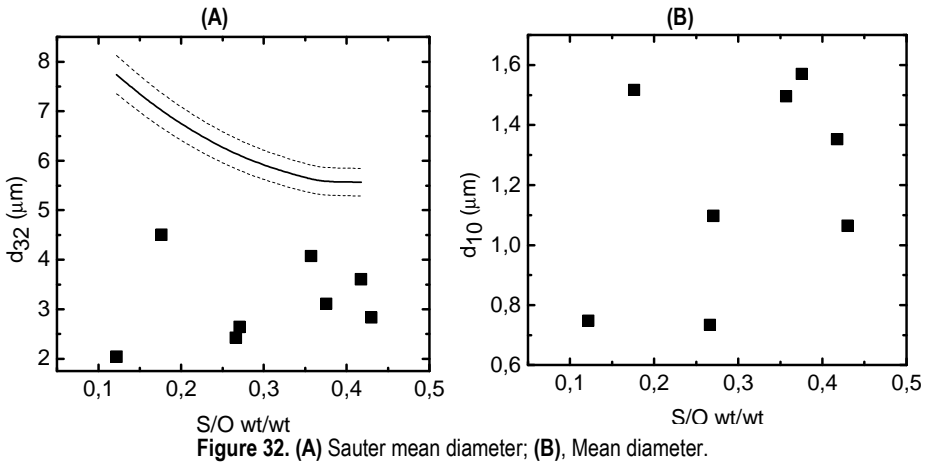


Figure 31. (A) Relative back scattering at 30 min and 24 h.(B), Surface area of dispersion.

Droplet size and polydispersity

The model of the Sauter mean diameter d_{32} (Figure 32 (A)) predicts a decrease with the S/O ratio. The experimental results do not reflect that, firstly, the experimental values are smaller than the model ones and secondly, the experimental values are disparate (vaying from 2 μm to 4.5 μm) but a slightly decreasing behaviour is intuited. The mean diameter d_{10} (Figure 32 (B)) is found in all range around $1.0 \pm 0.5 \mu\text{m}$.

Polydispersity as coefficient of variation cv (Figure A 51) is the same in all the emulsions because all experimental diameters are alike and it is around 0.9, so emulsions are polydispersed. On the other hand, the surface area of dispersion a_v decreases with an increase of the surfactant concentration S/O (from 2.5 to 1.5 μm^{-1}). At small scale, the behaviour of a_v (Figure 31 (B)) (dependant of d_{32} and the dispersed phase volume fraction ϕ –which remains constant) is the inverse (a_v raise with S/O ratio). Due to the disparity and the randomness of d_{32} values, the surface area of dispersion at medium scale is considered not to be significant.



Summary

As it has been discussed, the presence of surfactant favours the elastic behaviour of the emulsions, because it allows the formation of finer droplets (intrinsically related with the rheological behaviour) Yet if stability was a property to take into account, the surfactant concentration would be really close to the optimum value to achieve a more efficient stabilisation over time.

4.2. Validation of the scale-up models

4.2.1. Experiments at large scale

The following scale-up models are obtained from the experimental values at small and medium scale. Some operational problems did not allow preparing emulsions at large scale at first: the impeller blades touched the tank walls during the operation and the impeller, due to its weight, vibrated excessively during the operation at medium stirring rates (400 rpm) making it not really safety, so the range of stirring rates was limited (up to 400 rpm). Finally, we reduced the width of the blades in 2 cm from the original one, and we added an impeller guide to the tank, so a stirring rate N of 1100 rpm could be achieved with the empty stirred tank.

During the experimentation another problem appeared: the stirrer power was not sufficient at stirring rates higher than 700 rpm due to the high viscosity of the emulsion formed. The maximum torque T provided by the stirrer was $90 \text{ N} \cdot \text{cm}$, so when the torque required to stir the emulsion at a fixed rate N was higher than $90 \text{ N} \cdot \text{cm}$, the stirring rate N was reduced automatically, leading to an invalid experiment. Actually, this occurred with only one experiment corresponding to the highest stirring rate N planned: the rheological properties of the emulsion do not follow the behaviour of the other experiments, since the stirring rate is not the proper one and varied through the process.

Figure 33 depicts both torque T provided by the stirrer and stirring rate N of the experiment at the highest N (788 rpm). Around minute 3.75, the torque T reaches a maximum ($90 \text{ N} \cdot \text{cm}$) and immediately after, the stirring rate N decreases sharply. From that point, Torque T remains constant around $80 \text{ N} \cdot \text{cm}$ while the stirring rate N continues to decrease. The amount of emulsion (4 L when the torque T reaches the maximum) and its solid-like properties required a higher power than the one that the stirrer could provide, in order to maintain the energy input planned. Therefore, if new experiments were carried out, a more powerful stirrer would be required so as to obtain a more extended experimental range

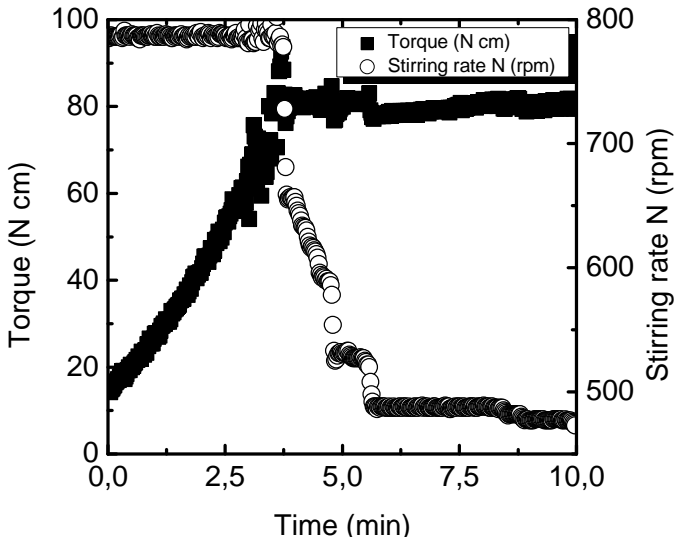


Figure 33. Torque T and stirring rate N during all the experiment $N = 788$ rpm.

The high amount of product required for each experiment does not allow us to complete an experimental design. Therefore, the experiments (Appendices A 1.3.3.) were carried out to validate the scale-up models obtained from the experiments at the other two scales. In fact, this is very interesting, since if we validate the scale-up model obtained with the small and medium scale using the large scale vessel, it would mean that the scale-up model can be applied to other scales other than the ones used to obtain the model.

4.2.2. Validation of the scale-up models

Lineal models at fixed conditions

As discussed previously, the scale-up model followed is ND^α , so the power law exponent α has to be obtained. Due to the apparent linearity of the results, the method used is based on applying a lineal regression between the rheological parameters and ND^α , where α is optimised finding the highest correlation coefficient. The form of the regression is:

$$\text{Parameter} = a + b \cdot ND^\alpha$$

Where ND^α is defined as $ND^\alpha \text{ (cm}^\alpha\text{/s)} = \frac{\pi N \text{ (min}^{-1}\text{)}}{60} D^\alpha \text{ (cm}^\alpha\text{)}$.

Due to equipment limitation, the results at high ND^α (from $N = 1050$ rpm) are really disperse and do not fit conveniently with any linear regression, so this experiments are not included in the range in which the following model would be applied.

In fact, each rheological parameter has a different power law exponent α but this has no sense because emulsions behaviour is defined by all parameters. Therefore, the general power law exponent α defined from the five rheological parameters is found maximising the sum of the correlation coefficients.

The validations of the models were carried out fixing two different surfactant concentration S/O ($S/O = 0.43 \pm 0.02$ and $S/O = 0.267 \pm 0.020$) and two different addition times t ($t = 303$ s [5.08 min] and $t = 1095$ s [18.24 min]) at each scale. The combinations of the levels of the two factors in order to obtain the models are shown in Table 7 .

Table 7. Combination of levels of the factors to validate the models

S/O (wt/wt)	t
0.267 ± 0.020	303 s (5.08 min)
0.43 ± 0.02	303 s (5.08 min)
0.43 ± 0.02	1095 s (18.24 min)

Table 8 shows a summary of the results (the power law exponent α and the coefficient of correlation), the extended ones and some graphs are available on Appendices A 2.1.

Table 8. The power law exponent α and parameter and each combination of levels

S/O (wt/wt) t (s) (t(min))	Storage modulus	Loss modulus	Critical yield stress	Yield stress	Viscosity at $\dot{\gamma} = 1 \text{ s}^{-1}$	d_{32}	Rheological parameters
0.267 ± 0.020 303s(5.08min)	0.67	0.63	0.51	0.43	0.34	0.58	0.53
0.43 ± 0.02 303s(5.08min)	0.62	0.59	0.44	0.51	0.32	-0.55	0.49
0.43 ± 0.02 1095s(18.24min)	0.75	0.61	0.56	0.57	0.62	0.91	0.62

The results in Table 8 show that the power law exponent α of the Sauter mean diameter is only valid in the empirical model at $t = 5.08$ min and $S/O = 0.267$, which is comparable with the other

parameters. In the other two situations, the value is not logic (compared with the other values). As discussed previously, the subjectivity of the measurements (done manually), the random chose of the measurement zone, and the place within the emulsion in which the sample is extracted are determinant factors to consider in order to explain that situation.

The number of values to obtain the lineal models at the conditions $S/O = 0.43 \pm 0.02 / t = 303$ s (5.08 min) and $S/O = 0.43 \pm 0.02 / t = 1095$ s (18.24 min) are limited, 5 and 7 respectively. So, we cannot ensure the validity of the power law exponents α at those conditions. In fact, they would be corroborated by obtaining the global model, discussed in the following section.

Lineal models at fixed conditions from models at each scale

The determination of the power law exponent α from the models was done by the same method as from the experimental values. Some values from each model were obtained fixing a significant number of levels (included inside the experimental range) and then α was optimised maximising the correlation coefficient. The steps followed are discussed in the previous section.

Table 9. Power law exponent α from general models at small and medium scale. The extended ones are presented in Appendices A 2.2.

S/O (wt/wt) t (s) (t(min))	Storage modulus	Loss modulus	Critical yield stress	Yield stress	Viscosity at $\dot{\gamma} = 1 \text{ s}^{-1}$	d_{32}	Rheological parameters
0.267±0.020 303s(5.08min)	0.81	0.90	1.06	0.73	-0.07	0.23	0.71
0.43 ± 0.02 303s(5.08min)	1.05	0.72	0.60	0.52	0.04	-0.18	0.55
0.43 ± 0.02 1095s(18.24min)	1.57	0.80	0.35	0.35	-0.01	0.01	0.57

Comparing the experimental α (Table 8) with those from the models at each scale (Table 9), we observe that only in a few occasions both are similar. Despite this fact, when a power law exponent α is calculated maximizing the sum of the five rheological parameters correlation coefficients, the values are really close, even though these values have a limited validity.

Both (from experiments and models) power law exponent α possess the same behaviour when the values of the factors are changed. Remaining constant the addition time t (addition flow rate

is different at each scale, as discussed previously), whether the surfactant concentration S/O is varied (0.27 to 0.43), the exponent α decreases not fairly in the majority of the rheological values with S/O –and so in the general exponent). On the other hand, at constant surfactant amount S/O , the power law exponent α slightly increases its value (at the current experiments model and at most of the parameters in the regressions from previous work models) when the addition time t is raised.

Therefore, we could conclude that the few experiments developed from the experimental design at the same conditions as the validation experiments, used to obtain the general models are not sufficient to obtain a valid scale up invariant α . Performing more experiments is utterly necessary so as to ensure the validity of the scale-up invariant –what we have done in this work. In fact, the experimental design performed to obtain the empirical models includes only an experiment at $S/O = 0.43 / t = 5.08$ min and none at $S/O = 0.43 / t = 18.24$ min. Moreover, at $S/O = 0.267 / t = 5.08$ min, where three experiments at each scale are performed, only both exponents α (from current work and model) of G' and G'' are slightly coincident, as happens with the values at the validation at each scale.

Specific and global models from all the experiments carried out in the current work

Once these models are obtained and the similarity among power law exponents α at different conditions is corroborated, we decide to find a model which includes the whole experiments carried out in this current work and define the value of any rheological parameter as a function of surfactant concentration S/O , addition time t (min) and ND^α (as a factor which includes the stirring rate N , impeller diameter D –scale- and the power law exponent α). The exponent α will be optimised in order to obtain the maximum correlation coefficient (the procedure is the same as explained previously).

Table 10 shows the specific α for each rheological parameter and a global α which is found from the maximisation of the sum of correlation coefficients for each rheological parameter (as obtained at fixed conditions, Table 8). Appendices N shows the complete models with quadratic interactions.

Table 10. The power law exponent α which define the whole experimental system. The models are available on Appendices A 2.3.

Storage modulus	Loss modulus	Critical yield stress	Yield stress	Viscosity at $\dot{\gamma} = 1 \text{ s}^{-1}$	Rheological parameters
0.73	0.77	0.66	0.49	0.45	0.63

In Appendices A 2.3.3., you can see the depiction of the experimental results compared with the specific models and the global one. As it is logic, the specific model fits more properly with the experimental results, yet the difference with the global model is not fairly significant. This difference is more remarkable at $S/O = 0.267 \pm 0.020 / t = 303 \text{ s}$ (5.08 min) due to larger number of experiments than at the other two conditions, where both models (specific and general) include perfectly (in almost all the parameters) the experimental values. Moreover, the random distribution of the experimental results (under and above the model) shows the significance of the regression –no specific behaviours are followed by any scale–.

In that case, from the Sauter mean diameter d_{32} , no model is obtained due to the disparity of experimental results (shown, for example, in the power law exponents α obtained at a fixed conditions Table 8).

The next step is the confirmation that the scale-up model obtained from the experimental models is valid and includes the values from which the models at each scale were calculated. In order to illustrate properly the possible differences, a response surface graph has been depicted, where the addition time has been fixed and the other two factors (ND^α and S/O) vary along the experimental range. As it can be observed, ND^α includes the scale –as D , impeller diameter–, so that it allows us to depict both scales (small and medium) at the same graph. Figure 34 shows the graphical representation of all the experimental values (both scales) at $t = 8.84 \text{ min}$. Red points are those whose value is lower than the model predicts, and the dark ones, the contrary. That random distribution (under and above the response surface) indicates the validity of the global model. This behaviour is found with the storage modulus G' and loss modulus G'' , but the rest of the rheological parameters, the experimental values remain mainly above the surface.

Obviously, the validity of the models at each scale (where G' and G'' fits the models properly) is intrinsically related with these results.

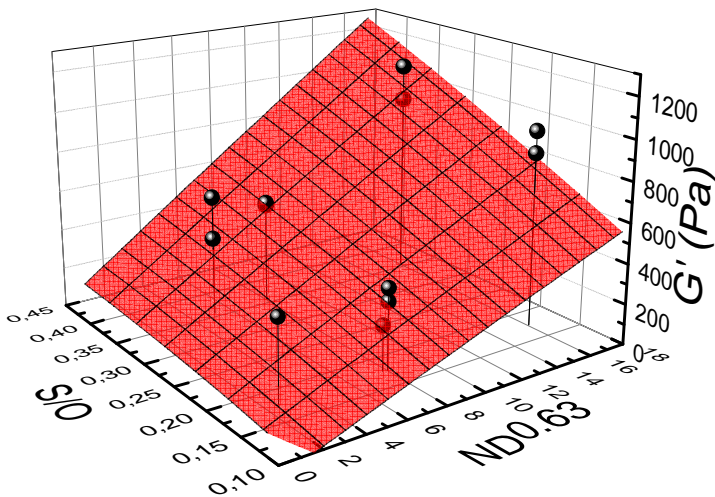


Figure 34. Scale-up general model ($\alpha = 0.63$) and the experimental values from models at each scale were obtained. $t = 8.84$ min.

General models from all the experiments performed in the system (previous and current work)

Confirmed the similarity between the experimental values in the previous work and the model obtained from the experiments carried out in this work, we decided to calculate the quadratic model of each rheological parameter as a function of surfactant concentration S/O , addition time t and ND^α (stirring rate N and scale) –as in all the models calculated–, which include all the experiments developed in the system (previous and current work) following the same procedure as before –maximization of the sum of the correlation coefficients, as discussed previously–. Thus broadening the application range of the model. The power law exponent α ($\alpha = 0.65$) is really close to that obtained only with the current experimental values ($\alpha = 0.63$), that confirms the similarity of behaviour between the values of the current experiments and the values from previous experiments. On the other hand, a random distribution of values of different scales along the experimental range is shown in G' and G'' models, while for the other parameters, due to the difference of the value -not of the behaviour- in some fixed conditions, the experimental values of a scale remain only under or above the model prediction.

Therefore, logically, the current experimental values fit utterly with the global model obtained from them, but the difference between them and the general model from the experimental values of the two works (current and previous) is not significant. This is important because the divergence observed in the small and medium scale validation –due to plausible erroneous calibration of the rheometer and other uncertain errors- is minimised and confirms, as discussed in the previous section, that emulsions in both studies (currently and previously) are the same.

As it is observed in Figure 35 (all the experiments (from current and previous work) depicted with the general model ($\alpha = 0.65$) from all the experiments at $t = 5.08$ min) and in Figure 36 (current experiments presented with the general model ($\alpha = 0.65$) from all the experiments at (A) $t = 18.24$ min / $S/O = 0.43 \pm 0.02$ and (B) $t = 5.08$ min / $S/O = 0.43 \pm 0.02$), the experimental values follow a random distribution (the values are lower and higher than the model's prediction). In Appendices A 2.4., the model's equations are shown and Figure A 58 to 63 confirm the validity of these general models depicting them with the experimental values (of both previous and current work).

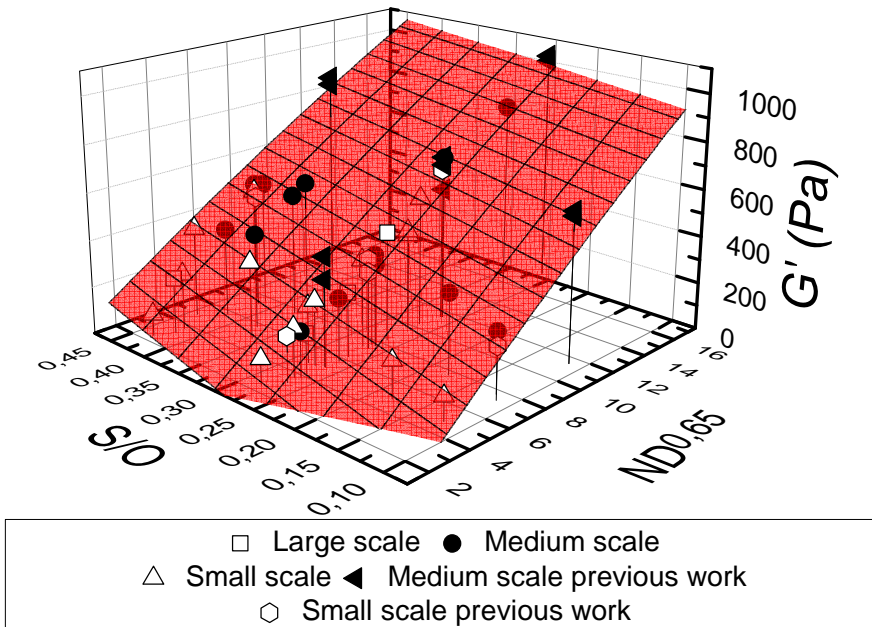


Figure 35. Scale-up general model ($\alpha = 0.65$) and all the experimental values (from current and previous work). $t = 5.08$ min.

(A)

(B)

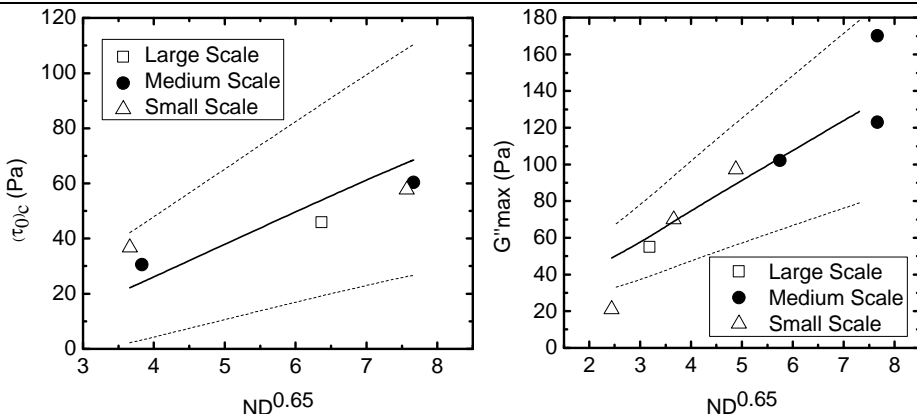


Figure 36. (A) Scale-up general model $(\tau_0)_c$ ($\alpha = 0.65$) and the current experimental values. $t = 18.24$ min / $S/O = 0.43 \pm 0.02$. **(B)**, Scale-up general model G'' ($\alpha = 0.65$) and the current experimental values. $t = 5.08$ min / $S/O = 0.43 \pm 0.02$.

Physical meaning of the power law exponent α

The power law exponent α is really close to $\alpha = 2/3$, which would indicate that emulsions with equal power per unit volume P/V value have the same properties. As discussed in the introduction,

$$\frac{P}{V} = \frac{N_P \rho N^3 D^5}{g_c H T^2 \parallel}$$

Apparently, the value of the exponent $\alpha = 2/3$ is not intuitive but thanks to the geometric similarity between vessels and their geometry, the exponent is exactly $2/3$. For instance, to predict the equivalent stirring rate N_2 at medium scale of the N_1 at small scale,

$$N_2 = N_1 \left(\frac{D_1}{D_2} \right)^{\frac{2}{3}} = N_1 \left(\frac{4.5}{9} \right)^{\frac{2}{3}} = \frac{1}{12} N_1 \quad \text{or}$$

$$N_2 = N_1 \left(\frac{D_1^5 \cdot H_2 \cdot T_2^2}{D_2^5 \cdot H_1 \cdot T_1^2} \right)^{1/3} = N_1 \left(\frac{4.5^5 \cdot 8 \cdot 10^2}{9^5 \cdot 4 \cdot 5^2} \right)^{1/3} = \frac{1}{12} N_1$$

At large scale, in spite of the lower diameter of the impeller ($D_3 = 16$ cm), the power law exponent α to relate it with the other scales, is not exactly $\alpha = 2/3$ but it's really close.

Okufi et al³⁴ studied P/V as an scale invariant at liquid – liquid dispersions, but they concluded that the equal tip speed was a better scale-up criterion. Bourne and Yu³⁵ assumed P/V as a scale

invariant in their study of macromixing at stirred tanks. Despite this fact, several authors (Wilkins and Gates²⁶, Paul Chen et al³⁶, etc) recommend P/V to perform the scale-up of mixing processes. In this study, the emulsion volume V increases over time until all the dispersed phase is added. On the other hand, as torque T profiles provided by LabWorldSoft® along all the process duration show, torque T increases its value while water is being added, logically, the more fluid there is, the more energy input the stirrer has to provide in order to maintain the fixed stirring rate. As it is observed in Figure 37, the graphical representation of the power per unit volume P/V ($P = TN 2\pi / 60$) versus emulsification time, P/V is not constant over time and, hence, the interpretation of this physical meaning is not obvious and would constitute a more extended work. Moreover, as P and V vary during all the emulsification time, we cannot fix P/V as a scale invariant from the beginning.

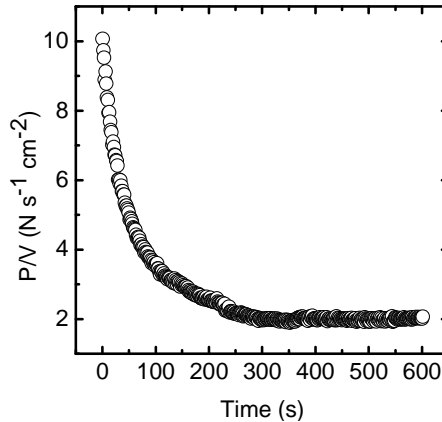


Figure 37. Evolution of P/V at $S/O = 0.267$, $N = 700$ rpm and $t = 5.08$ min at medium scale over time

Another important result is that there is not an appreciable difference between stability over time (30 min and 24 h after preparation) comparing the three scales results. Apparently, in the large scale more instable emulsions would be formed because of the plausible presence of non-agitated zones (due to the higher distance between blades which would favour coalescence between droplets). However, by representing the *relative BS* at all the three scales (Figure 38), we can see that the values agree with the values agree with the model at $ND^{0.65}$, so the emulsions formed are the same at all three scales and have the same stability.

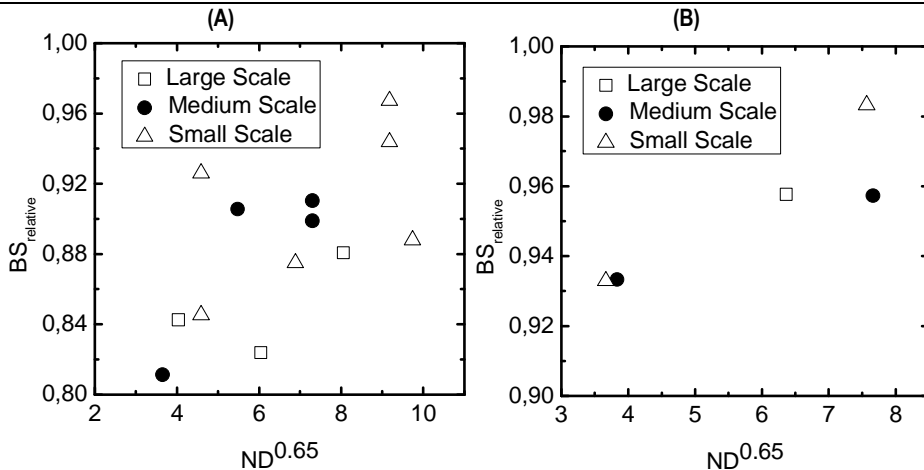


Figure 38. (A) Relative BS 24 h after the emulsion preparation at $S/O = 0.267 / t = 5.08$ min. (B) Relative BS 30 min after the emulsion preparation at $S/O = 0.43 / t = 18.24$ min.

Figure 39 is presented in order to visualise the destabilization process, where the separation of phases is clearly observed (creaming). What is true is that the majority of the emulsions remain, to the naked eye, completely stable (as the first sample) two months after the preparation.

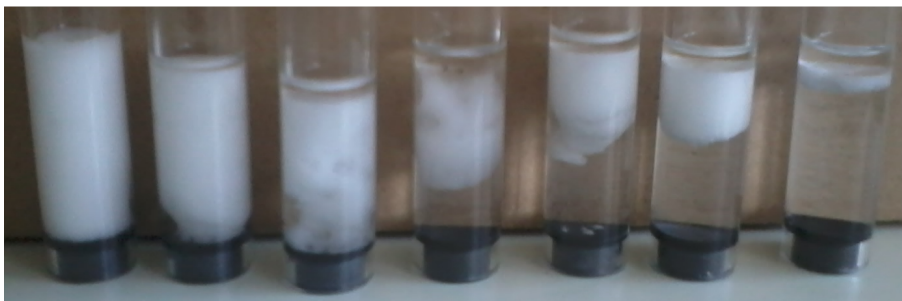


Figure 39. Progressive destabilization of the emulsion at cylindrical glass measurement cell. Samples from different-scale emulsions.

4.3. Preparation of meso- and macroporous materials

One of the application of HIPREs is the preparation of meso- and macroporous materials (Vilchez et al³⁷, Santamaría et al³⁸, Esquena et al³⁹, Vilchez et al⁴⁰). According to IUPAC⁴¹, materials are considered as microporous when their pore sizes are less than 2 nm; mesoporous, 2-50 nm; and macroporous, bigger than 50 nm.

HIPREs allow us to obtain particles with a combination of different pore sizes. The drops in the dispersed phase act as templates for macropores and structures afforded by surfactant molecules act as templates for mesopores.

The preparation of silica particles with meso- and macropores from the prepared emulsions is simple. In our case, a slightly amount of ammonium buffer solution was added to a portion of emulsion prepared to raise the pH, and then, tetraethyl orthosilicate (TEOS) –which generate silica from its hydrolysis- was added. The emulsion remained about 12 hours at 40 °C at a stirring rate of 500 rpm. As we are working with inverse emulsions (W/O emulsions), the TEOS is solubilised in the continuous phase and then reacts with the water on the interface, producing hollow particles or a thin film material. In our case, the process is not yet optimised, but some first essays confirmed the synthesis of silica materials with meso and macropores.

The sample was analysed by Transmission and Scanning Electron Microscopy (TEM and SEM) and some representative images are shown in the following photographs:

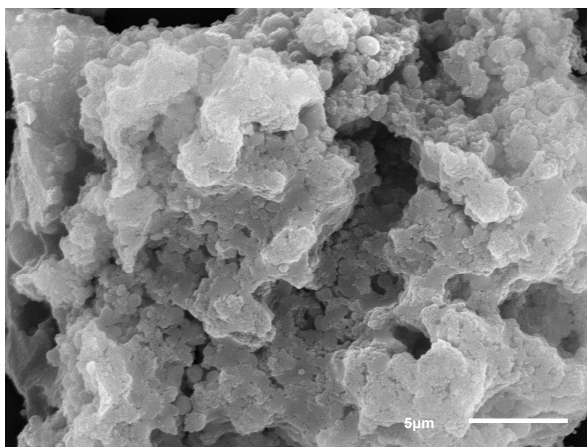


Figure 40. SEM micrograph of the sample at 4300x

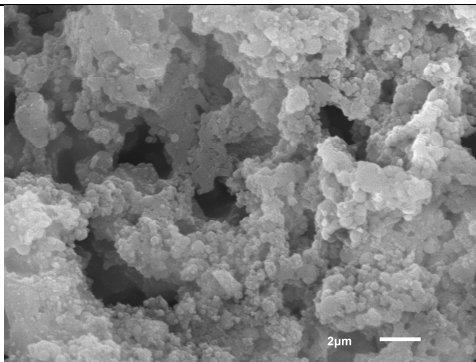


Figure 41. SEM micrograph of the sample at SEM at 5500x

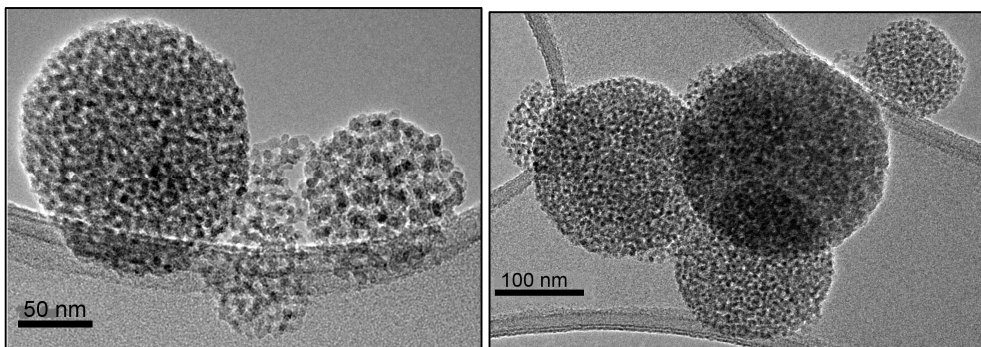


Figure 42. TEM micrographs of the sample at TEM at 60000x and 40000x, respectively.

In Figure 40 and 41, the macropores can be clearly seen as the interstices among joint particles and in Figure 42, mesopores are intuited by the different dark tones showed in the rough surface of the particles. The mesopore size distribution of the sample was analysed by the BJH method⁴² from data obtained in the adsorption-desorption of nitrogen (at 77 K). The pores were around 5 nm. On the other hand, macropores size was not determined, but will be determined in a further study by mercury porosimetry⁴³. The surface area was determined by the BET method from the adsorption-desorption isotherm, and a value of 525 m²/g was obtained.

Materials with dual meso- and macropores combine the advantages of high specific areas with good diffusion properties associated with macropores. Due to this excellent properties as Esquena et al³⁹ affirm, meso/macroporous materials are being widely used in a lot of industrial applications, such as in chromatographic adsorbents separation processes, photocatalysis, fuel cells, energy storage or heterogeneous catalysis for biodiesel production.

5. Conclusions

As the validation results at small and medium scale show, the majority of models describing the effect of the process variables to the rheological parameters are not validated. The storage and loss modulus (G' and G'') are those which are more properly predicted. On the other hand, the critical yield stress $(\tau_0)_c$ models are valid in some ranges of the experimental range and the yield stress τ_0 model describes the same behaviour as the results, but these values are lower. Focusing on viscosity, in all the experiments the value of the model is slightly higher than the experimental one.

It is unhesitating that the solid-like behaviour is related with the emulsion structure as several authors (Malkin et al.²¹, Teipel²², etc) exposed, therefore, the behaviour of the values of the droplet size at each experiments is correct. However, the diameter values differ excessively from the models. The measurement of the droplet size is done manually and is completely subjective. The random choice of the zone of measurement, the place within the emulsion which it is extracted, the background of the experimenter, etc can be determinant factors that can distort the final value. Therefore, the rheological parameters to characterise the emulsions are a more valid method instead of droplet size, owing to the minimization of the human interactions in the measurement.

What is clear is that some parameters are coincident; the emulsions prepared at both works (previous and current) are similar. Although, the values predicted by the models and the experimental results slightly differ, their behaviours are clearly similar, so the systematic and uncontrolled errors seem to be the cause of distortion of our measurements. Therefore, the non-coincidence between models and experimental values in viscosity and yield stress can be caused by an erroneous calibration of the rheometer (as discussed in the results section). Another plausible source of error could be the surfactant used; despite being the same, as it is not a pure component with a defined chain-length, its properties can change from batch to batch.

Moreover, the extension of the models at low stirring rates N succeed in most of the rheological parameters at both scales (especially for the loss modulus G''_{max}). When both values do not fit, the predicted value is higher than the experimental one.

The effect of the factors in the rheological behaviour of the emulsions is uneven. The most influential factor is the stirring rate. The impeller is the “droplets’ breaker”, so the quicker it spins, the more elastic the emulsions are. The surfactant concentration, as a surfactant-to-oil (dodecane) ratio S/O , has a secondary but important effect. The more surfactant there is, the interfacial tension is reduced and more surfactant monomers are available to stabilise the water-in-oil interface, leading to the formation of finer droplets, which, packed together due to the high volume fraction of dispersed phase, involves the formation of a more elastic emulsion, yet an optimum surfactant concentration, which stabilise more efficiently the emulsion over time, exists. Finally, the influence of addition flow rate Q (or addition time t) is not as significant as the other factors. Although it is unhesitating that there are differences between the experiments performed at the extreme values of the range, they are not so pronounced as in the other factors. Therefore, not only we can affirm that the emulsion behaviour is slightly influenced by the addition flow rate Q , but the stirring rate is the veritable factor that influences the most in the emulsion preparation.

The back scattering profiles confirms that the predominant destabilisation mechanism is, without any doubt, coalescence, which is followed (mainly in some extreme levels) by sedimentation or creaming.

Monodisperse emulsion, as the results show, cannot be achieved, so all the emulsions are polydisperse as the coefficient of variation cv at all the experiments and the captures of the droplets at the microscope, presented in Appendices A 2.5, show. Yet images of the majority of the emulsions at the microscope present a visible homogeneity in size, which would suggest that the polydispersity is not as sharp as the coefficient of variation cv predicts. As discussed in the validation of the models at each scale, the Sauter mean diameter d_{32} is considerably lower than the prediction of the model (previous work), so the inverse proportionality of cv to d_{32} (the standard deviation s is similar in both works) might cause these higher polydispersity values, which is

apparently not observed in the microscope images. This is another evidence of the subjectivity of the droplet size measurement.

In the scale-up process, due to its complexity, we followed a prudent method; firstly, the lineal regressions of some experiments with the same surfactant concentration and addition time were performed in order to obtain an optimum power law exponent α . The scale invariants α of the three fixed conditions do not differ too much. So, the next step was the multiple regressions –with quadratic terms- of all the current experimental values maximising the sum of regression coefficient of all the rheological parameters—as previously- to obtain the scale invariant α which defines more properly the behaviour of all the parameter in the experimental system. And the final step was putting together the current and previous experiments (from which models at each scale were obtained) to obtain a more significant model of the system also because the application range is broadened. The difference between both quadratic models, generally, is not so remarkable. The power law exponent α obtained by regression is $\alpha = 0.63$ from current experiments and $\alpha = 0.65$ from all the experiments (current and previous work).

On the other hand, the difference between values of some rheological parameters in the previous and current work distorts slightly the regressions because a lack of a random distribution of the scales (some values at the same scale remain only under or above the global model) is confirmed (mainly, in viscosity and yield stress). Yet that do not happen with the model from current experiments because the settings of the devices have not been changed, so values are more coincident.

When we obtain the power law exponent α from the models at each scale, we observe the disparity of values, which do not fit with the power law exponent α from the current experiments. Therefore, the models obtained in previous works define properly the behaviour of the rheological parameters at each scale but they are not valid to predict a reliable scale-up invariant, owing to the few number of experiments performed at the same conditions.

The power law exponent α possesses a physical meaning, In fact, it is really close to $\alpha = 2/3$, which would indicate that power per unit volume P/V is the scale invariant, one of the most recommended parameters in the scale-up of mixing processes. Yet in this experimental system, the P/V is not constant along the emulsification process, so there is no immediate and obvious explanation. That would require a broader discussion, which we leave for a further and more extended work.

Moreover, the emulsions with equal scale-up invariant number $ND^{0.65}$ (as we consider, emulsions have the same properties) do not present significant variation of stability over time (30 min and 24 h after the emulsion preparation). This indicates that when increasing the production, there is no difference in properties and in stability, also important, among emulsions at the three scales.

What is really unique of this work is that the global model allows us to predict the values of the preparation and composition variables at each scale in order to obtain the same emulsion at the three scales. As far as we know, no other study has obtained a scale invariant factor for the preparation of highly-concentrated emulsions prepared at three different scales, which covers all three scales, different addition times, stirring rates and surfactant concentrations, so this is an excellent result and a very remarkable conclusion.

6. References

1. Pal, R. Yield stress and viscoelastic properties of high internal phase ratio emulsions. *Colloid Polym. Sci.* **277**, 583–588 (1999).
2. Babak, V. G. & Stébé, M.-J. Highly Concentrated Emulsions: Physicochemical Principles of Formulation. *J. Dispers. Sci. Technol.* **23**, 1–22 (2002).
3. Fernandez, P., André, V., Rieger, J. & Kühnle, A. Nano-emulsion formation by emulsion phase inversion. *Colloids Surfaces A Physicochem. Eng. Asp.* **251**, 53–58 (2004).
4. IKA. Colloid Mill MK. at <<http://www.ikaprocess.com/Products/Inline-disperser-dispersing-machine-high-shear-cph-6/Colloid-Mill-MK-csb-MK/>>
5. France, J. M. *et al.* On Slip Effects in Steady-state Flow Measurements Oil-in-Water Food Emulsions. **8774**, (1998).
6. Aranberri, I., Binks, B. P., Clint, J. H. & Group, C. ELABORACION Y CARACTERIZACIÓN DE EMULSIONES. **7**, 211–231 (2006).
7. Capdevila, M., Maestro, A., Porras, M. & Gutiérrez, J. M. Preparation of Span 80/oil/water highly concentrated emulsions: influence of composition and formation variables and scale-up. *J. Colloid Interface Sci.* **345**, 27–33 (2010).
8. Esquena, J., Sankar, G. S. R. R. & Solans, C. Highly Concentrated W / O Emulsions Prepared by the PIT Method as Templates for Solid Foams. 2983–2988 (2003).
9. Sadtler, V. *et al.* Low Energy Emulsification Methods for Nanoparticles Synthesis. (2008).
10. Esquena, J., Sankar, G. S. R. R. & Solans, C. Highly Concentrated W / O Emulsions Prepared by the PIT Method as Templates for Solid Foams. 2983–2988 (2003).
11. Whittingstall, P. Overview of Viscosity and Its Characterization. *Curr. Protoc. Food Anal. Chem.* **H1.1.1.-H1**, 1–6 (2001).
12. Bhattacharya, S., Bal, S., Mukherjee, R. K. & Bhattacharya, S. Kernel Powder (TKP) Suspension. **13**, (1991).
13. Bhattacharya, S. & Bhat, K. K. Steady shear rheology of rice-blackgram suspensions and suitability of rheological models. *J. Food Eng.* **32**, 241–250 (1997).
14. Jager-Lézer, N. *et al.* Rheological analysis of highly concentrated W/O emulsions. **138**, 129–138 (1998).

15. Mason, T. *et al.* Osmotic pressure and viscoelastic shear moduli of concentrated emulsions. *Phys. Rev. E* **56**, 3150–3166 (1997).
16. Kulicke, W.-M., Arendt, O. & Berger, M. Characterization of hydroxypropylmethyl- cellulose-stabilized emulsions. *Colloid Polym. Sci.* **276**, 1024–1031 (1998).
17. Yang, X. H. & Zhu, W. L. Viscosity properties of sodium carboxymethylcellulose solutions. *Cellulose* **14**, 409–417 (2007).
18. Mason, T. G. & Bibette, J. Shear Rupturing of Droplets in Complex Fluids. *Langmuir* **13**, 4600–4613 (1997).
19. Particle Science. Drug Development Services. Emulsion Stability and Testing. *Tech. Br.* **2**, (2011).
20. Bru, P. *et al.* Particle Size and Rapid Stability Analyses of Concentrated Dispersions Use of Multiple Light Scattering Technique. *Recherche* **881**, 1–15 (2004).
21. Malkin, A. Y., Masalova, I., Slatter, P. & Wilson, K. Effect of droplet size on the rheological properties of highly-concentrated w/o emulsions. *Rheol. Acta* **43**, 584–591 (2004).
22. Teipel, B. U. Influence of Droplet Size on the Rheological Behavior of Emulsions. **73**, 609–615 (2002).
23. Paruta-Tuarez, E., Marchal, P., Sadtler, V. & Choplin, L. Analysis of the Princen and Kiss Equation To Model the Storage Modulus of Highly Concentrated Emulsions. *Ind. Eng. Chem. Res.* **50**, 10359–10365 (2011).
24. Zauner, R. & Jones, A. G. Scale-up of Continuous and Semibatch Precipitation Processes. *Ind. Eng. Chem. Res.* **39**, 2392–2403 (2000).
25. Gorsky, I. in *Pharm. Process Scale-Up* (Levine, M.) 43–56 (Marcel Dekker, Inc, 2001).
26. Wilkens, R. J. & Gates, L. E. How to Scale-Up Mixing Processes in Non-Newtonian Fluids. *Solids/Liquids Handl.* 44–52 (2003).
27. NIST. SEMATECH e-Handbook of Statistical Methods. at <<http://www.itl.nist.gov/div898/handbook/>>
28. L. Eriksson, E. Johansson, N. Kettaneh-Wold, C. Wilström, S. W. *Design of Experiments. Principles and Applications.* (Umetrics AB).
29. Sigma-Aldrich. Span 80 for GC. at <<http://www.sigmaaldrich.com/catalog/product/fluka/09569?lang=es®ion=ES>>

30. CERE. Emulsion Stability by Turbiscan. at [http://www.cere.dtu.dk/Expertise/Laboratories/Emulsion Stability by Turbiscan.aspx](http://www.cere.dtu.dk/Expertise/Laboratories/Emulsion%20Stability%20by%20Turbiscan.aspx)
31. Schramm, L. *Surfactants: fundamentals and applications in the petroleum industry*. (2000). at <http://catdir.loc.gov/catdir/samples/cam032/99015820.pdf>
32. Pugh, R. Foaming, foam films, antifoaming and defoaming. *Adv. Colloid Interface Sci.* **64**, 67–142 (1996).
33. Pichot, R. Stability and Characterisation of Emulsions in the presence of Colloidal Particles and Surfactants. (2010).
34. Okufi, S., De Ortiz, E. S. P. & Sawistowski, H. Scale-up of liquid-liquid dispersions in stirred tanks. *Can. J. Chem. Eng.* **68**, 400–406 (1990).
35. Bourne, J. R. & Yu, S. Investigation of micromixing in stirred tank reactors using parallel reactions. *Ind. Eng. Chem. Res.* **33**, 41–55 (1994).
36. Chen, J. P., Higgins, F. B. & Chang, S. *Mixing*. **3**,
37. Vilchez, S., Pérez-Carrillo, L. a, Miras, J., Solans, C. & Esquena, J. Oil-in-alcohol highly concentrated emulsions as templates for the preparation of macroporous materials. *Langmuir* **28**, 7614–21 (2012).
38. Santamaría, E. *et al.* Micro-, Meso-, and Macroporous Materials Obtained from a Highly Concentrated Emulsion of Decane/Brij 35/Water and Decane/Brij 700/Water. *Chem. Lett.* **41**, 1041–1043 (2012).
39. Esquena, J., Nestor, J., Vilchez, A., Aramaki, K. & Solans, C. Preparation of mesoporous/macroporous materials in highly concentrated emulsions based on cubic phases by a single-step method. *Langmuir* **28**, 12334–40 (2012).
40. Vilchez, A., Rodríguez-Abreu, C., Esquena, J., Menner, A. & Bismarck, A. Macroporous polymers obtained in highly concentrated emulsions stabilized solely with magnetic nanoparticles. *Langmuir* **27**, 13342–52 (2011).
41. Soler-Illia, G. J. de A. A., Sanchez, C., Lebeau, B. & Patarin, J. Chemical Strategies To Design Textured Materials: from Microporous and Mesoporous Oxides to Nanonetworks and Hierarchical Structures. *Chem. Rev.* **102**, 4093–4138 (2002).
42. Barrett, E. P., Joyner, L. G. & Halenda, P. P. The determination of pore volume and area distributions in porous substances. I. Computations from nitrogen isotherms. *J. Am. Chem. Soc.* **73**, 373–380 (1951).
43. Giesche, H. Mercury Porosimetry: A General (Practical) Overview. *Part. Part. Syst. Charact.* **23**, 9–19 (2006).

7. Abbreviations and nomenclature

Abbreviations

<i>CCD</i>	Central composite design
<i>CS mode</i>	A controlled stress input τ is provided and the resulting shear rate $\dot{\gamma}$ is determined
<i>CR mode</i>	A controlled shear rate $\dot{\gamma}$ is provided and the resulting stress input τ is determined
<i>DOE</i>	Design of experiments
<i>EIP</i>	Emulsion inversion point
<i>HIPRE</i>	High-internal-phase-ratio emulsions
<i>HLB</i>	Hydrophile-lipophile balance
<i>O/W</i>	Oil in water
<i>PIT</i>	Phase inversion temperature
<i>rpm</i>	Revolutions per minute
<i>RSM</i>	Response surface method
<i>SEM</i>	Scanning Electron Microscopy
<i>TEM</i>	Transmission Electron Microscopy
<i>TEOS</i>	Tetraethyl orthosilicate
<i>W/O</i>	Water in oil

Nomenclature

α	Power law exponent of the scale invariant (-)
a_d	Area of dispersed phase (μm^2)
a_v	Surface area of dispersion (μm^{-1})
<i>BS</i>	Back scattering (%)
BS_{rel}	Relative back scattering (%)
cv	Coefficient of variation (μm^{-1})
D	Impeller blade diameter (cm)
d_{10}	Mean diameter (μm)
d_{32}	Sauter mean diameter or surface-volume mean diameter (μm)
d_i	Droplet diameter (μm)
Fr	Froude number (-)
$\dot{\gamma}$	Shear rate (s^{-1})
ϕ	Dispersed phase volume fraction (-)
g	Standard gravity (m/s^2)

g_c	Gravitational conversion factor
G	Static shear modulus (Pa)
G^*	Complex shear modulus (Pa)
G'	Storage modulus (Pa)
G''	Loss modulus (Pa)
G''_{max}	Loss modulus at the critical yield stress $(\tau_0)_c$ (Pa)
H	Height of the liquid in the vessel (cm)
λ	Wave length (nm)
μ	Newtonian viscosity (Pa s)
η	Non-Newtonian viscosity (Pa s)
η_0	Zero-shear viscosity (Pa s)
η_∞	Infinite-shear viscosity (Pa s)
N	Stirring rate (rpm or min ⁻¹)
$N D^a$	Scale invariant from Gorsky approach (m ^a /min)
n_i	Number of droplets
N_p	Power number (-)
P	Power (W)
P/V	Power per unit volume (W/m ³)
Q	Addition flow rate (mL/min)
ρ	Density of solution dispersion (kg/m ³)
R_{32}	Sauter mean radius (μm)
Re	Reynolds number (-)
σ	Interfacial tension (N/m)
S/O	Surfactant concentration as a surfactant-to-oil ratio (wt/wt)
s	Standard deviation (-)
S_t	Impeller tip speed (rad/s)
τ	Shear stress (Pa)
τ_0	Yield stress (Pa)
$(\tau_0)_c$	Critical yield stress (Pa)
T	Torque (N m)
T/V	Torque per unit volume ((N·m)/m ³)
t	Addition time (s or min)
T	Vessel diameter (cm)
T_{HLB}	Hydrophile-lipophile balance (HLB) temperature
V_t	Volume of the whole dispersion (mL)
V_d	Volume of the dispersed phase (mL)
ω	Frequency (s ⁻¹)

APPENDICES

A 1.Validation of the models at each scale

A 1.1. Models at small scale

Storage module		Loss modulus		Yield stress	
Significant factors	R ² =0.895	Significant factors	R ² =0.956	Significant factors	R ² =0.968
<i>cnt</i>	-293.91	<i>cnt</i>	-54.4604	<i>cnt</i>	-15.9537
SO	1120.1	SO	188.201	SO	86.7395
<i>N</i>	0.357357	<i>Q</i>	-0.901303	<i>Q</i>	-0.752919
		<i>N</i>	0.102584	<i>N</i>	0.0422001
All factors	R ² =0.968	All factors	R ² =0.982	All factors	R ² =0.981
<i>cnt</i>	564.685	<i>cnt</i>	84.4835	<i>cnt</i>	-24.6676
SO	-503.631	SO	-113.967	SO	160.891
<i>Q</i>	-31.8898	<i>Q</i>	-7.36936	<i>Q</i>	-1.60802
<i>N</i>	-0.446682	<i>N</i>	-0.0198661	<i>N</i>	0.0565369
SO·SO	295.692	SO·SO	455.441	SO·SO	-175.1
SO· <i>Q</i>	48.3333	SO· <i>Q</i>	4.30093	SO· <i>Q</i>	1.41204
SO· <i>N</i>	0.751587	SO· <i>N</i>	-0.00119048	SO· <i>N</i>	-0.000396825
<i>Q</i> · <i>Q</i>	0.187326	<i>Q</i> · <i>Q</i>	0.105749	<i>Q</i> · <i>Q</i>	-0.00993451
<i>Q</i> · <i>N</i>	0.00929762	<i>Q</i> · <i>N</i>	0.00224643	<i>Q</i> · <i>N</i>	0.000720238
<i>N</i> · <i>N</i>	0.000225332	<i>N</i> · <i>N</i>	0.0000434848	<i>N</i> · <i>N</i>	-0.0000115782

Loss modulus		Viscosity at $\dot{\gamma} = 1 \text{ s}^{-1}$		Droplet size d_{32}	
Significant factors	R ² =0.864	Significant factors	R ² =0.968	Significant factors	R ² =0.870
<i>cnt</i>	-45.5106	<i>cnt</i>	16.7469	<i>cnt</i>	33.4817
SO	151.099	SO	99.9419	SO	-52.5678
<i>N</i>	0.0627515	<i>Q</i>	-2.44871	<i>N</i>	-0.0289828
		<i>N</i>	0.0121315	SO· <i>N</i>	0.036746
		<i>Q</i> · <i>N</i>	0.00183333	<i>N</i> · <i>N</i>	0.00000567314

All factors	R ² =0.945	All factors	R ² =0.981	All factors	R ² =0.953
<i>cnt</i>	116.38	<i>cnt</i>	10.0834	<i>cnt</i>	28.0317
SO	-179.997	SO	151.163	SO	-45.5111
Q	-7.47687	Q	-2.00992	Q	0.376127
N	-0.0744452	N	0.0510368	N	-0.027895
SO·SO	460.871	SO·SO	-115.859	SO·SO	14.9444
SO·Q	2.27315	SO·Q	1.2963	SO·Q	-1.07407
SO·N	0.0506349	SO·N	-0.00714286	SO·N	0.036746
Q·Q	0.146724	Q·Q	-0.0280323	Q·Q	0.0102862
Q·N	0.001825	Q·N	0.00183333	Q·N	-0.000255952
N·N	0.0000467272	N·N	-0.0000176182	N·N	0.00000686148

A 1.2. Models at medium scale

Storage module		Loss modulus		Yield stress	
Significant factors	R ² =0.871	Significant factors	R ² =0.928	Significant factors	R ² =0.814
<i>cnt</i>	-450.164	<i>cnt</i>	-82.3682	<i>cnt</i>	-21.6703
SO	2323.35	SO	137.98	SO	45.6014
Q	-0.85115	Q	-0.114307	Q	-0.0642641
N	1.00667	N	0.295287	N	0.118595
SO·N	-1,5903	N·N	-0.0000778645	N·N	-0.000033338
All factors	R ² =0.897	All factors	R ² =0.939	All factors	R ² =0.831
<i>cnt</i>	-680.474	<i>cnt</i>	-174.689	<i>cnt</i>	-20.6458
SO	1607.49	SO	355.475	SO	111.876
Q	1.56539	Q	0.407566	Q	-0.12889
N	1.32794	N	0.360909	N	0.113074
SO·SO	2132.15	SO·SO	71.1692	SO·SO	-184.722
SO·Q	-3.75518	SO·Q	-0.827748	SO·Q	0.172652
SO·N	-1.58682	SO·N	-0.154957	SO·N	0.0122336
Q·Q	0.00484023	Q·Q	-0.000397309	Q·Q	-0.000652809
Q·N	-0.00238095	Q·N	-0.000202009	Q·N	0.000156994
N·N	-0.0000260001	N·N	-0.0000786595	N·N	-0.0000406345

Critical yield stress		Viscosity at $\dot{\gamma} = 1 \text{ s}^{-1}$		Droplet size d_{32}	
Significant factors	$R^2 = 0.918$	Significant factors	$R^2 = 0.876$	Significant factors	$R^2 = 0.853$
<i>cnt</i>	-51,9604	<i>cnt</i>	-43.5255	<i>cnt</i>	17.5157
SO	94,9204	SO	95.1645	SO	-4.23008
Q	-0,0700075	Q	-0.0522684	N	-0.0191686
N	0,193633	N	0.143311	N·N	0.0000699652
N·N	-0,0000556089	N·N	-0.0000473812		
All factors	$R^2 = 0.933$	All factors	$R^2 = 0.886$	All factors	$R^2 = 0.892$
<i>cnt</i>	-84,3104	<i>cnt</i>	-66.3167	<i>cnt</i>	20.9231
SO	182,305	SO	153.777	SO	-22.8561
Q	-0,0703627	Q	0.182687	Q	0.00789889
N	0,23	N	0.152788	N	-0.0228599
SO·SO	45,0939	SO·SO	-176.092	SO·SO	28.0957
SO·Q	0,0736253	SO·Q	-0.11467	SO·Q	-0.0558241
SO·N	-0,113963	SO·N	0.0457972	SO·N	0.00943173
Q·Q	0,000475447	Q·Q	-0.000610621	Q·Q	0.0000783906
Q·N	-0,000119792	Q·N	-0.0000643973	Q·N	-0.00000811012
N·N	-0,0000520639	N·N	-0.0000542717	N·N	0.00000798984

A 1.3. Experiments performed

A 1.3.1. Small scale

Exp	S/O (wt/wt)	Q (mL/min)	N (rpm)
1	0.267	14.0	525
2	0.267	14.0	1050
3	0.267	14.0	700
4	0.267	14.0	1400
5	0.267	3.9	700
6	0.267	14.0	350
7	0.267	24.1	700
8	0.177	14.0	700
9	0.121	14.0	700
10	0.44	14.0	700
11	0.357	14.0	700
12	0.267	8.0	700
13	0.267	20.0	700
14	0.267	14.0	1400
15	0.267	14.0	700
16	0.267	8.0	700
17	0.267	14.0	1485
18	0.42	14.0	350
19	0.42	14.0	1050
20	0.42	14.0	525
21	0.42	3.9	525
22	0.42	3.9	1085

A 1.3.2. Medium scale

Exp	S/O (wt/wt)	Q (mL/min)	N (rpm)
1	0.375	112	525
2	0.375	112	700
3	0.267	112	525
4	0.267	112	1050
5	0.267	31	700
6	0.267	112	350
7	0.267	112	700
8	0.267	193	700
9	0.177	112	700
10	0.121	112	700
11	0.419	112	700
12	0.267	64	700
13	0.267	160	700
14	0.267	112	700
15	0.357	112	700
16	0.267	31	700
17	0.267	112	1400
18	0.419	112	700
19	0.267	64	700
20	0.42	112	525
21	0.42	31	350
22	0.42	31	700

A 1.3.3. Large scale

Exp	S/O (wt/wt)	Q (mL/min)	N (rpm)
1	0.267	895	263
2	0.267	895	788
3	0.267	895	394
4	0.267	895	525
5	0.42	895	200
6	0.42	248	400

A 1.4. Graphical representation of the models and the experiments to validate them

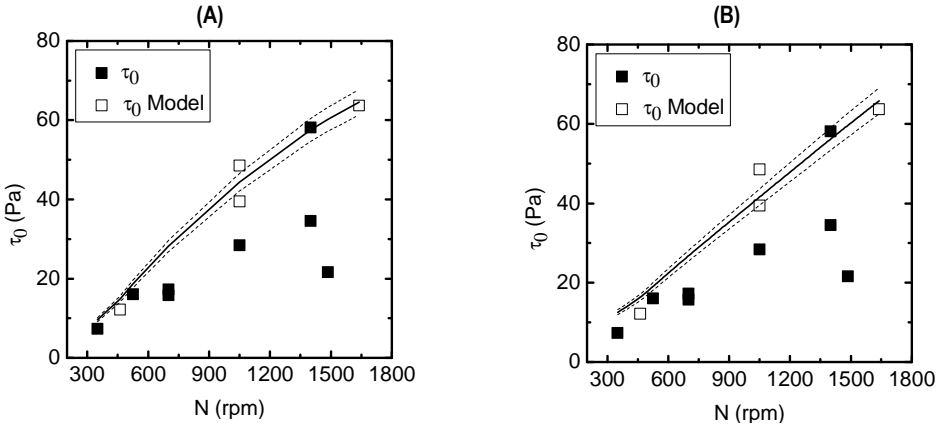


Figure A 1. Yield stress τ_0 at equal S/O and Q at small scale. (A). general model; (B). significant model.

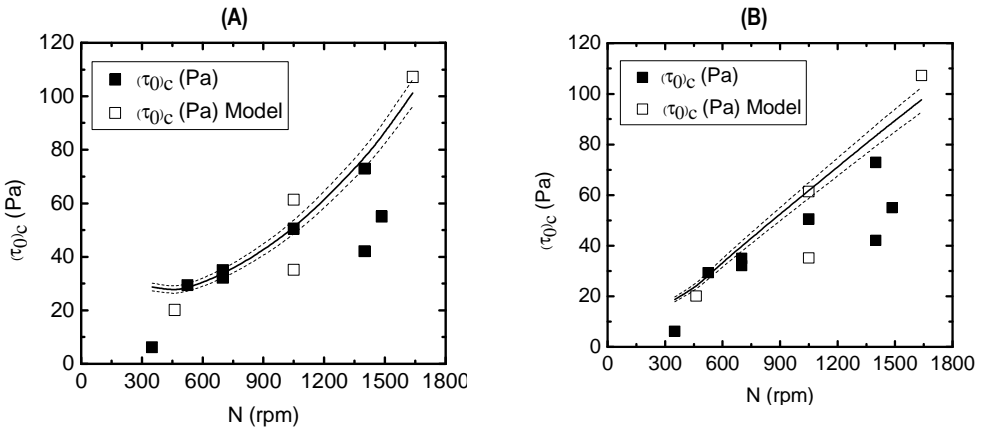


Figure A 2. Critical yield stress $(\tau_0)_c$ at equal S/O and Q at small scale. (A). general model; (B). significant model.

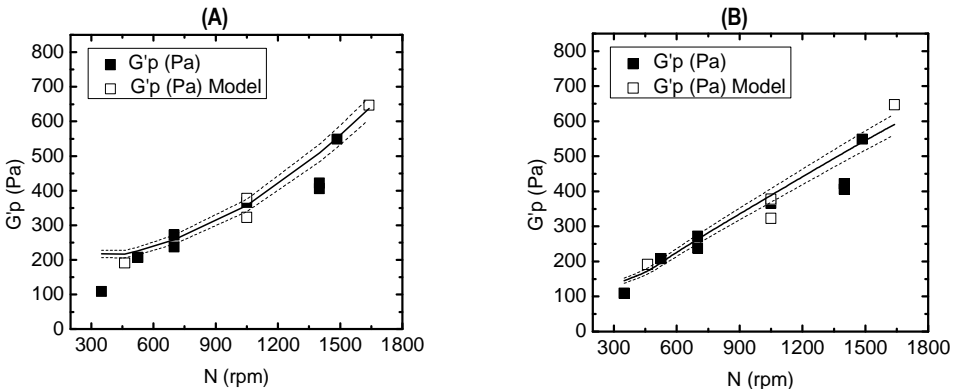


Figure A 3. Storage modulus G' at equal S/O and Q at small scale. (A). general model; (B). significant model.

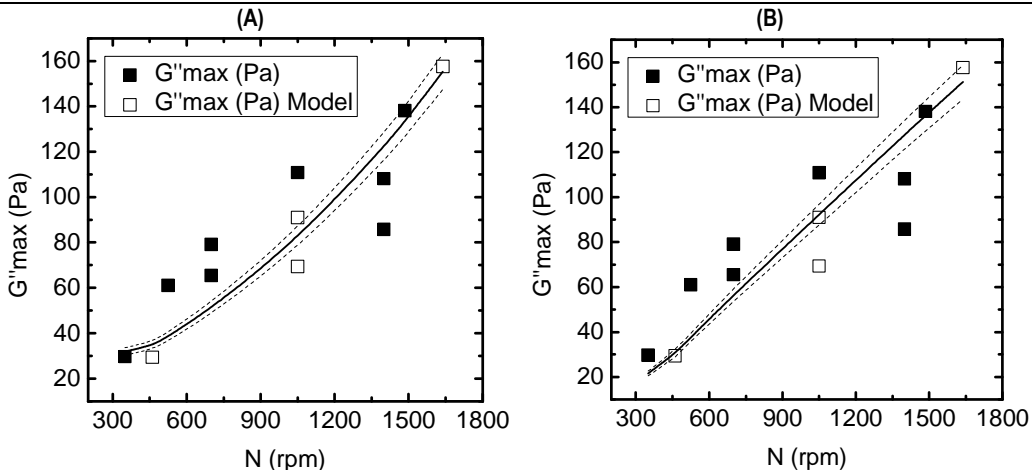


Figure A 4. Loss modulus G''_{max} at equal S/O and Q at small scale. (A). general model; (B). significant model.

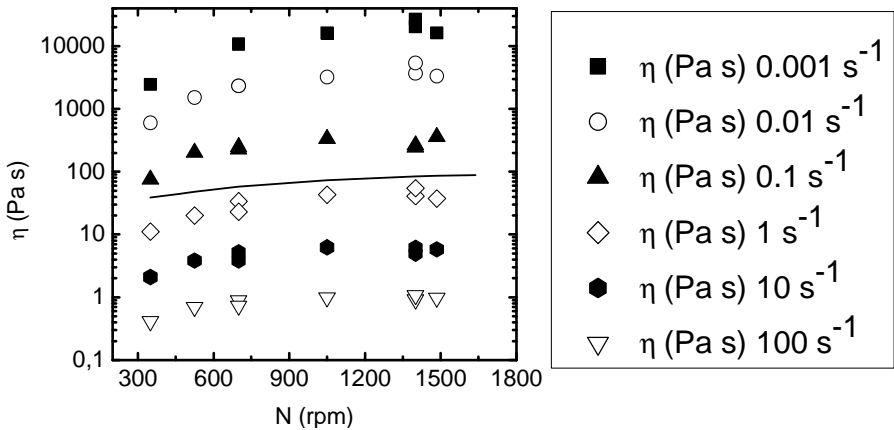


Figure A 5. Viscosity at each gradient at equal S/O and Q at small scale. Models: line.

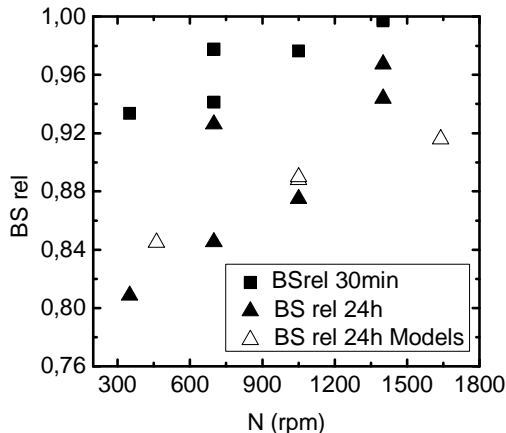


Figure A 6. Relative back scattering at 30 min and 24 h at equal S/O and Q at small scale.

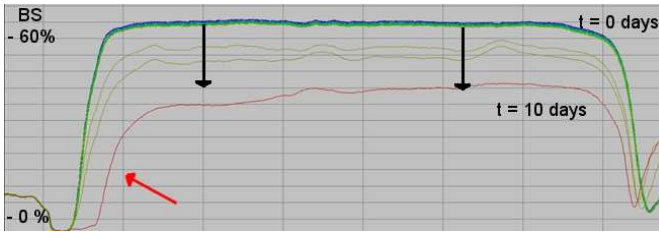


Figure A 7 Back scattering versus cell position at different time. Equal S/O and Q. $N = 1485$ rpm

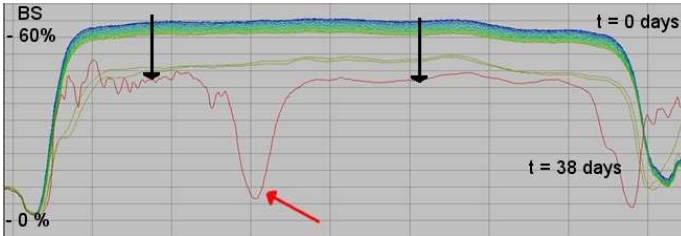


Figure A 8. Back scattering BS versus cell position at different time. Equal S/O and Q. $N = 350$ rpm

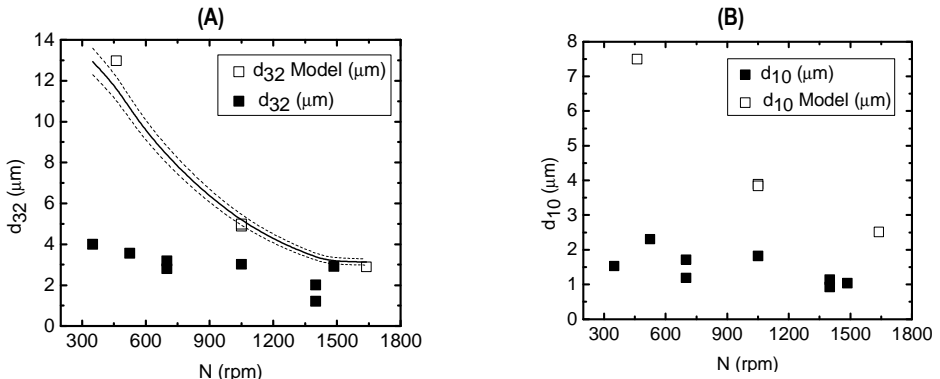


Figure A 9. (A) Sauter mean diameter and (B) mean diameter at equal S/O and Q at small scale.

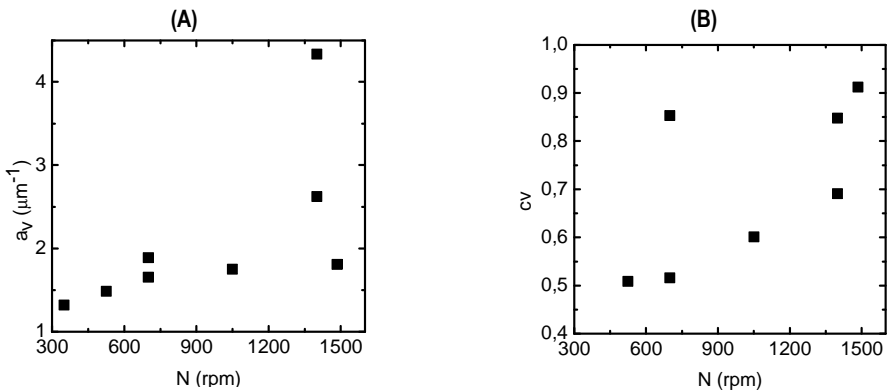


Figure A 10. (A) Surface area of dispersion and (B) coefficient of variation at equal S/O and Q at small scale.

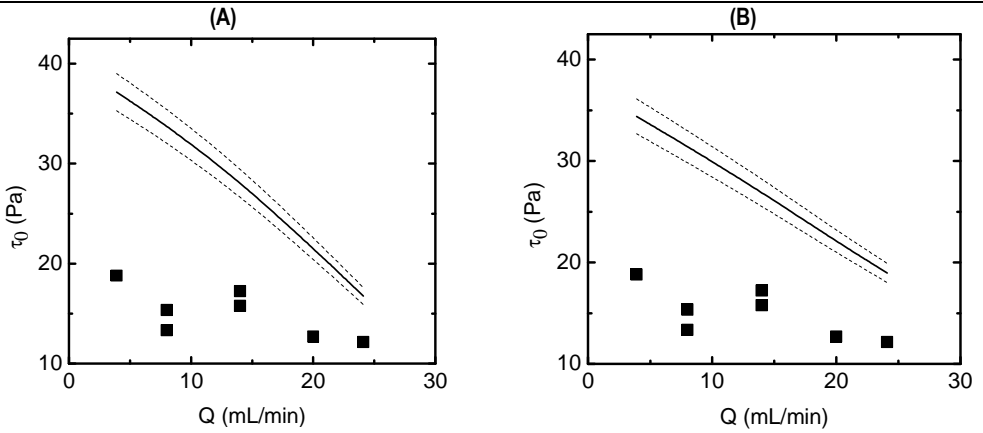


Figure A 11. Yield stress τ_0 at equal S/O and N at small scale. (A). general model; (B). significant model.

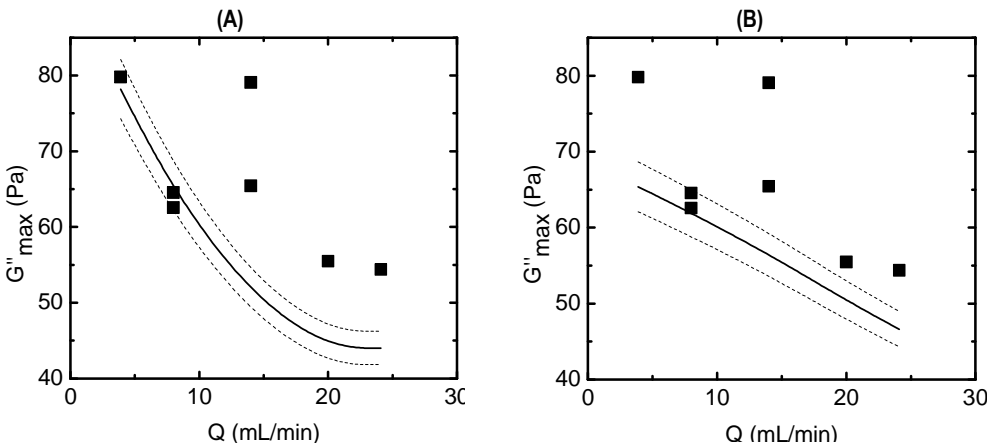


Figure A 12. Loss modulus G''_{max} at equal S/O and N at small scale. (A). general model; (B). significant model.

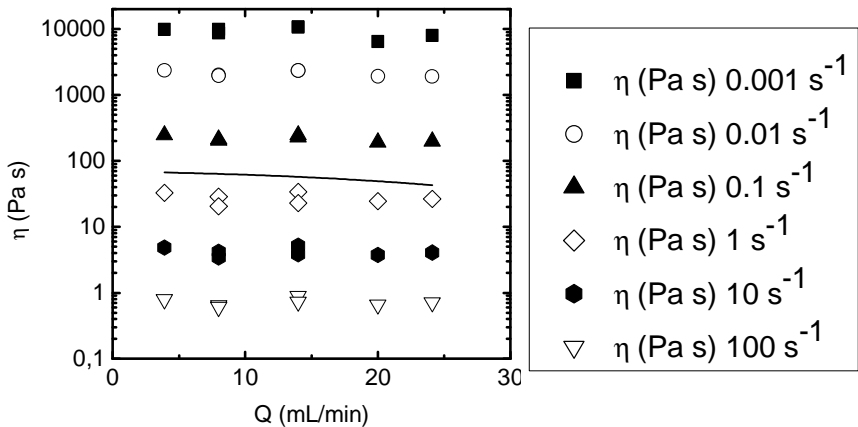


Figure A 13. Viscosity at each gradient at equal S/O and N at small scale. Models: line.

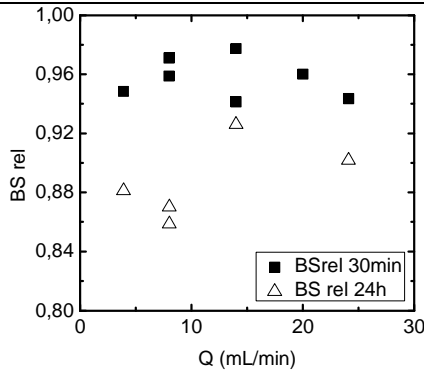


Figure A 14. Relative back scattering at 30 min and 24 h at equal S/O and N at small scale.

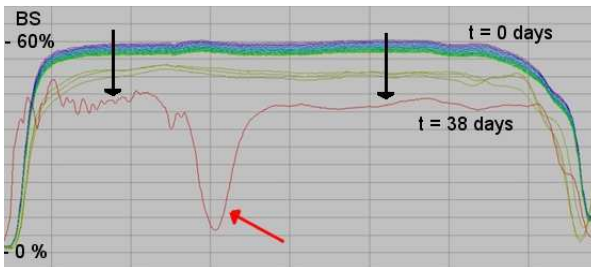


Figure A 15. Back scattering versus cell position at different time. Equal S/O and N . $Q = 3.9$ mL/min

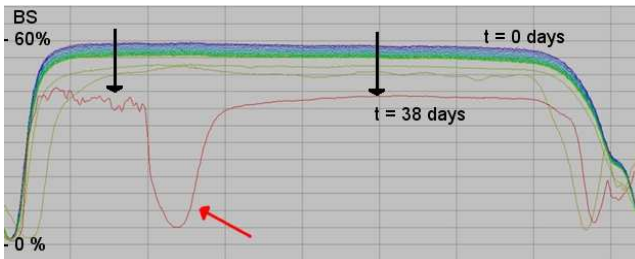


Figure A 16. Back scattering versus cell position at different time. Equal S/O and N . $Q = 24.1$ mL/min

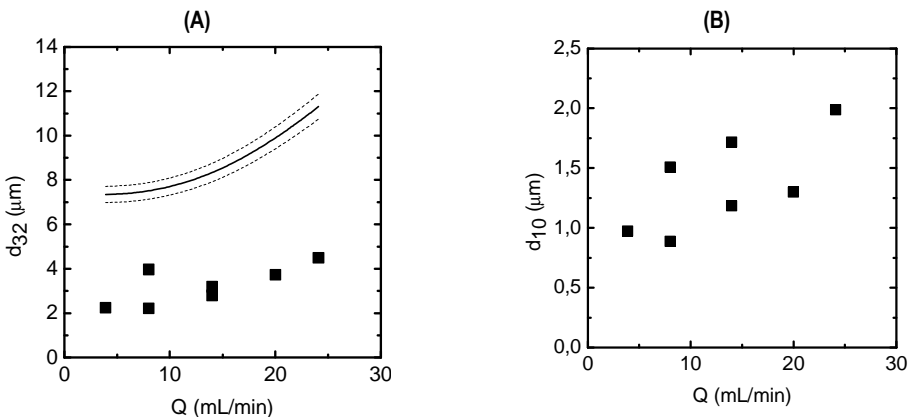


Figure A 17. (A) Sauter mean diameter and (B) mean diameter at equal S/O and N at small scale.

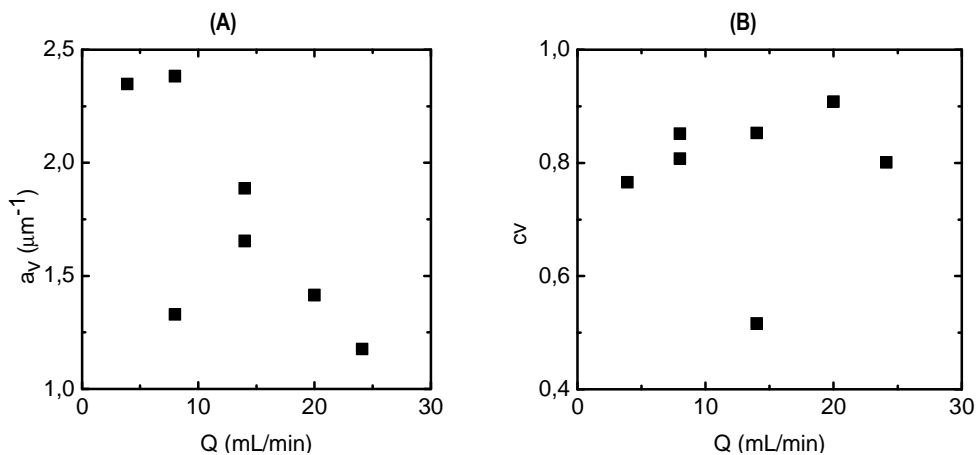


Figure A 18. (A) Surface area of dispersion and (B) coefficient of variation at equal S/O and N at small scale.

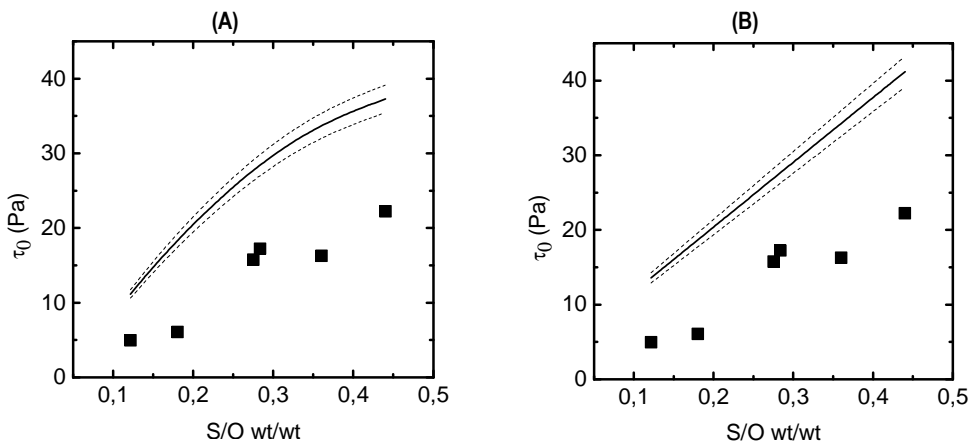


Figure A 19. Yield stress τ_0 at equal N and Q at small scale. (A). general model; (B). significant model.

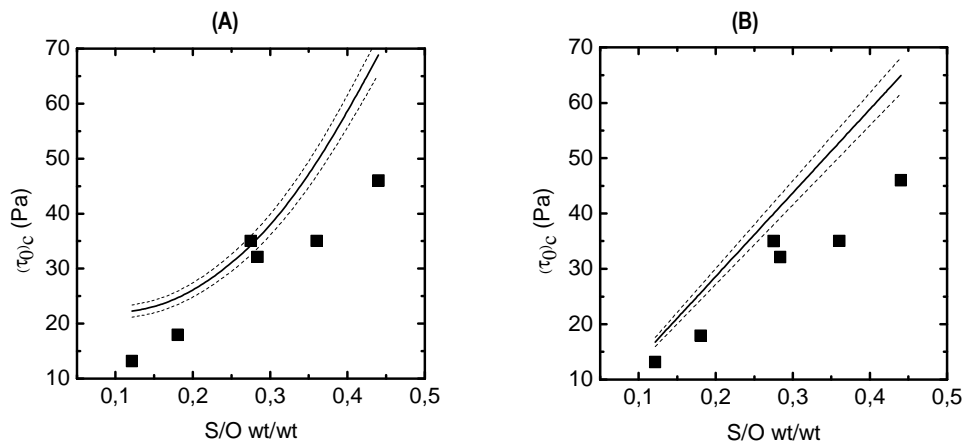


Figure A 20. Critical yield stress $(\tau_0)_c$ at equal N and Q at small scale. (A). general model; (B). significant model.

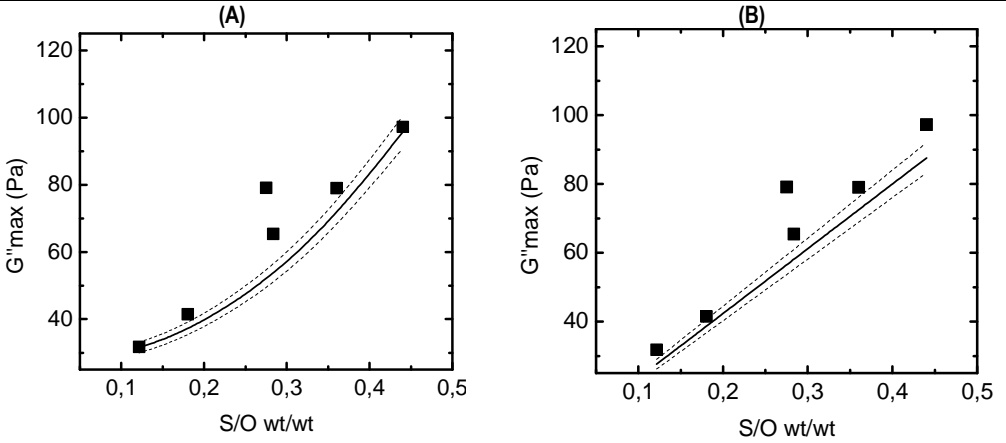


Figure A 21. Loss modulus G''_{max} at equal N and Q at small scale. (A). general model; (B). significant model.

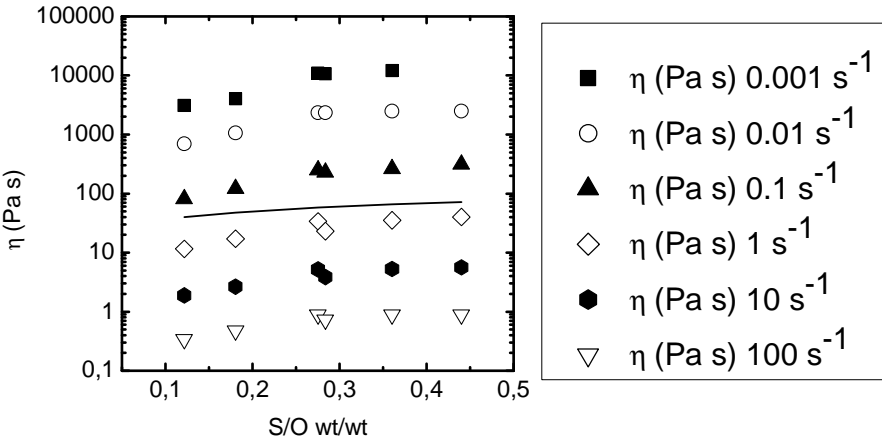


Figure A 22. Viscosity at each gradient at equal N and Q at small scale. Models: line.

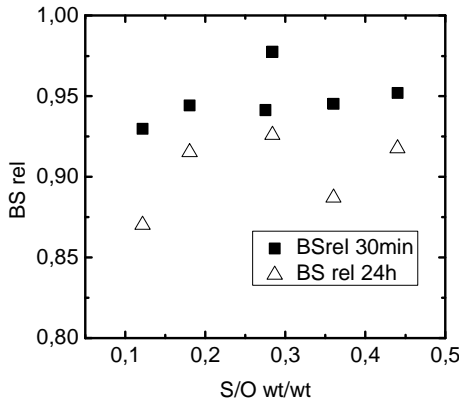


Figure A 23. Relative back scattering at 30 min and 24 h at equal N and Q at small scale.

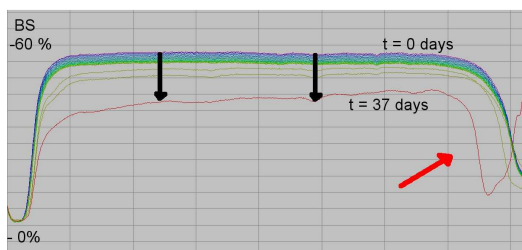


Figure A 24. Back scattering versus cell position at different time. Equal N and Q . $S/O = 0.121$

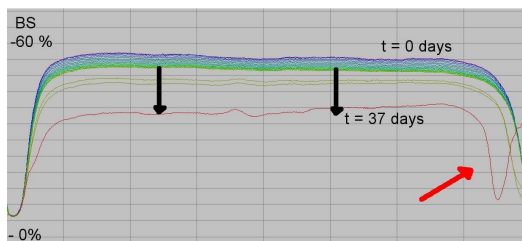


Figure A 25. Back scattering versus cell position at different time. Equal N and Q . $S/O = 0.420$

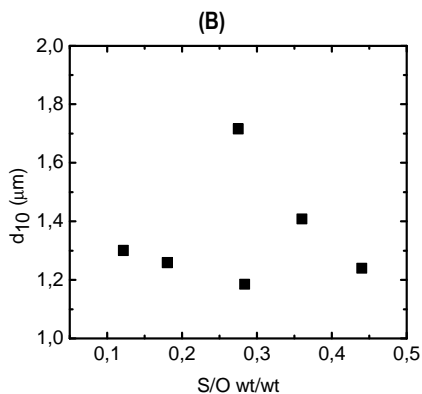
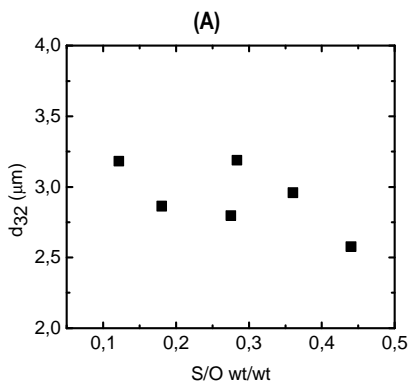


Figure A 26. (A) Sauter mean diameter and (B) mean diameter at equal N and Q at small scale.

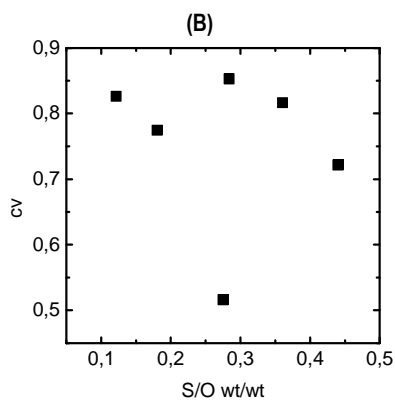
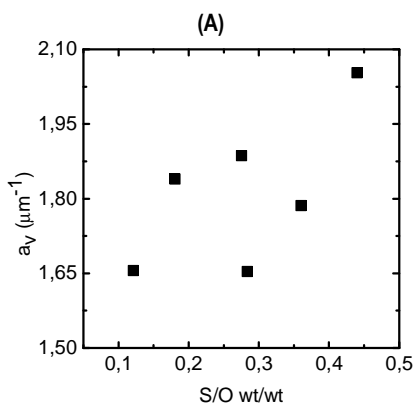


Figure A 27. (A) Surface area of dispersion and (B) coefficient of variation at equal N and Q at small scale.

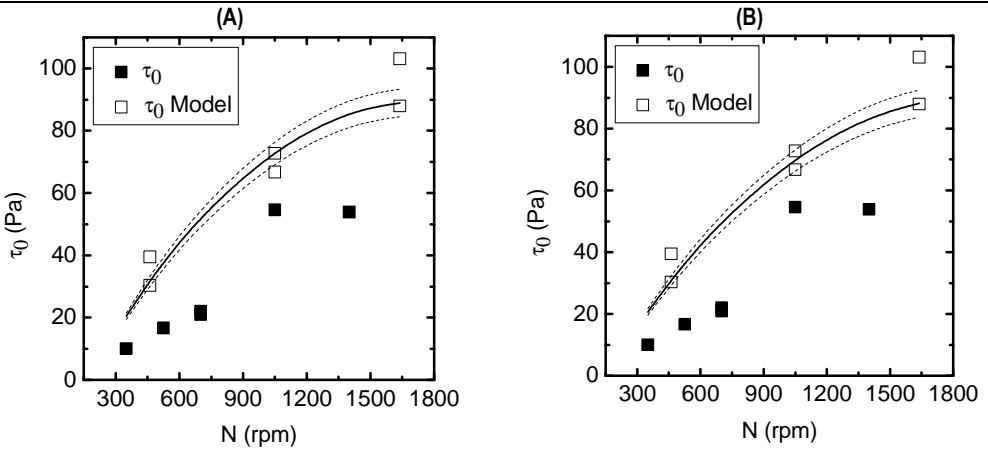


Figure A 28. Yield stress τ_0 at equal S/O and Q at medium scale. (A). general model; (B). significant model.

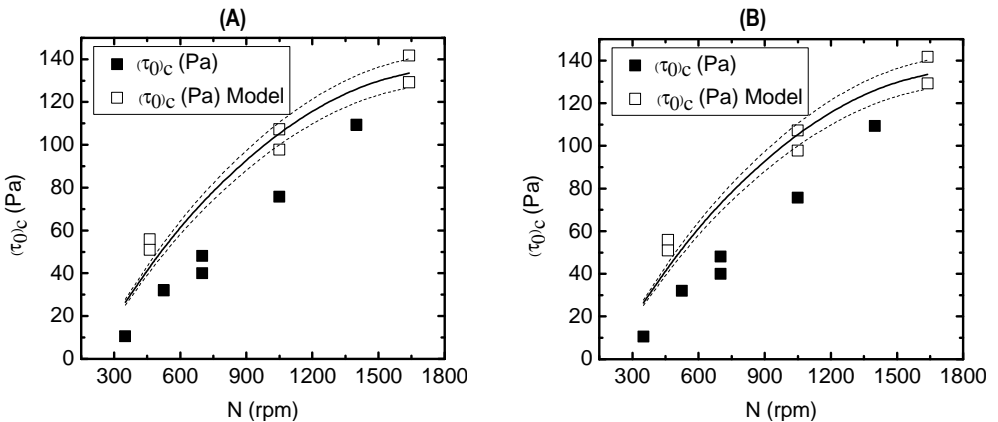


Figure A 29. Critical yield stress $(\tau_0)_c$ at equal S/O and Q at medium scale. (A). general model; (B). significant model.

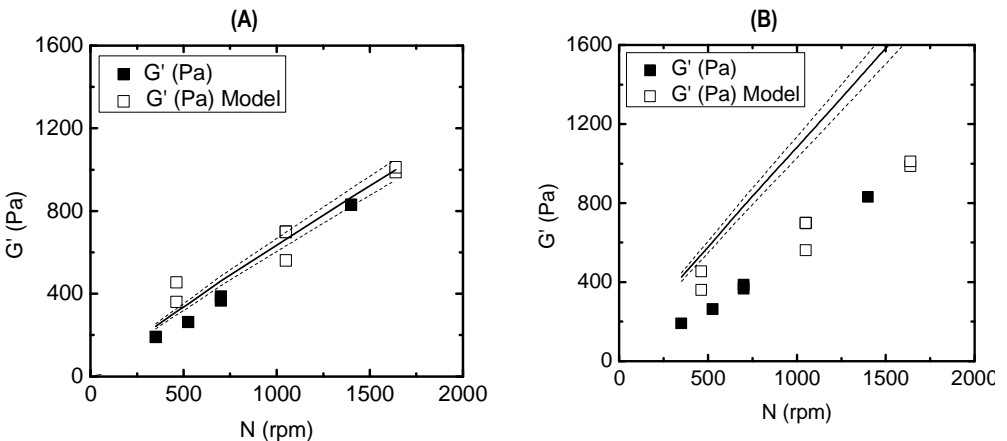


Figure A 30. Storage modulus G' at equal S/O and Q at medium scale. (A). general model; (B). significant model.

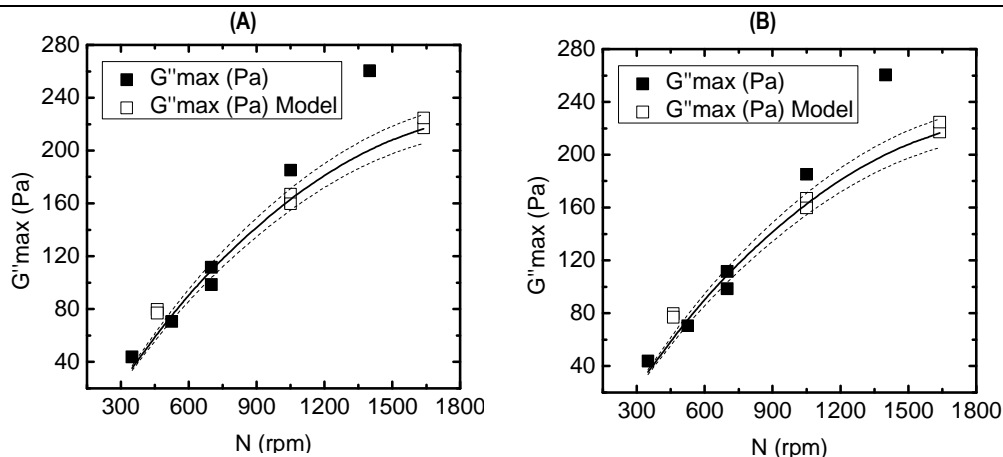


Figure A 31. Loss modulus G''_{max} at equal S/O and Q at medium scale. (A). general model; (B). significant model.

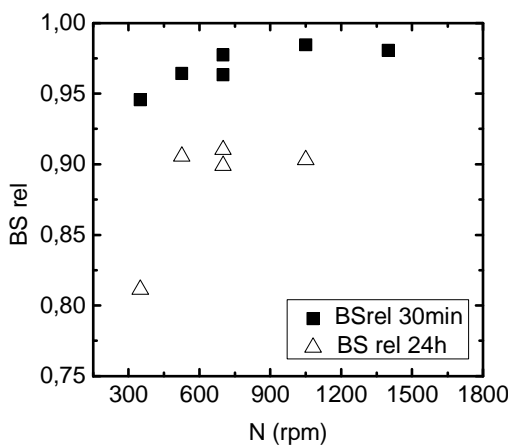


Figure A 32. Relative back scattering at 30 min and 24 h at equal S/O and Q at medium scale.

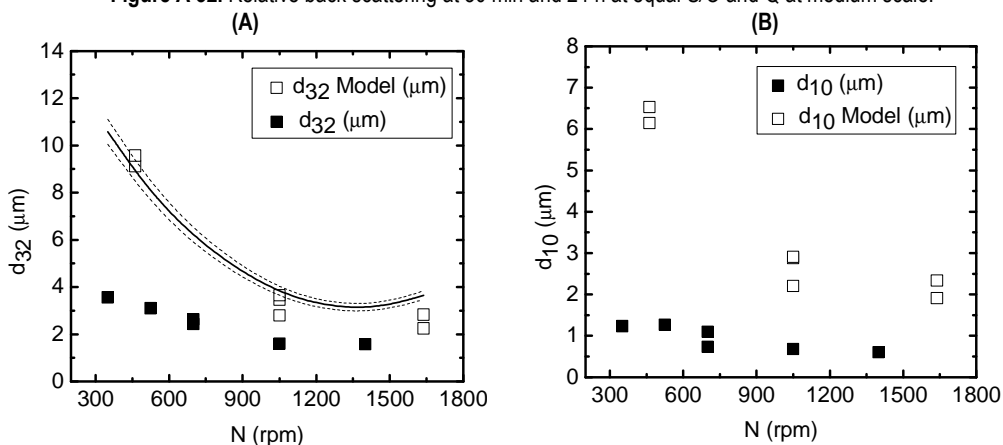


Figure A 33. (A) Sauter mean diameter and (B) mean diameter at equal S/O and Q at medium scale.

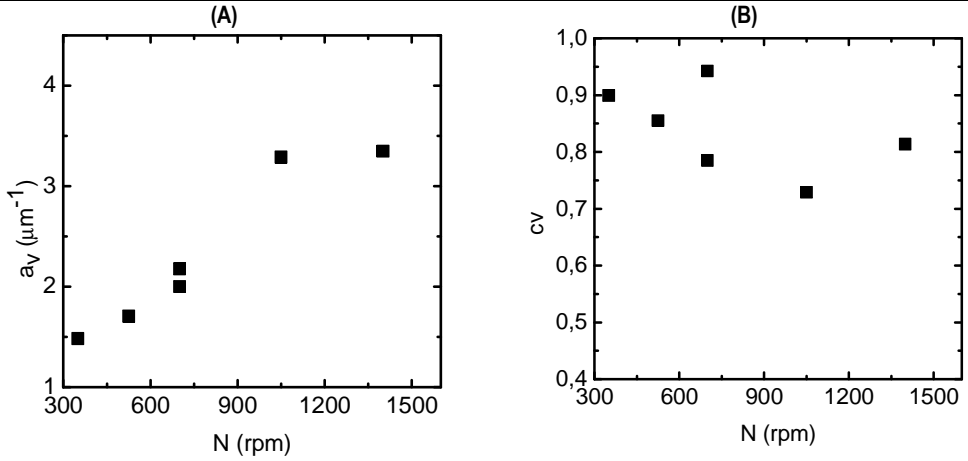


Figure A 34. (A) Surface area of dispersion and (B) coefficient of variation at equal S/O and Q at medium scale.

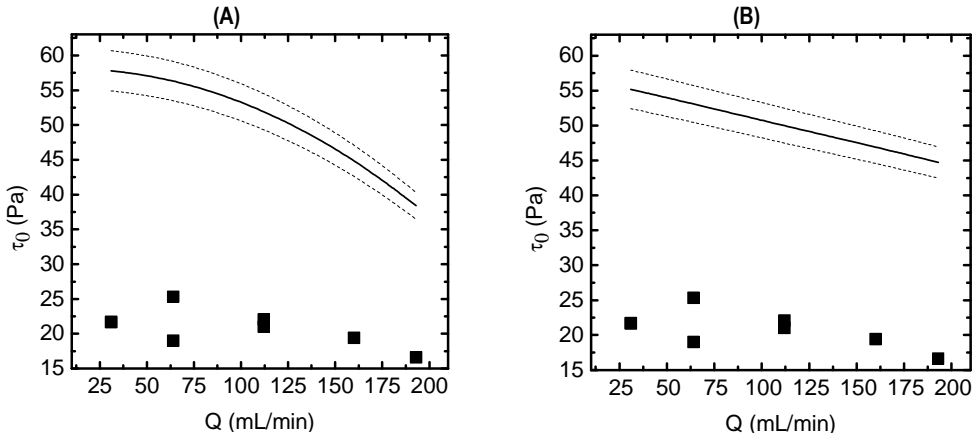


Figure A 35. Yield stress τ_0 at equal S/O and N at medium scale. (A). general model; (B). significant model.

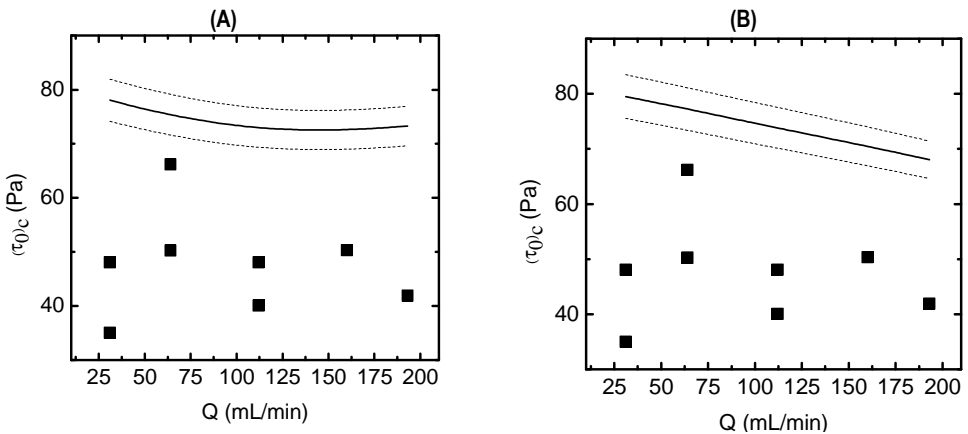


Figure A 36. Critical yield stress $(\tau_0)_c$ at equal S/O and N at medium scale. (A). general model; (B). significant model.

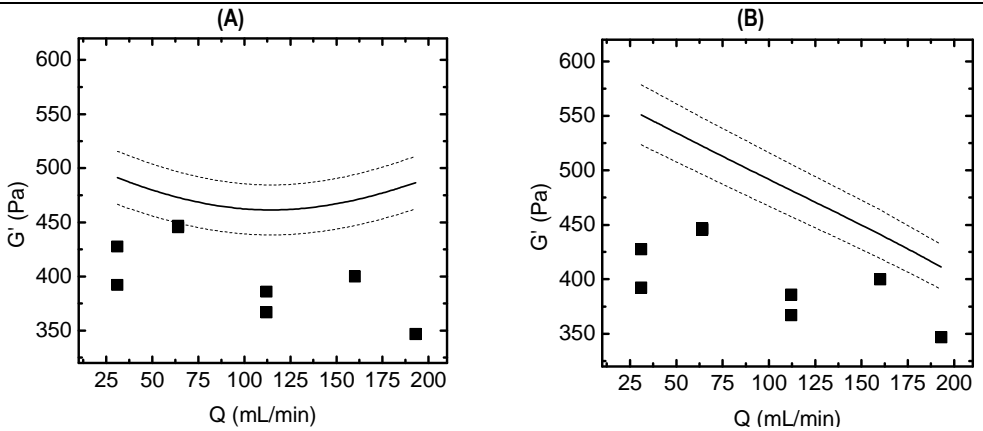


Figure A 37. Storage modulus G' at equal S/O and N at medium scale. (A). general model; (B). significant model.

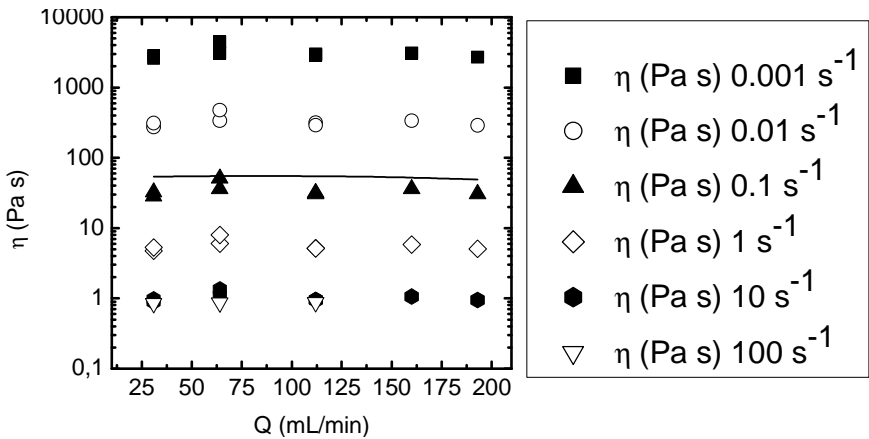


Figure A 38. Viscosity at each gradient at equal S/O and N at medium scale. Models: line.

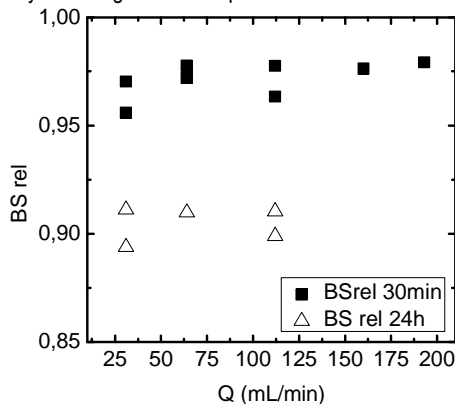


Figure A 39. Relative back scattering at 30 min and 24 h at equal S/O and N at medium scale.

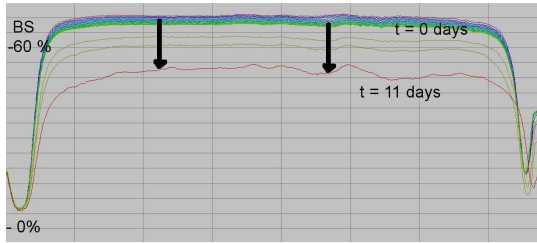


Figure A 40. Back scattering versus cell position at different time. Equal S/O and N . $Q = 31$ mL/min



Figure A 41. Back scattering versus cell position at different time. Equal S/O and N . $Q = 193$ mL/min

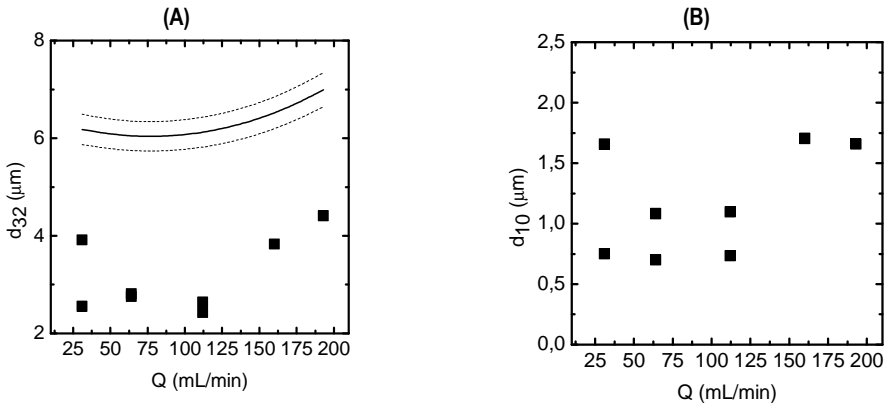


Figure A 42. (A) Sauter mean diameter and (B) mean diameter at equal S/O and N at medium scale.

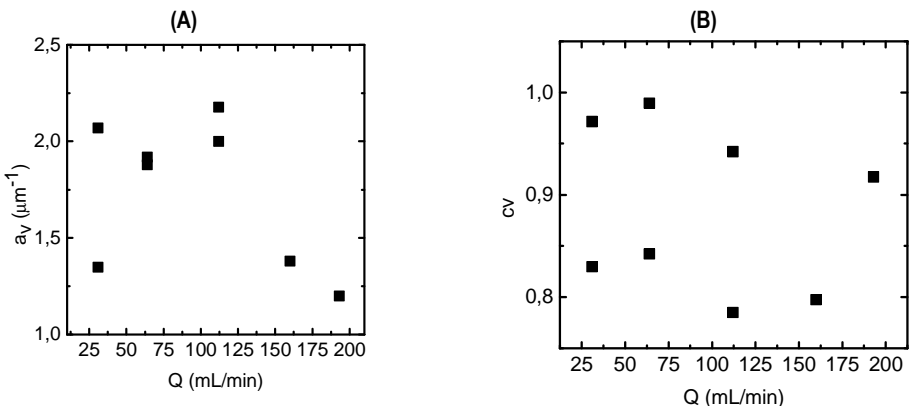


Figure A 43. (A) Surface area of dispersion and (B) coefficient of variation at equal S/O and N at medium scale.

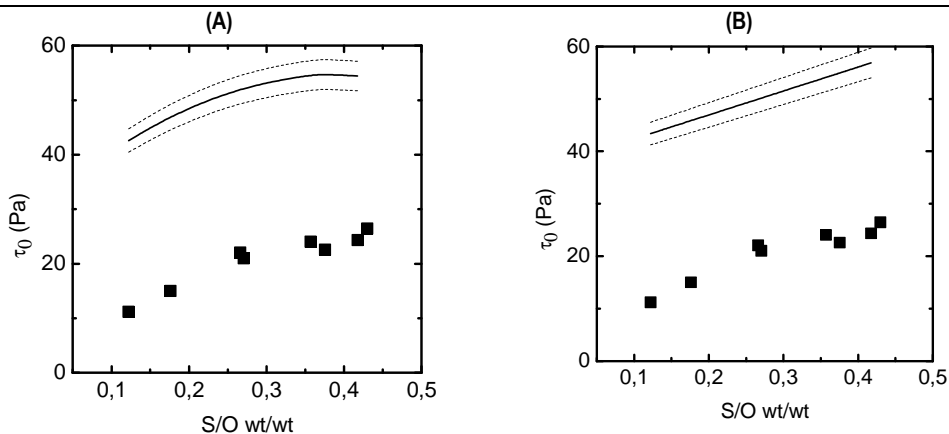


Figure A 44. Yield stress τ_0 at equal Q and N at medium scale. (A). general model; (B). significant model.

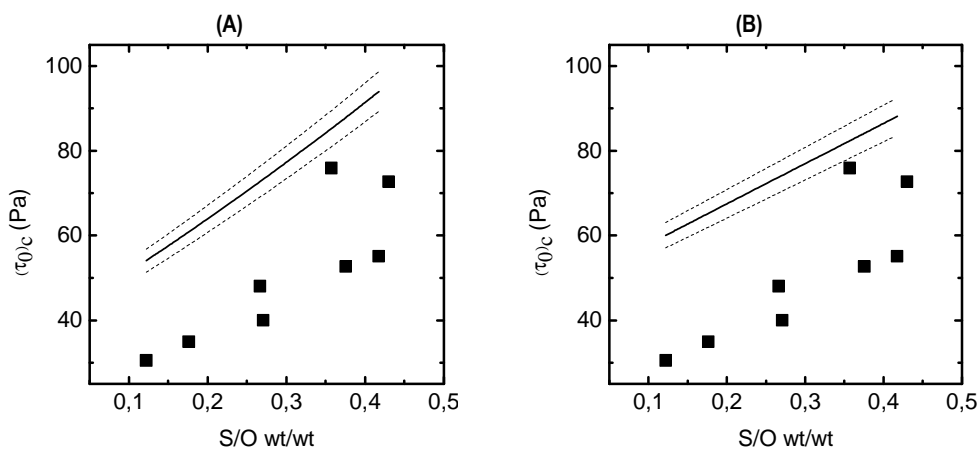


Figure A 45. Critical yield stress $(\tau_0)_c$ at equal Q and N at medium scale. (A). general model; (B). significant model

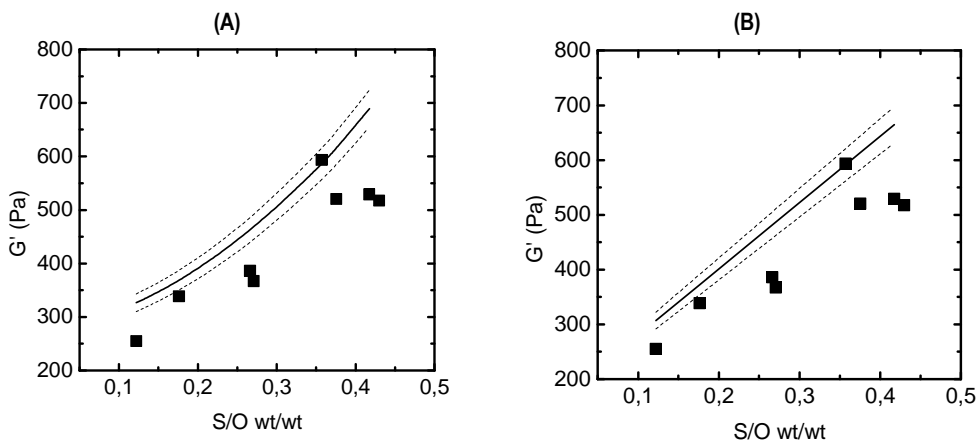


Figure A 46. Storage modulus G' at equal N and Q at medium scale. (A). general model; (B). significant model.

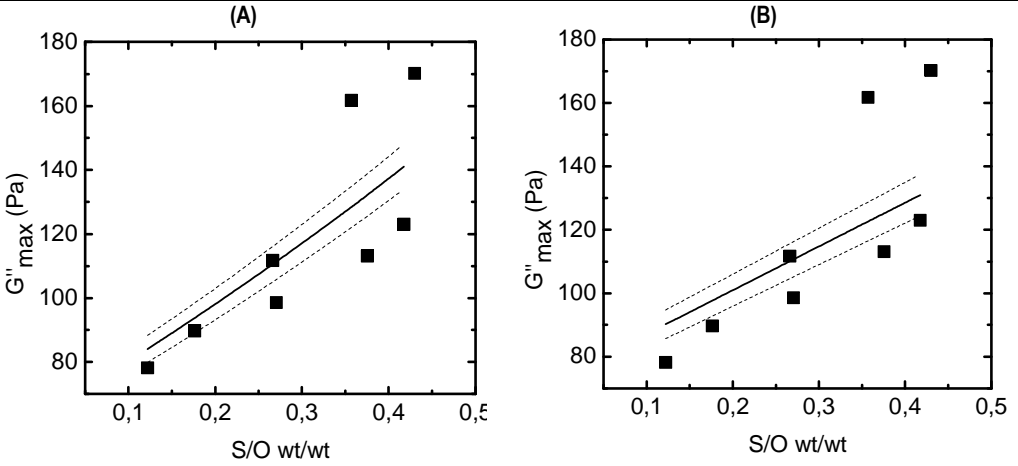


Figure A 47. Loss modulus G''_{max} at equal N and Q at medium scale. (A). general model; (B). significant model.

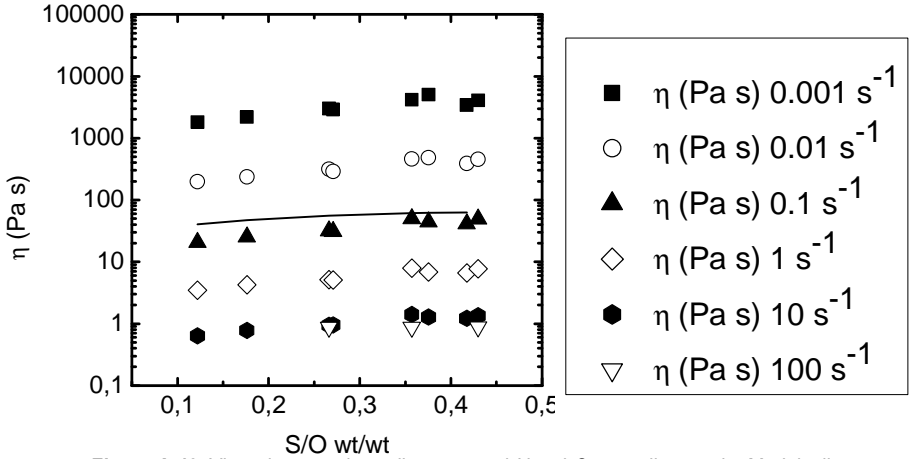


Figure A 48. Viscosity at each gradient at equal N and Q at medium scale. Models: line.

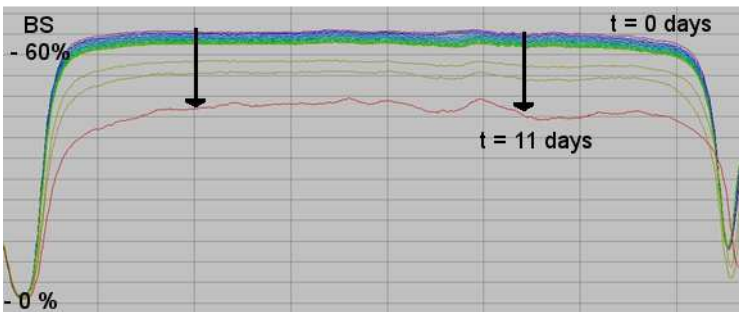


Figure A 49. Back scattering with cell position at each time. Equal N and Q . $S/O = 0.121$.

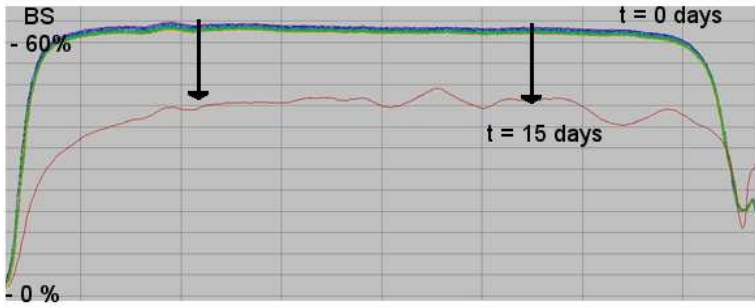


Figure A 50. Back scattering with cell position at each time. Equal N and Q . $S/O = 0.440$.

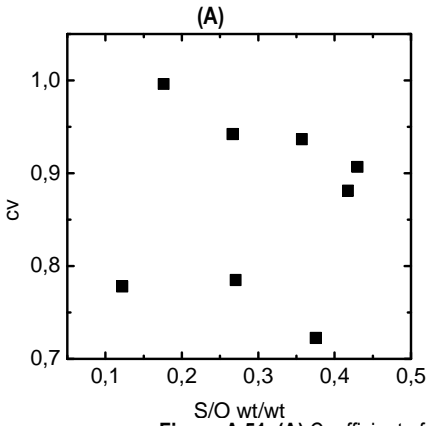


Figure A 51. (A) Coefficient of variation at equal N and Q at medium scale.

A 2. Validation of the scale-up models

A 2.1. Scale-up models at fixed conditions

A 2.1.1. Validation of the scale-up model with equal S/O rate 0.43 and addition time 18.24 min.

The surfactant concentration was fixed at $S/O = 0.43 \pm 0.02$ and the addition time. at $t = 1095$ s (18.24 min). In Table A 1 addition flow rates and stirring rates at each scale are shown.

Table A 1. Addition flow rates and range of stirring rate N at each scale

Scale	t (min)	Q (mL/min)	Lower N (rpm)	Higher N (rpm)
Small	18.24	3.9	525	1085
Medium	18.24	31	350	700
Large	18.24	248	400	400

Storage module		Loss modulus		Critical yield stress	
α	0.75	α	0.61	α	0.56
Factors	$R^2=0.986$	Factors	$R^2=0.969$	Factors	$R^2=0.952$
cnt	43.2579	cnt	10.8648	cnt	9.20127
$ND^{0.75}$	84.4764	$ND^{0.61}$	14.1284	$ND^{0.56}$	5.05794
Yield stress		Viscosity at $\dot{\gamma}=1 \text{ s}^{-1}$		d_{32}	
α	0.57	α	0.62	α	0.91
Factors	$R^2=0.904$	Factors	$R^2=0.999$	Factors	$R^2=0.738$
cnt	-0.642966	cnt	3.52467	cnt	3.52964
$ND^{0.57}$	3.19395	$ND^{0.42}$	4.47322	$ND^{0.58}$	-0.28099

Storage module		Loss modulus		Critical yield stress	
α	0.62	α	0.62	α	0.62
Factors	$R^2=0.938$	Factors	$R^2=0.968$	Factors	$R^2=0.941$
cnt	46.3507	cnt	10.7535	cnt	9.09774
$ND^{0.62}$	60.2169	$ND^{0.62}$	14.4992	$ND^{0.62}$	5.91555
Yield stress		Viscosity at $\dot{\gamma}=1 \text{ s}^{-1}$			
α	0.62	α	0.62		
Factors	$R^2=0.899$	Factors	$R^2=0.999$		
cnt	-0.71094	cnt	3.52467		
$ND^{0.62}$	3.64142	$ND^{0.62}$	4.47322		

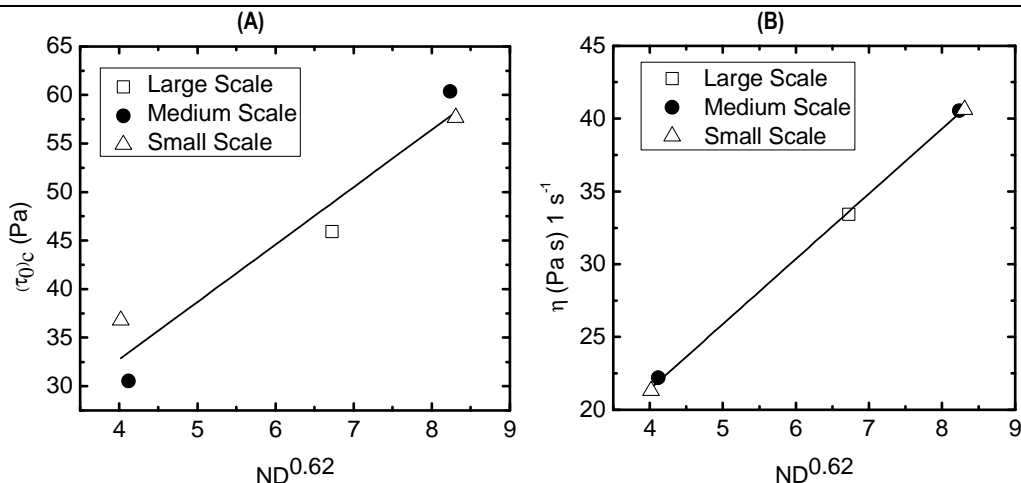


Figure A 52. (A) Scale-up lineal model $(\tau_0)_c$ ($\alpha = 0.62$) and the current experimental values. $t = 18.24 \text{ min}$ / $S/O = 0.43 \pm 0.02$. (B). Scale-up general model η (1 s^{-1}) ($\alpha = 0.62$) and the current experimental values. $t = 18.24 \text{ min}$ / $S/O = 0.43 \pm 0.02$.

A 2.1.2 Validation of the scale-up model with equal S/O rate 0.43 and addition time 5.03 min.

The experiments were carried out with a surfactant oil ratio $S/O = 0.43 \pm 0.02$ and the addition time at $t = 303 \text{ s}$ (5.08 min). The addition flow rates Q is different at each scale (Table) if t remains constant due to the change of effective volume V . $Q = V/t$. The agitation speed N is varied between 200 rpm and 1050 rpm depending on the scale.

Table A 2 Addition flow rates and range of stirring rate N at each scale.

Scale	t (min)	Q (mL/min)	Lower N (rpm)	Higher N (rpm)
Small	5.08	14.0	350	700
Medium	5.08	112	525	700
Large	5.08	895	200	200

Storage module		Loss modulus		Critical yield stress	
α	0.62	α	0.59	α	0.44
Factors	$R^2 = 0.948$	Factors	$R^2 = 0.895$	Factors	$R^2 = 0.923$
cnt	-37.4252	cnt	-21.1968	cnt	-17.3548
$ND^{0.62}$	69.3024	$ND^{0.59}$	19.1331	$ND^{0.44}$	6.55326

Yield stress		Viscosity at $\dot{\gamma} = 1 \text{ s}^{-1}$		d_{32}	
α	0.51	α	0.32	α	-0.55
Factors	R²=0.876	Factors	R²=0.935	Factors	R²=0.539
cnt	-0.412588	cnt	-8.11513	cnt	4.27962
$ND^{0.51}$	2.58185	$ND^{0.31}$	2.98034	$ND^{0.58}$	-0.007

Storage module		Loss modulus		Critical yield stress	
α	0.49	α	0.49	α	0.49
Factors	R²=0.968	Factors	R²=0.888	Factors	R²=0.921
cnt	-51.3225	cnt	-24.4002	cnt	-16.48
$ND^{0.49}$	51.3377	$ND^{0.49}$	15.1898	$ND^{0.49}$	7.34829

Yield stress		Viscosity at $\dot{\gamma} = 1 \text{ s}^{-1}$	
α	0.49	α	0.49
Factors	R²=0.876	Factors	R²=0.908
cnt	-0.528452	cnt	-6.10035
$ND^{0.49}$	2.46649	$ND^{0.49}$	4.37982

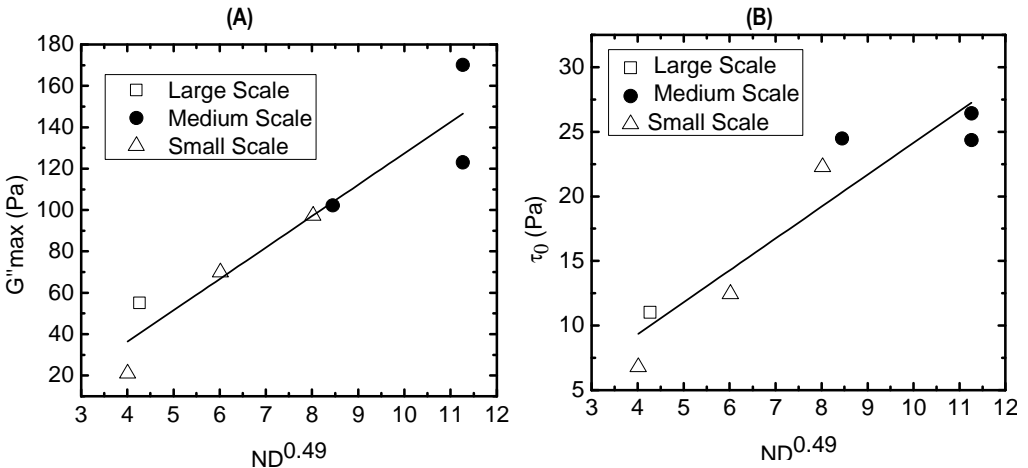


Figure A 53. (A) Scale-up linear model G'' ($\alpha = 0.49$) and the current experimental values. $t = 5.08 \text{ min}$ / $S/O = 0.43 \pm 0.02$. (B). Scale-up general model $(\tau_0)_c$ ($\alpha = 0.49$) and the current experimental values. $t = 5.08 \text{ min}$ / $S/O = 0.43 \pm 0.02$.

A 2.1.3. Validation of the scale-up model with equal S/O rate 0.267 and addition time

5.08 min.

The experiments were performed with a surfactant oil ratio $S/O = 0.267 \pm 0.02$ and the addition time at $t = 303$ s (5.08min). Table A 1 shows the addition flow rate at each scale The agitation speed N is varied between 200 rpm and 1485 rpm depending on the scale.

Storage module		Loss modulus		Critical yield stress	
α	0.67	α	0.63	α	0.51
Factors	R²=0.896	Factors	R²=0.817	Factors	R²=0.799
cnt	9.63274	cnt	0.559308	cnt	-6.83461
$ND^{0.67}$	49.5007	$ND^{0.63}$	12.4511	$ND^{0.51}$	4.80066
Yield stress		Viscosity at $\dot{\gamma} = 1 \text{ s}^{-1}$		d_{32}	
α	0.43	α	0.34	α	0.58
Factors	R²=0.868	Factors	R²=0.909	Factors	R²=0.810
cnt	-2.76528	cnt	-2.74074	cnt	4.20347
$ND^{0.43}$	2.01416	$ND^{0.42}$	2.10874	$ND^{0.58}$	-0.1738

Storage module		Loss modulus		Critical yield stress	
α	0.53	α	0.53	α	0.53
Factors	R²=0.860	Factors	R²=0.800	Factors	R²=0.798
cnt	39.1667	cnt	5.62904	cnt	-7.37805
$ND^{0.53}$	30.847	$ND^{0.53}$	9.00033	$ND^{0.53}$	5.12274
Yield stress		Viscosity at $\dot{\gamma} = 1 \text{ s}^{-1}$			
α	0.53	α	0.53		
Factors	R²=0.848	Factors	R²=0.727		
cnt	-3.6695	cnt	2.32741		
$ND^{0.53}$	2.71742	$ND^{0.53}$	2.72357		

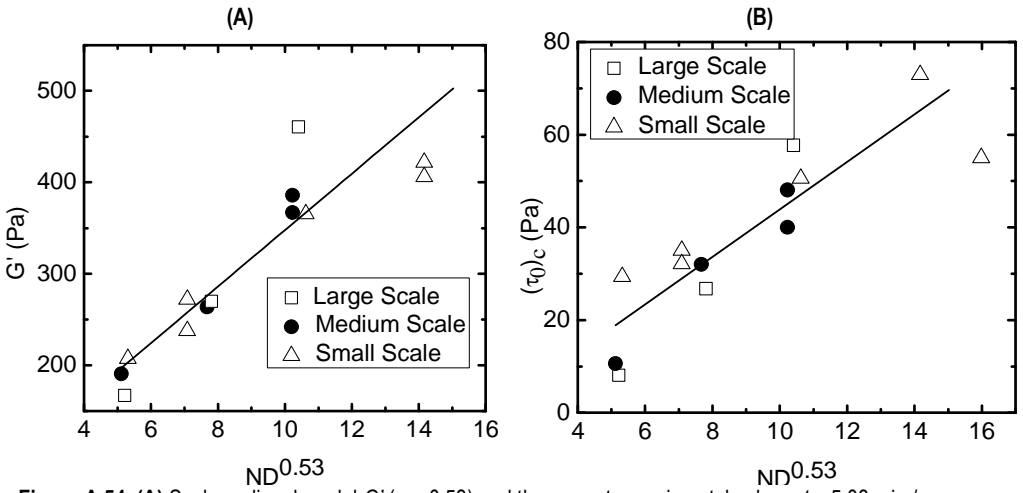


Figure A 54. (A) Scale-up lineal model G' ($\alpha = 0.53$) and the current experimental values. $t = 5.08$ min / $S/O = 0.267 \pm 0.020$. (B). Scale-up general model $(\tau_0)_c$ ($\alpha = 0.53$) and the current experimental values. $t = 5.08$ min / $S/O = 0.267 \pm 0.020$.

A 2.2. Scale-up models from general models at medium and small scale

Table 11. Power law exponent α from general models at small and medium scale

	Storage modulus	Loss modulus	Yield stress	Critical yield stress
0.267 ± 0.020 303 s (5.08 min)	$\alpha = 0.81$	$\alpha = 0.9$	$\alpha = 0.73$	$\alpha = 1.06$
	$R^2 = 0.995$	$R^2 = 0.874$	$R^2 = 0.862$	$R^2 = 0.881$
	Viscosity at $\dot{\gamma} = 1 \text{ s}^{-1}$	d_{32}	Rheological parameters	
	$\alpha = -0.07$	$\alpha = 0.23$	$\alpha = 0.71$	
	$R^2 = 0.600$	$R^2 = 0.675$	$\Sigma R^2 = 3.972$	
	Storage modulus	Loss modulus	Yield stress	Critical yield stress
0.43 ± 0.02 303 s (5.08 min)	$\alpha = 1.05$	$\alpha = 0.72$	$\alpha = 0.52$	$\alpha = 0.60$
	$R^2 = 0.883$	$R^2 = 0.976$	$R^2 = 0.977$	$R^2 = 0.957$
	Viscosity at $\dot{\gamma} = 1 \text{ s}^{-1}$	d_{32}	Rheological parameters	
	$\alpha = -0.04$	$\alpha = -0.18$	$\alpha = 0.55$	
	$R^2 = 0.892$	$R^2 = 0.733$	$\Sigma R^2 = 4.381$	
	Storage modulus	Loss modulus	Yield stress	Critical yield stress
0.43 ± 0.02 1095 s (18.24 min)	$\alpha = 1.57$	$\alpha = 0.80$	$\alpha = 0.35$	$\alpha = 0.35$
	$R^2 = 0.971$	$R^2 = 0.971$	$R^2 = 0.965$	$R^2 = 0.895$
	Viscosity at $\dot{\gamma} = 1 \text{ s}^{-1}$	d_{32}	Rheological parameters	
	$\alpha = -0.01$	$\alpha = 0.01$	$\alpha = 0.57$	
	$R^2 = 0.728$	$R^2 = 0.434$	$\Sigma R^2 = 4.123$	

A 2.3. Scale-up models from all the current experiments

A 2.3.1. Specific models

Storage module		Viscosity at $\dot{\gamma}=1 \text{ s}^{-1}$		Yield stress	
$\alpha = 0.73$		$\alpha = 0.45$		$\alpha = 0.49$	
All factors	$R^2=0.945$	All factors	$R^2=0.864$	All factors	$R^2=0.779$
cnt	-203.392	cnt	-39.5753	cnt	-33.8482
SO	445.733	SO	97.6858	SO	138.498
t	23.6241	t	2.58375	t	1.01195
ND $^\alpha$	30.5123	ND $^\alpha$	3.96059	ND $^\alpha$	2.14001
SO·SO	-525.63	SO·SO	-135.997	SO·SO	-164.168
SO·t	-1.92463	SO·t	-0.524705	SO·t	0.257605
SO·ND $^\alpha$	142.917	SO·ND $^\alpha$	5.00092	SO·ND $^\alpha$	0.35003
t·t	-0.813	t·t	-0.068067	t·t	-0.036103
t·ND $^\alpha$	-0.560247	t·ND $^\alpha$	-0.0845639	t·ND $^\alpha$	-0.0251517
ND $^\alpha$ ·ND $^\alpha$	0.226533	ND $^\alpha$ ·ND $^\alpha$	-0.0996281	ND $^\alpha$ ·ND $^\alpha$	0.0273247

Loss modulus		Critical yield stress	
$\alpha = 0.77$		$\alpha = 0.66$	
All factors	$R^2=0.885$	All factors	$R^2=0.870$
cnt	-28.4948	cnt	-34.3082
SO	-32.3791	SO	12.3166
t	10.2673	t	5.61204
ND $^\alpha$	2.82603	ND $^\alpha$	4.26674
SO·SO	61.6904	SO·SO	-13.3294
SO·t	-5.92729	SO·t	-2.77061
SO·ND $^\alpha$	50.374	SO·ND $^\alpha$	18.7187
t·t	-0.247339	t·t	-0.119006
t·ND $^\alpha$	-0.573033	t·ND $^\alpha$	-0.316812
ND $^\alpha$ ·ND $^\alpha$	0.753539	ND $^\alpha$ ·ND $^\alpha$	0.00220542

A 2.3.2. Global models (equal α)

Storage module		Viscosity at $\dot{\gamma} = 1 \text{ s}^{-1}$		Yield stress	
$\alpha = 0.63$		$\alpha = 0.63$		$\alpha = 0.63$	
All factors	$R^2=0.933$	All factors	$R^2=0.837$	All factors	$R^2=0.762$
cnt	-241.047	cnt	-26.6488	cnt	-30.0252
SO	531.327	SO	65.5977	SO	128.376
t	22.2054	t	2.77495	t	1.1478
ND $^\alpha$	30.8485	ND $^\alpha$	3.96419	ND $^\alpha$	2.43186
SO·SO	-567.285	SO·SO	-113.496	SO·SO	-162.611
SO·t	0.0790068	SO·t	-1.05983	SO·t	0.160984
SO·ND $^\alpha$	99.2951	SO·ND $^\alpha$	11.2393	SO·ND $^\alpha$	1.97795
t·t	-0.79194	t·t	-0.0683013	t·t	-0.0381033
t·ND $^\alpha$	-0.36922	t·ND $^\alpha$	-0.136258	t·ND $^\alpha$	-0.0476094
ND $^\alpha$ ·ND $^\alpha$	-0.0862289	ND $^\alpha$ ·ND $^\alpha$	-0.172986	ND $^\alpha$ ·ND $^\alpha$	0.067956

Loss modulus		Critical yield stress	
$\alpha = 0.63$		$\alpha = 0.63$	
All factors	$R^2=0.866$	All factors	$R^2=0.870$
cnt	-36.2677	cnt	-36.3202
SO	-19.3378	SO	16.2306
t	9.57588	t	5.56571
ND $^\alpha$	3.78451	ND $^\alpha$	4.34475
SO·SO	54.0548	SO·SO	-15.4667
SO·t	-5.06703	SO·t	-2.67904
SO·ND $^\alpha$	33.0044	SO·ND $^\alpha$	16.8435
t·t	-0.244244	t·t	-0.118914
t·ND $^\alpha$	-0.340715	t·ND $^\alpha$	-0.290576
ND $^\alpha$ ·ND $^\alpha$	0.290713	ND $^\alpha$ ·ND $^\alpha$	-0.0126529

A 2.3.3. Comparison between specific and global (equal α) models

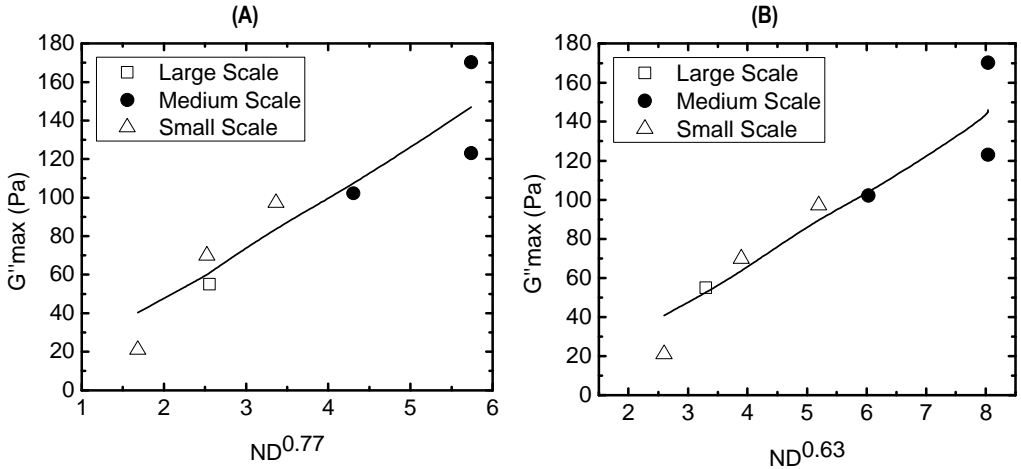


Figure A 55. (A) Scale-up specific model for G''_{max} ($\alpha = 0.77$) and the current experimental values. $t = 5.08$ min/ $S/O = 0.43 \pm 0.02$. **(B)** Scale-up global model for G''_{max} ($\alpha = 0.63$) and current experimental values. $t = 5.08$ min/ $S/O = 0.43 \pm 0.02$.

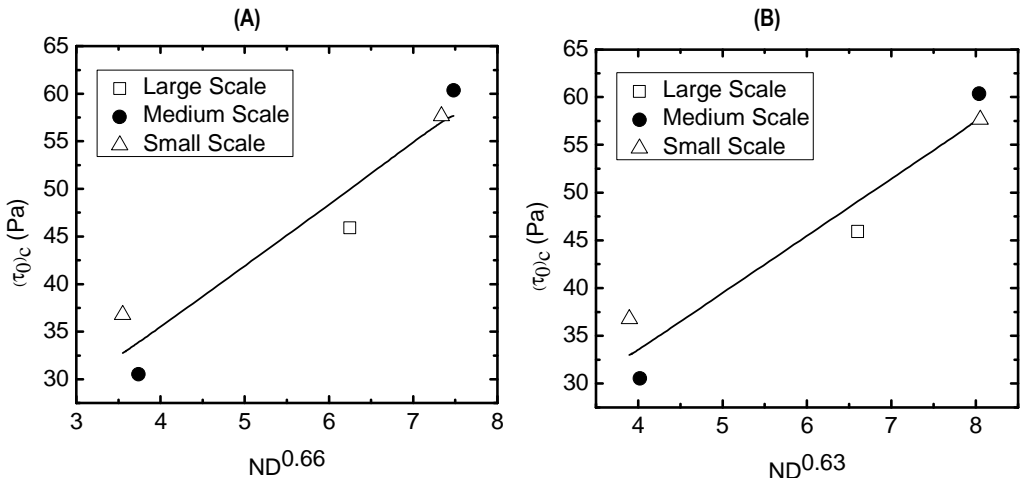


Figure A 56. (A) Scale-up specific model for $(\tau_0)_c$ ($\alpha = 0.66$) and the current experimental values. $t = 18.24$ min/ $S/O = 0.43 \pm 0.02$. **(B)** Scale-up global model for $(\tau_0)_c$ ($\alpha = 0.63$) and the current experimental values. $t = 18.24$ min/ $S/O = 0.43 \pm 0.02$.

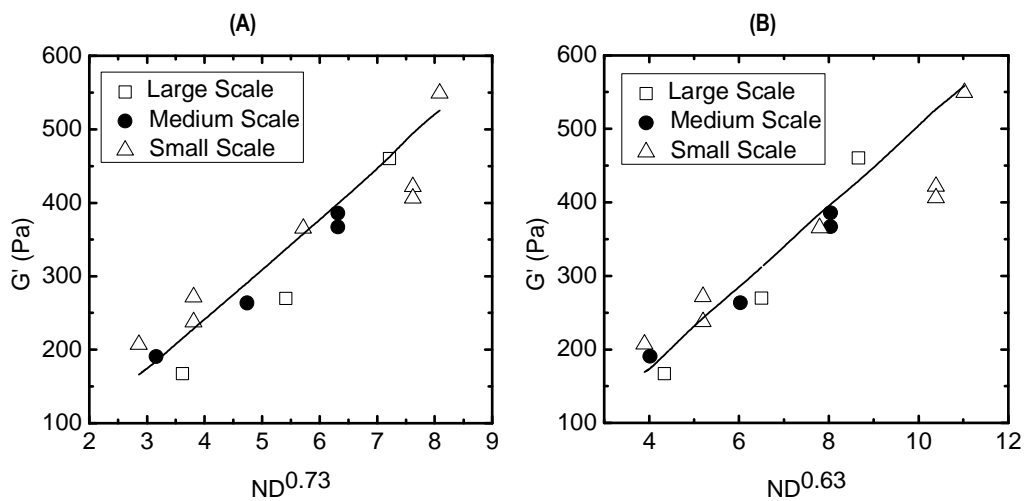
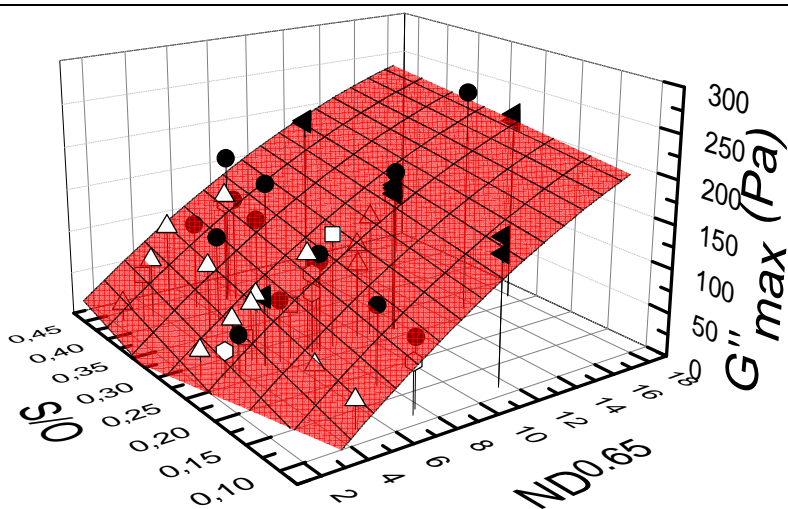


Figure A 57. (A) Scale-up specific model for G' ($\alpha = 0.73$) and current experimental values. $t = 5.08$ min/
S/O = 0.267 ± 0.020 . (B) Scale-up global model for G' ($\alpha = 0.63$) and current experimental values. $t = 5.08$ min/
S/O = 0.267 ± 0.020 .

A 2.4. Scale-up general models from all the current and previous experiments.

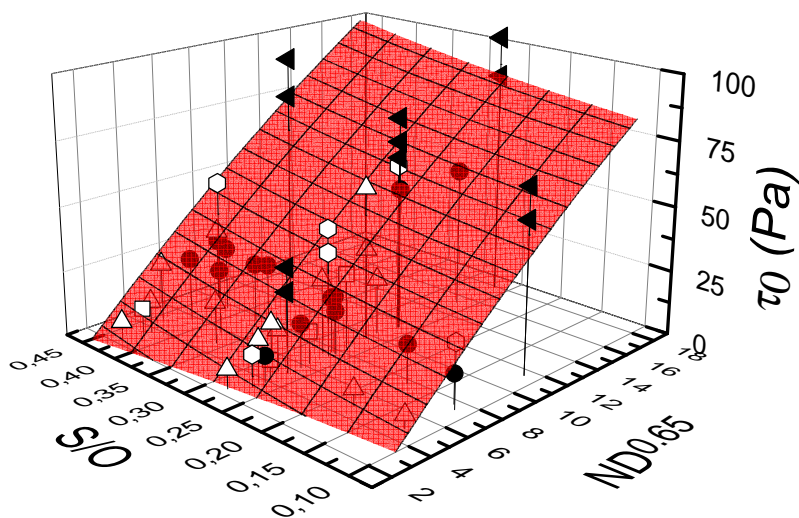
Storage module		Viscosity at $\dot{\gamma} = 1 \text{ s}^{-1}$		Yield stress	
$\alpha = 0.65$		$\alpha = 0.65$		$\alpha = 0.65$	
All factors	$R^2=0.918$	All factors	$R^2=0.793$	All factors	$R^2=0.785$
cnt	-394.122	cnt	-23.336	cnt	-39.9885
SO	1149.16	SO	0.70745	SO	41.2604
t	3.51173	t	2.05542	t	3.06814
ND $^\alpha$	71.7241	ND $^\alpha$	6.81352	ND $^\alpha$	7.47299
SO·SO	-111.706	SO·SO	76.0863	SO·SO	51.1844
SO·t	-0.857913	SO·t	-5.07955	SO·t	-6.21771
SO·ND $^\alpha$	-37.6436	SO·ND $^\alpha$	6.38526	SO·ND $^\alpha$	0.463545
t·t	-0.533322	t·t	-0.030139	t·t	-0.0474696
t·ND $^\alpha$	1.58486	t·ND $^\alpha$	0.0434906	t·ND $^\alpha$	-0.0151409
ND $^\alpha$ ·ND $^\alpha$	-0.446052	ND $^\alpha$ ·ND $^\alpha$	-0.165767	ND $^\alpha$ ·ND $^\alpha$	-0.071697

Loss modulus		Critical yield stress	
$\alpha = 0.65$		$\alpha = 0.65$	
All factors	$R^2=0.911$	All factors	$R^2=0.874$
cnt	-113.959	cnt	-59.6012
SO	264.289	SO	64.0821
t	2.9204	t	2.73349
ND $^\alpha$	23.0857	ND $^\alpha$	12.6013
SO·SO	-27.3606	SO·SO	133.617
SO·t	-2.37308	SO·t	-7.53427
SO·ND $^\alpha$	-7.55177	SO·ND $^\alpha$	-0.583854
t·t	-0.105331	t·t	-0.0256353
t·ND $^\alpha$	0.0801098	t·ND $^\alpha$	0.070665
ND $^\alpha$ ·ND $^\alpha$	-0.376446	ND $^\alpha$ ·ND $^\alpha$	-0.179922



- Large scale ● Medium scale
- △ Small scale ◀ Medium scale previous work
- Small scale previous work

Figure A 58. Scale-up general model G''_{max} ($\alpha = 0.65$) and all the experimental values (from current and previous work). $t = 5.08$ min.



- Large scale ● Medium scale
- △ Small scale ◀ Medium scale previous work
- Small scale previous work

Figure A 59. Scale-up general model τ_0 ($\alpha = 0.65$) and all the experimental values (from current and previous work). $t = 5.08$ min.

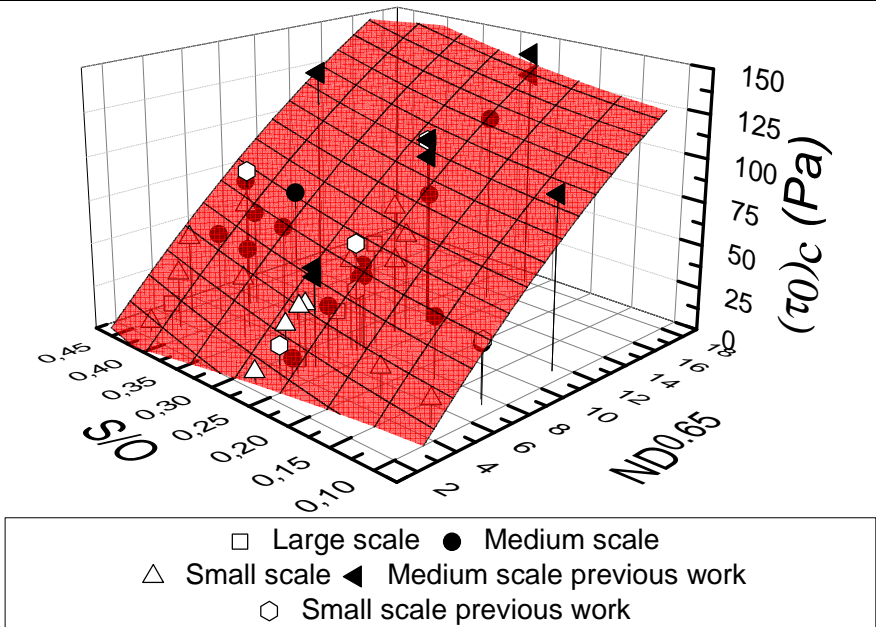


Figure A 60. Scale-up general model $(\tau_0)_c$ ($\alpha = 0.65$) and all the experimental values (from current and previous work). $t = 5.08$ min

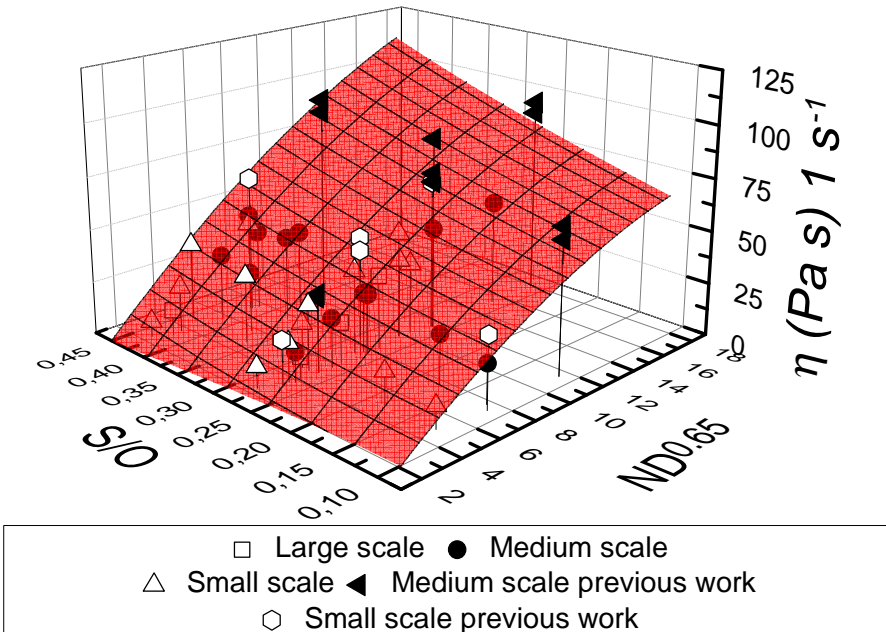


Figure A 61. Scale-up general model η (1 s^{-1}) ($\alpha = 0.65$) and all the experimental values (from current and previous work). $t = 5.08$ min.

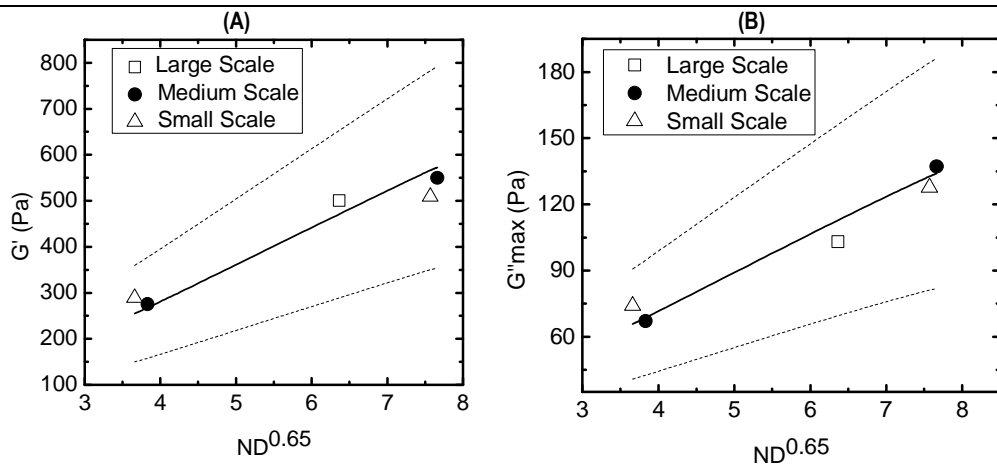


Figure A 62. (A) Scale-up general model G' ($\alpha = 0.65$) and the current experimental values. $t = 18.24$ min/ $S/O = 0.43 \pm 0.02$. (B). Scale-up general model G'' ($\alpha = 0.65$) and the current experimental values. $t = 18.24$ min/ $S/O = 0.43 \pm 0.02$.

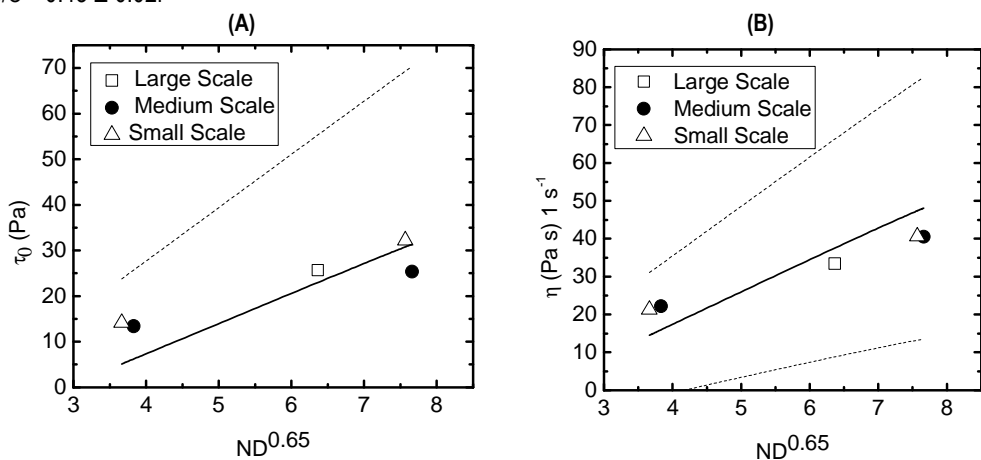


Figure A 63. (A) Scale-up general model $(\tau_0)_c$ ($\alpha = 0.65$) and the current experimental values. $t = 18.24$ min/ $S/O = 0.43 \pm 0.02$. (B). Scale-up general model η ($1 s^{-1}$) ($\alpha = 0.65$) and the current experimental values. $t = 18.24$ min/ $S/O = 0.43 \pm 0.02$.

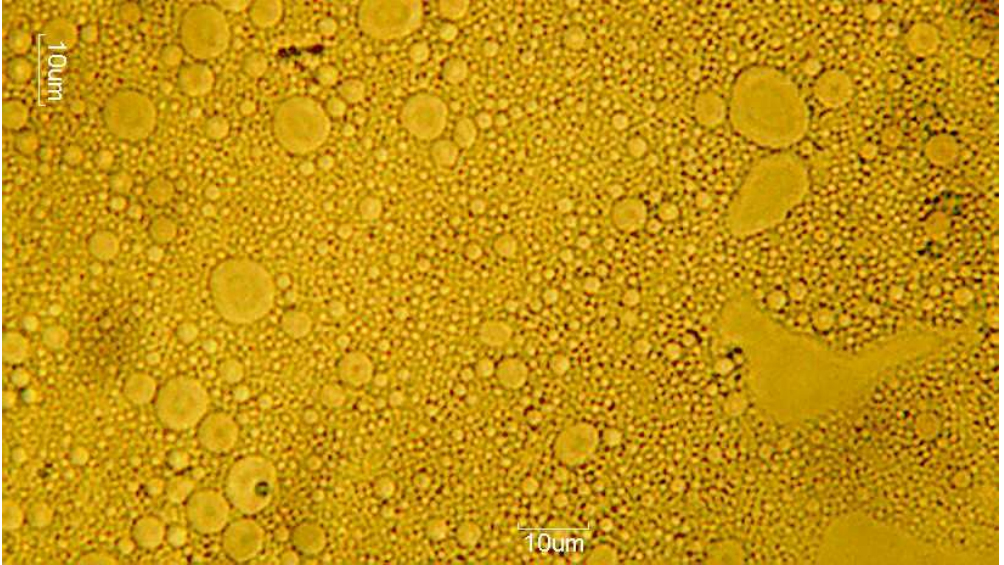
A 2.5. Images of the droplets of the emulsions obtained with the optical microscope

Figure A 64. Droplet's image of small scale emulsion. $S/O = 0.267$, $Q = 14$ mL/min , $N = 1050$ rpm.

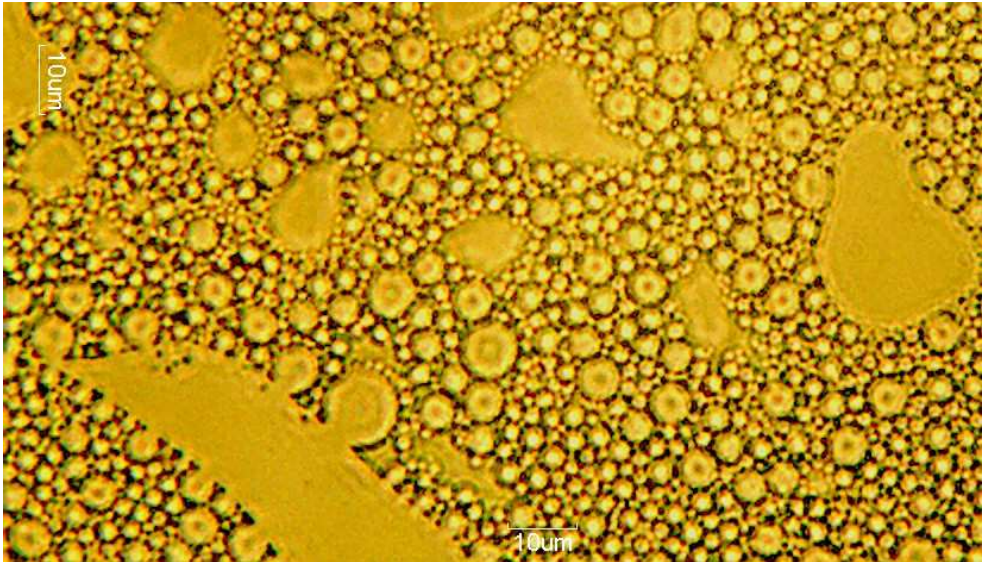


Figure A 65. Droplet's image of small scale emulsion. $S/O = 0.44$, $Q = 14$ mL/min , $N = 700$ rpm.

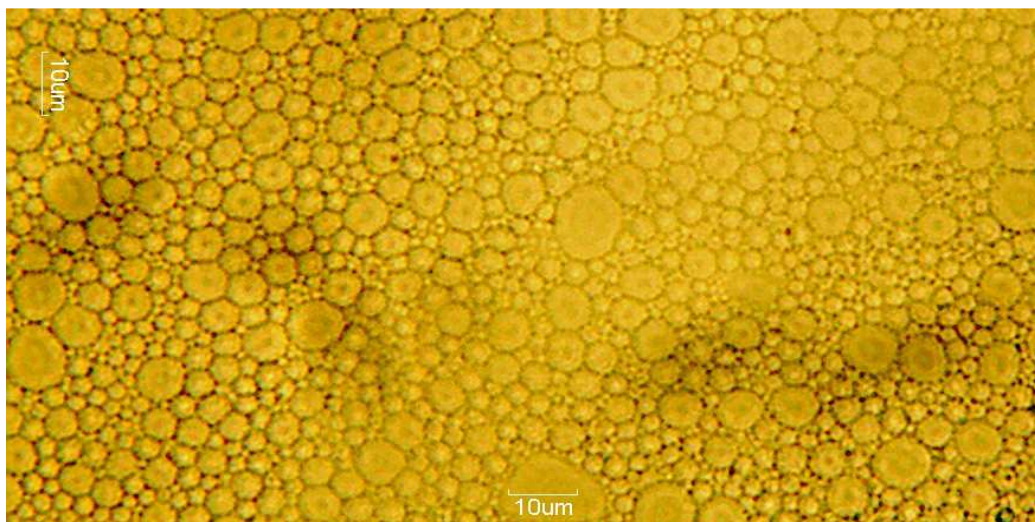


Figure A 66. Droplet's image of medium scale emulsion. S/O = 0.267, Q = 112 mL/min , N = 525 rpm.

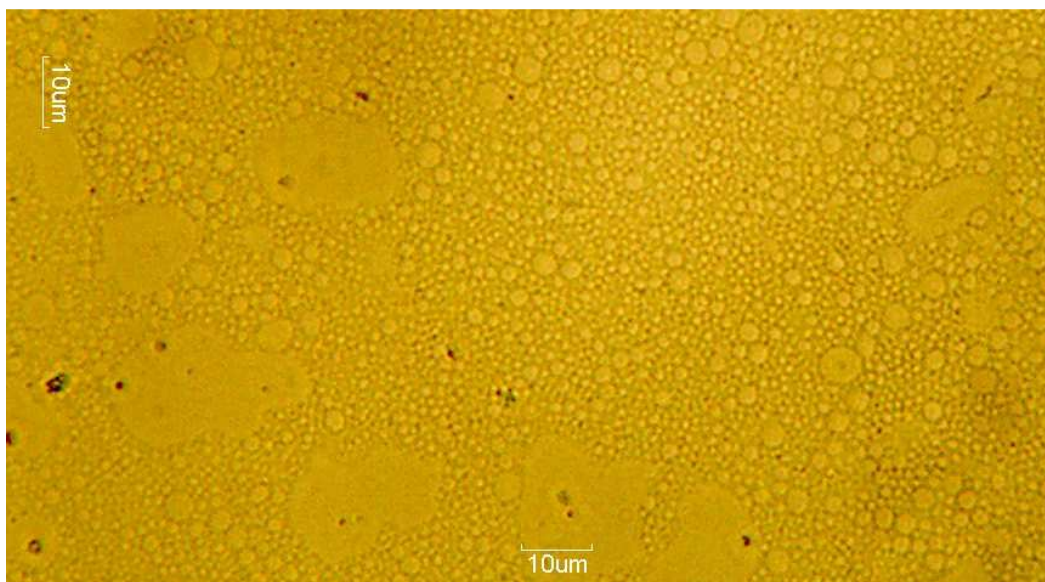


Figure A 67. Droplet's image of medium scale emulsion. S/O = 0.267, Q = 112 mL/min , N = 1050 rpm.

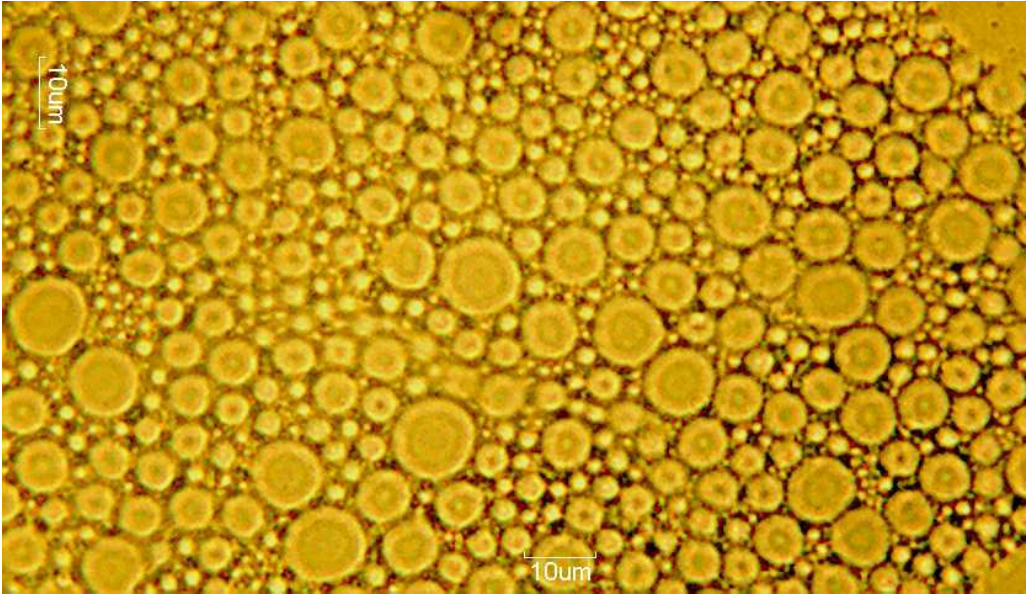


Figure A 68. Droplet's image of medium scale emulsion. $S/O = 0.267$, $Q = 112$ mL/min , $N = 350$ rpm.

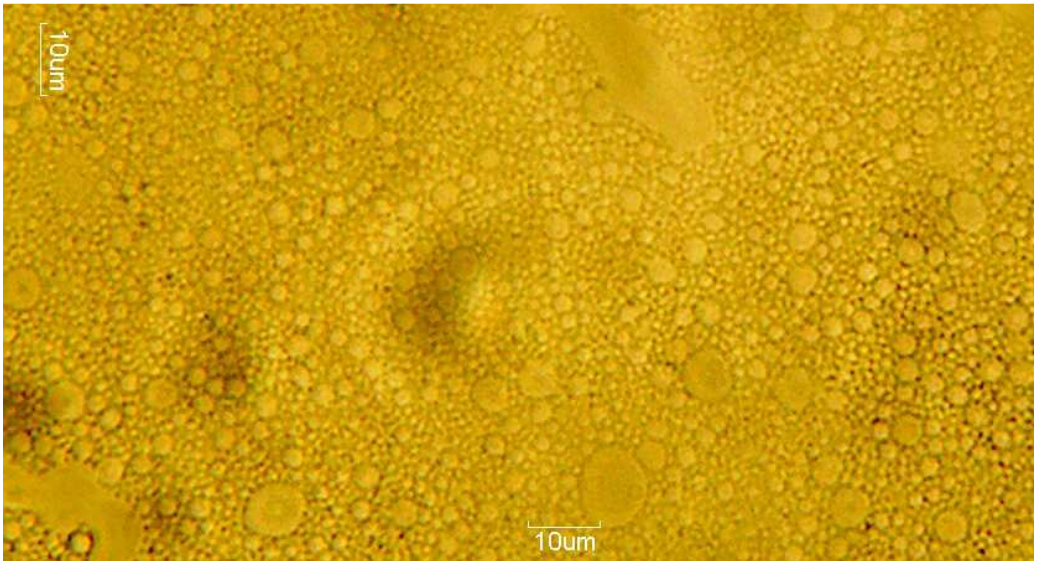


Figure A 69. Droplet's image of large scale emulsion. $S/O = 0.42$, $Q = 248$ mL/min , $N = 400$ rpm.

